Design and optimization of a meso-scale helical-tube-bundle heat exchanger

By

Yaning Wang

A dissertation submitted in partial fulfillment of

the requirements for the degree of

Doctor of Philosophy

(Mechanical Engineering)

at the

UNIVERSITY OF WISCONSIN - MADISON

2023

Date of final oral examination: 02/28/2023

Preliminary examination committee:

John Pfotenhauer, Professor, Mechanical Engineering
Franklin Miller, Professor, Mechanical Engineering
Gregory Nellis, Professor, Mechanical Engineering
Jennifer Franck, Assistant Professor, Engineering Physics
Mark Anderson, Associate Professor, Mechanical Engineering

Abstract

A recuperative heat exchanger is an important component in cryogenic systems, which is commonly applied for the cooling of superconducting electronics, infrared sensors, power systems, etc. Heat exchangers with helical tubes are applied widely since secondary flow is generated in the shell side and heat transfer can be augmented. Currently, the most common designs are the spiral wound heat exchangers, which consist of many layers of spiral tubes with different coil diameters in a closed shell. However, in a spiral wound heat exchanger, most of the fluid in the shell-side passes directly through the gap between two adjacent layers, which weakens the turbulence and the associated heat transfer coefficient. Furthermore, it is difficult to ensure that parallel tubes in such designs have equal length, resulting in non-uniform flow distribution and reduced efficiency. A novel twisted helical bundle geometry is proposed in this thesis of which the thermal performance is explored using CFD simulation.

To satisfy the requirement of the above cryogenic applications, the temperature span of the heat exchanger should be quite large. In this study, the proposed heat exchanger uses helium gas as the working fluid and is envisioned to operate between 300 K and 30 K with an effectiveness larger than 99%. The diameter of the inner tubes is in the meso-scale range ($\leq$1mm). Several tubes are twisted into one bundle and then several bundles are twisted into one group. The curve of each tube in the bundle is generated by different 3D sinusoidal equations, producing the same end-to-end length and coil diameter for each tube. Fluent is used to investigate the heat transfer and fluid flow characteristic of a fully developed region for both shell side and coil side separately. Due to its ability to account for the transport effects

of the turbulent shear stress and resolve the viscous sublayer, the k-omega SST model is used in this study for both the shell side and tube side simulation.

The twisted helical bundle geometry configuration can be specified by the number of bundles, number of tubes per bundle, pitch length of the bundle and tube diameter. The influence of these parameters on the thermal-hydraulic performance has been investigated. Nusselt number and friction factor correlations for both the shell side flow and tube side flow have been developed based on Reynolds number and dimensionless geometrical parameters including the conduction shape factor and pitch length, and these correlations are used as inputs for the overall heat exchanger model.

To find the intrinsic characteristic of geometry with better thermal performance and optimize the design, the vortex structure of shell side flow has been visualized and analyzed using the Q-criterion. The relationship between average vorticity magnitude on the Q-criterion iso-surface and the conductance has been characterized and can be further explored.

The overall heat exchanger design is proposed considering the heat exchange length, size limitation and flow redistribution problem. A 1D finite difference model accounting for axial conduction, parasitic heat load, varying thermal properties is built, in which the energy balance equations are based on pure counter flow configuration. The temperature profiles for the shell side, tube side and metal are solved using the weighted relaxation technique, and then the performance of the heat exchanger is calculated. Several assumptions are made during this process, including the constant heat flux boundary conditions and pure counter flow configuration, and the consistency of these assumptions are verified.

Based on the numerical results, a configuration with a pitch length of 50 mm, a tube outer diameter of 1.2 mm and tube inner diameter of 1 mm, with 8 tubes in one bundle, 6 bundles in one group and 9 groups going in parallel has been found to meet all design requirements (effectiveness>0.99 with mass flow rates up to 13 g/s, pressure drop<1 bar for both sides, and also the volume and mass limitation).

Table of Contents

List of Figures

List of Tables

Nomenclature

General

a, b	amplitudes of the two sine curves generating the tube path, mm
A	area, m^2
c	initial phase of the tube curve
C	conductance, W/K in Fluent simulation, or the capacity rate in Matlab (W/K)
CR	capacity ratio
d	number of tubes in the tube curve equation
D	tube diameter, m
DD	distance between two adjacent tubes in one bundle, m
D_h	hydraulic diameter, m
f	friction factor
h	heat transfer coefficient, $W/m^2 \cdot K$
k	thermal conductivity, W/m·K
L	total heat exchange length, m
N	number of tubes in the correlations, number of sections in the overall heat exchanger model
Nu	the Nu value
P	pressure, Pa
p	pitch length, m
q	heat flux, W/m^2
R	thermal resistance, K/W
Re	the Reynolds value

S	conduction shape factor, m
SR	strain rate tensor
u	velocity, m/s
u_τ	friction velocity, m/s
y+	the dimensionless wall distance
u+	the dimensionless velocity
ρ	density, kg/m^3
μ	dynamic viscosity, kg/m·s
ν	kinematic viscosity, m^2/s
τ_ω	wall shear stress, N/m^2
Ω	vorticity tensor
TKE	turbulence kinetic energy, m^2/s^2
β	number of transfer units
λ	axial conduction parameter
χ	dimensionless parasitic heat transfer rates
Θ	dimensionless temperature

Subscripts

c	Cold side
f	either hot fluid or cold fluid
h	hot side
m	metal
t	axis position in the equations generating the tube path

1. Introduction

1.1. Research motivation

Recuperative heat exchangers play an important role and have a large influence on the overall efficiency in many cryogenic systems. The motivation of this study is to design a compact meso-scale tube heat exchanger which can achieve high effectiveness (>99%) and minimization at the same time. There have been many studies on the shell side flow of a circular shell fitted with helical structures, flow in the helical coiled tubes and flow in the spiral wound heat exchangers, but little studies on twisted helical-tube-bundle meso-scale heat exchangers were reported. Thus, a novel geometry is proposed in this study.

Recuperative cryocoolers are used for the cooling of infrared sensors, superconducting electronics, etc. The three most common cycles are the Joule-Thomson cycle, Brayton cycle and Claude cycle, and their schematics are demonstrated in Figure 1.1 [1,2]. The heat exchangers for recuperative cycles are known as recuperators, which have two separate flow channels, one for high pressure flow coming out of the compressor, and another for low pressure flow entering the compressor. Many application scenarios limit the size and weight of cryocoolers and recuperative cryocoolers are usually tabletop size. For the typical application scenario, i.e., the cooling of infrared sensors in space, the required temperatures are in the range of 2-100 K [1], so flow goes through a large temperature span in the recuperator.

Studies have shown that the recuperator has a significant influence on the overall cryocooler performance, and a good recuperator design can accelerate the cooling rate, increase cooling efficiency, use less working fluid and therefore provide a lightweight system design [3]. The recuperators to achieve fast cooldown can be summarized as effective, compact, and low

pressure-drop [4]. Designing and manufacturing this type of heat exchanger has been a challenge, especially when the size and effectiveness objectives are becoming more and more strict with the development of the application scenarios.

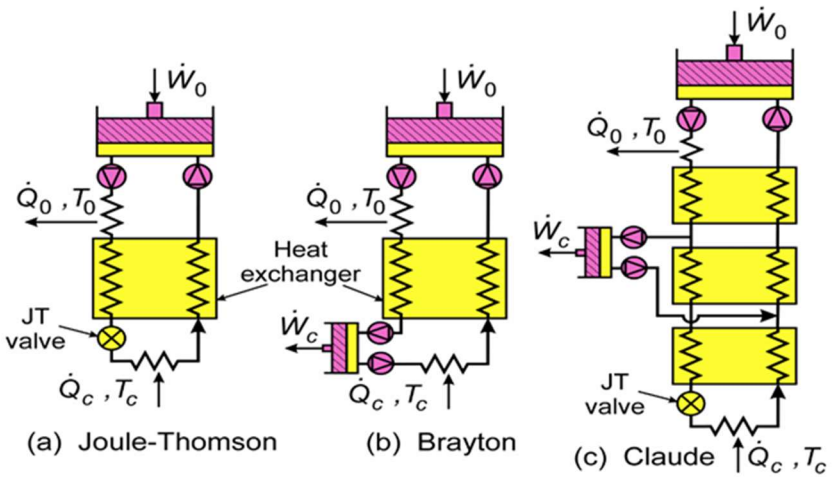

Figure 1.1. Schematics of the three most common recuperative cycles [1,2].

In next section, studies on recuperative heat exchangers and the state-of-the-art geometric designs are reviewed.

1.2. Research on recuperative heat exchangers

In space exploration missions, efficient and long life mechanical cryocoolers are required for cooling of optical heat loads and advanced space instruments, such as sensors, shields and telescopes. Brayton cryocoolers are appropriate for this purpose since the working fluid flows continuously in the closed cycle and negligible vibrations are produced [5]. Recuperators with different structures for Brayton cycles have been designed in recent years. In March 2002, a single stage reverse Brayton cryocooler started operating and provided refrigeration to the NICMOS (Near Infrared Camera and Multiple Object Spectrometer) on the Hubble space telescope, and this is the first space implementation of a turbo-Brayton cryocooler [6]. The recuperator for this system is a Slotted-Plate Heat exchanger (SPHX) developed by Creare, consisting of 300 slotted copper plates which are uniformly distributed along the length of the stainless steel outer shell. The two counter flows are separated by spacers brazed between adjacent plates [7]. The design, demonstrated in Figure 1.2, has a diameter and length of 90 mm and 560 mm respectively, and the mass is 7.7 kg [6,7,8].

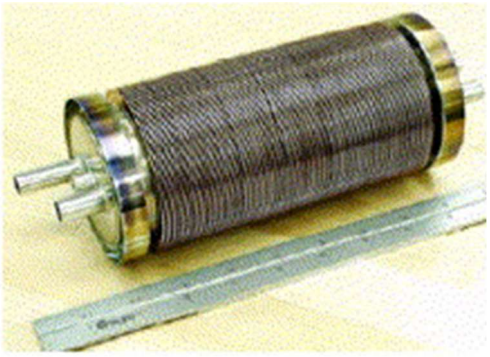

Figure 1.2. The Slotted Plate Heat exchanger [6].

In 2007, Creare developed the Silicon Micro-Machined Recuperator (SMR) as a candidate recuperator for turbo-Brayton cryocoolers [8]. The whole design and details of the silicon slotted plate are shown in Figure 1.3. The comparison between the SMR and Cu-SS SPHX is shown in

Table 1.1. Due to the use of lightweight materials and precision photo-etching techniques, the SMR is smaller and lighter than the Cu-SS SPHX for the same thermal performance.

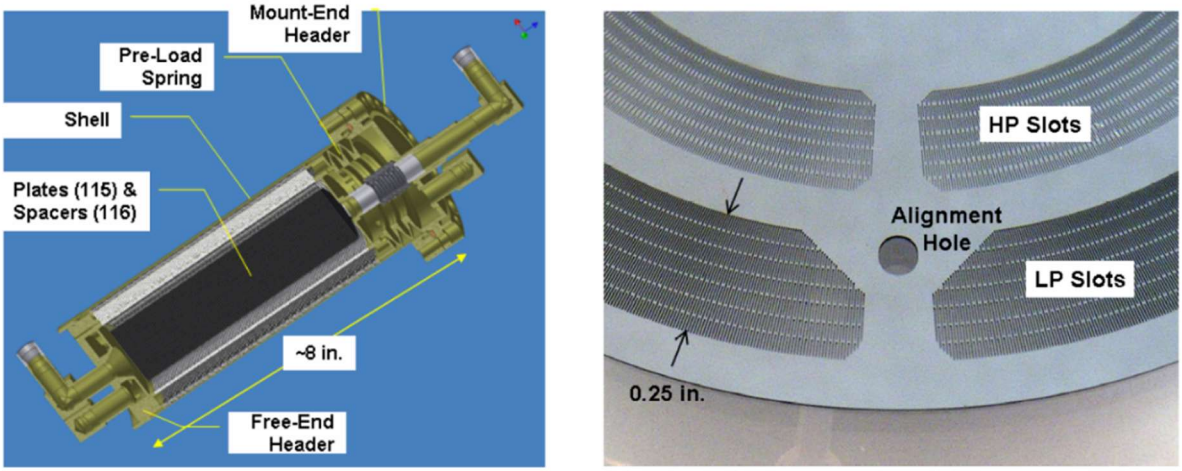

Figure 1.3. Silicon Micro-Machined Recuperator and the details of the silicon slotted plate [8].

Table 1.1. Comparison between Cu-SS SPHX and SMR [8].

	Cu-SS SPHX	SMR
Design Conditions		
Mass Flow Rate	1 g/s of Ne	1 g/s of Ne
HP Inlet Temperature	85 K	85 K
LP Inlet Temperature	35 K	35 K
HP Inlet Pressure	3.2 atm	3.2 atm
LP Inlet Pressure	2.0 atm	2.0 atm
Predicted Performance		
Thermal Ineffectiveness	0.012	0.012
Fractional Pressure Drop	< 0.3%	< 0.3%
Design		
Total Mass / Core Mass	4.7 kg / 4.1 kg	1.3 kg / 0.36 kg
Total Length / Core Length	17 in. / 14 in.	8.2 in. / 5.8 in.
Shell Diameter	3.5 in.	2.9 in.
Number of Plates	225	115

In 2014, Creare started to develop a micro shell and tube recuperator for a 10K cryocooler, which consists of thousands of stainless steel microtubes that are laser welded to a stainless steel tube sheet [5,9]. Two design configurations have been proposed. The legacy arrangement with an

annular core and the adapted design without an annular core are shown in Figure 1.4 [5]. The purpose of the adaptation is minimizing flow maldistribution penalties, axial conduction, and mass of the heat exchanger. The adapted module contains over 3800 tubes, with a shell outer diameter as 65 mm, a length as 580 mm, and total mass as 3.4 kg. The micro-tube laser welding system is shown in Figure 1.5, and the advantage of this technique is allowing the fabrication of 100% hermetic recuperators.

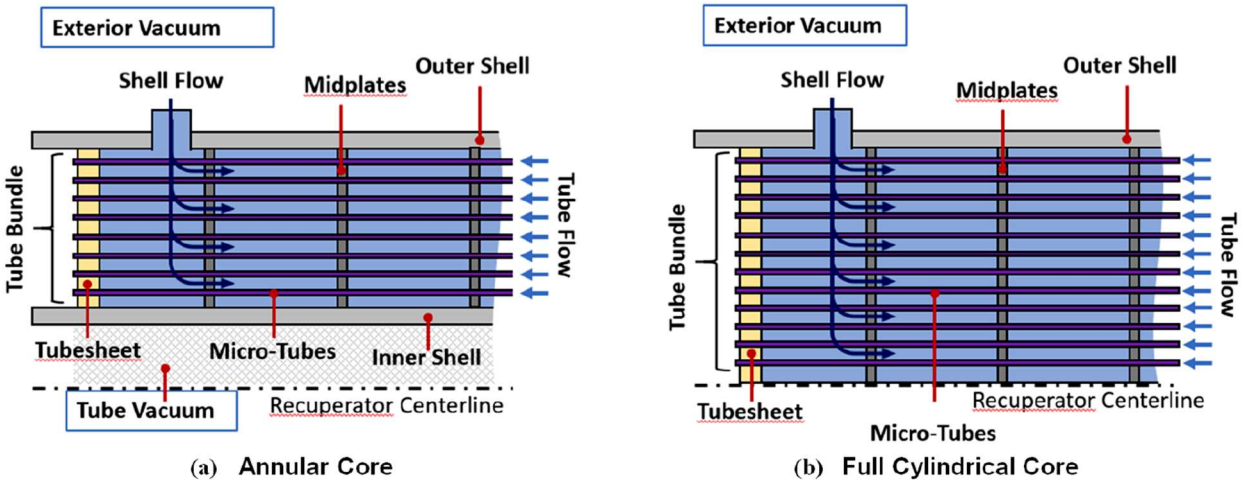

Figure 1.4. Illustration of microtube recuperator core layout. Relative to the legacy annular core arrangement (a), the fully cylindrical core (b) populated the core interior with microtubes, leading to a more compact, lightweight design. The cylindrical core also eliminates the inner shell, reducing parasitic axial conduction and further reducing weight [5].

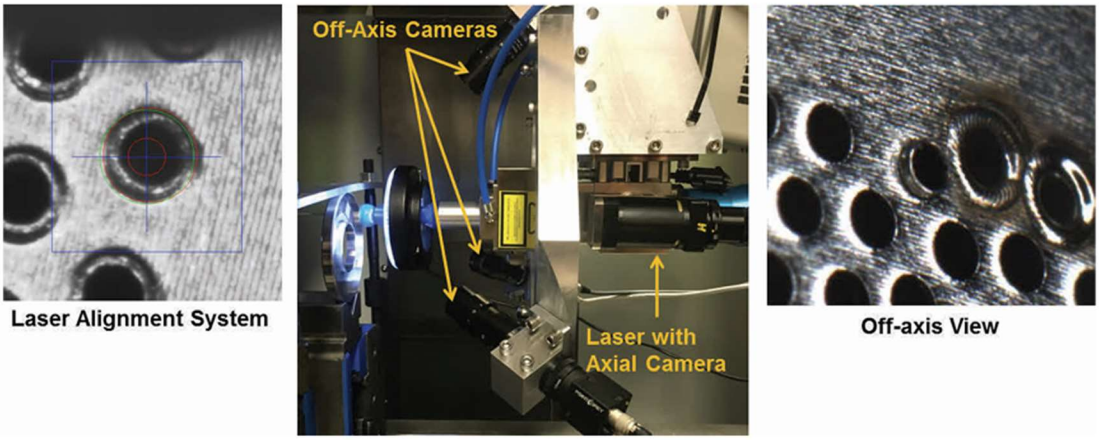

Figure 1.5. Micro-tube laser welding system [9].

Besides the reverse Brayton cryocooler, the optimization of miniature Joule-Thomson cryocoolers and the characteristic of the related heat exchangers are also research hotspots. The two basic configurations of recuperators for Joule-Thomson cryocoolers are shown in Figure 1.6 [4]. The recuperators for typical Hampson cryocoolers contain a helical finned tube around the mandrel in a shell, as an example shown in Figure 1.7 [10]. In 2021, Wei et al. proposed a non-isometric helically spiral heat exchanger with different fin pitch structure, shown in Figure 1.8. The sparse fin f_{p1} is used near the hot end while the dense fin f_{p2} is used near the cold end. By distributing the fin pitch in this way, the new structure increased the cool-down rate by 13.4%. Thus, the new structure can obtain rapid cooling characteristics without increasing the pressure drop a lot by using a whole denser fin structure. The mechanism behind the good cool down performance is complicated and needs to be further explored [11].

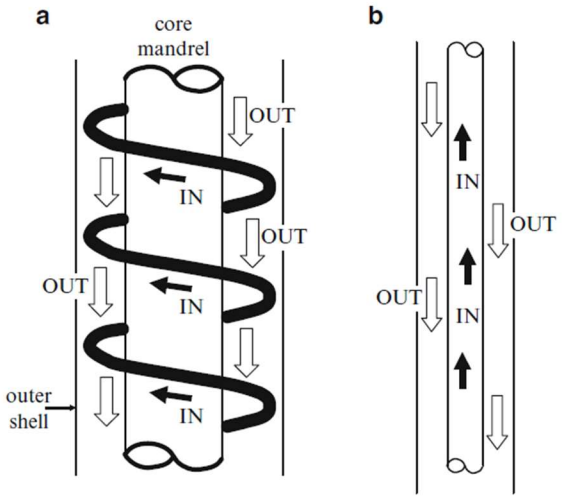

Figure 1.6. The two basic configurations of counter flow heat exchangers for Joule-Thomson cryocoolers, (a) Giauque-Hampson, and (b) Linde. IN represents the high-pressure supply flow and OUT the low-pressure return flow [4].

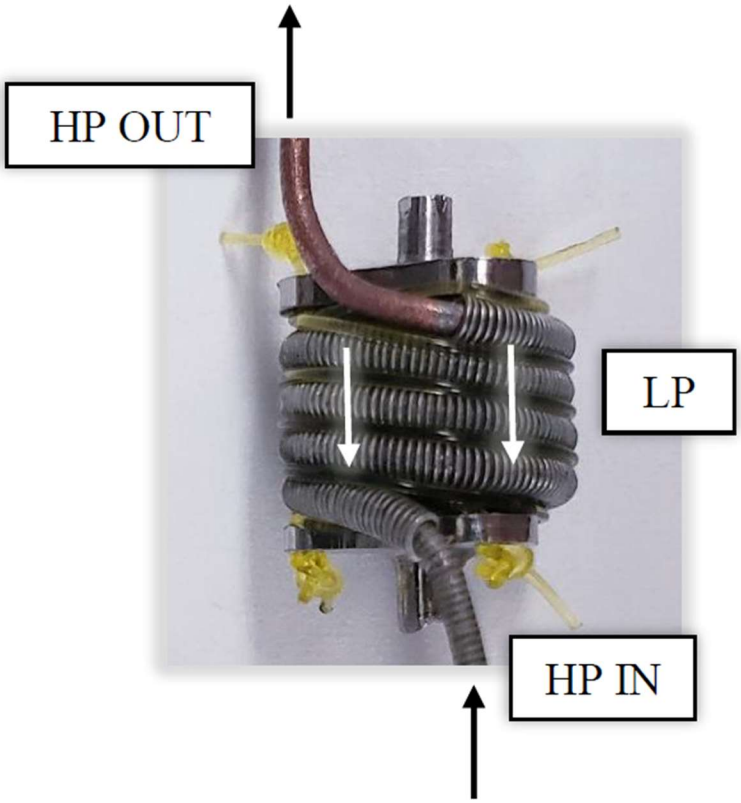

Figure 1.7. Photo of high pressure finned-tube helically coiled upon a cylindrical coil (without shell) [10].

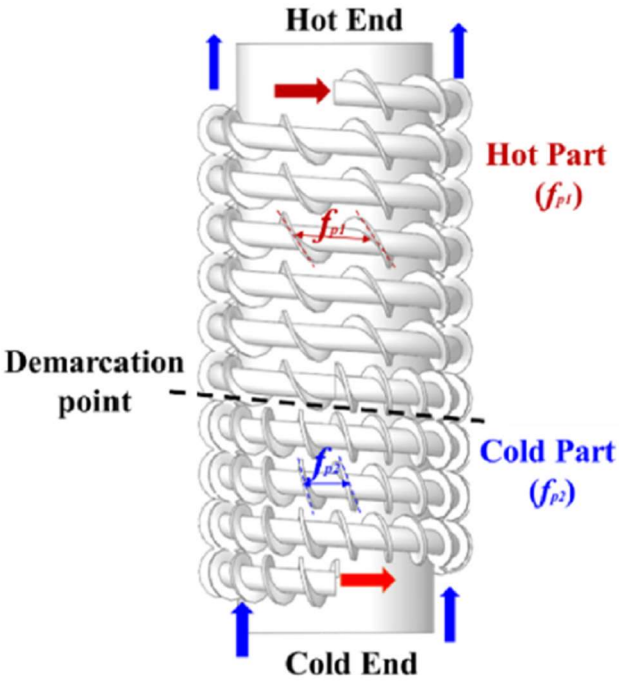

Figure 1.8. First-sparse-then-dense-structure recuperator [11].

The development trend of recuperators is being smaller, lighter, and more efficient. Studies on geometric structures which can facilitate heat transfer and reduce size are introduced in the following sections, including both recently proposed geometry and mature techniques.

1.3. Research on meso-scale tube heat exchangers

Heat exchangers with meso- and micro-scale channels have been a research trend due to their high ratio of surface area to volume, lower total mass, and low inventory of working fluids. Many studies have focused on the flow and heat transfer characteristics in micro- and meso-scale channels, and early transition to turbulence and thermal enhancement was noticed [12]. Meso-scale channels are defined when the characteristic length is no larger than 1 mm.

In 1994, Wang and Peng found that in meso-scale channels the fully developed turbulent heat transfer regime was initiated at Reynold's number (Re) values ranging from 1000 to 1500, rather than 2300 [13]. In 1995, one of the first studies, carried out by Gui and Scaringe, ascribe enhanced heat transfer coefficients in meso-scale channels to three key factors, which are the channel entrance effects, the pre-existing turbulence at the inlet and the surface roughness which leads to a thinner thermal boundary layer. They also stated that the critical Re number is around 1400 [14]. Based on their studies, it is reasonable to assume fluid mixing and heat transfer are more thorough in meso-scale channels than in normal size channels.

1.4. Research on heat exchangers with helical structures

Since highly compact flow passages are generally continuous without any interruptions [12], helical structures turn out to be a good option. In 1999, Rush and Newell found that in sinusoidal wavy passages, even when the flow is in the laminar regime, some macroscopic mixing different than the regular circulation occurs near the channel exit at relatively low Re values, as shown in Figure 1.9. The mixing moves toward the entrance as the Reynold's number is increased, as does the Nusselt number enhancement [15].

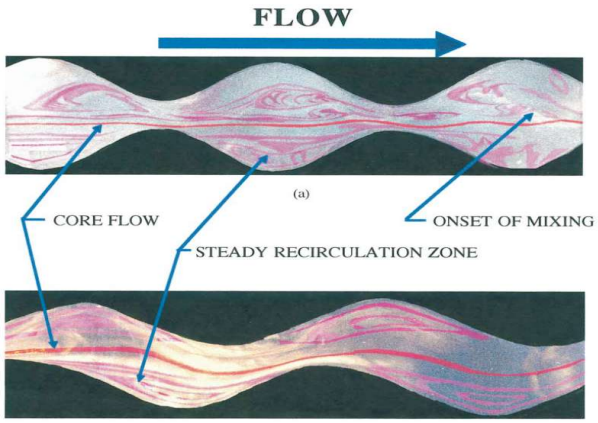

Figure 1.9. Fluid mixing different than regular recirculation in the laminar regime [15].

In recent years, CFD simulation has become an important method to explore various geometry shapes and to help optimize the design. Many Nu and friction factor correlations have been proposed based on different geometry factors. Along with advances in manufacturing, more and more shapes have been analyzed to improve the thermal performance of heat exchangers, usually by producing a thinner average thermal boundary layer as a result of adding interruptions and promoting flow mixing via secondary flows.

In 2007, Sivashanmugam and Suresh carried out experimental studies on heat transfer and hydraulic characteristics in the shell side of a circular tube fitted with regularly spaced helical screw-tape inserts, as shown in Figure 1.10 [16]. The effect of twist ratio and spacer length was

explored. Nu and friction factor correlations based on Re, twist ratio, spacer length and hydraulic diameter were proposed.

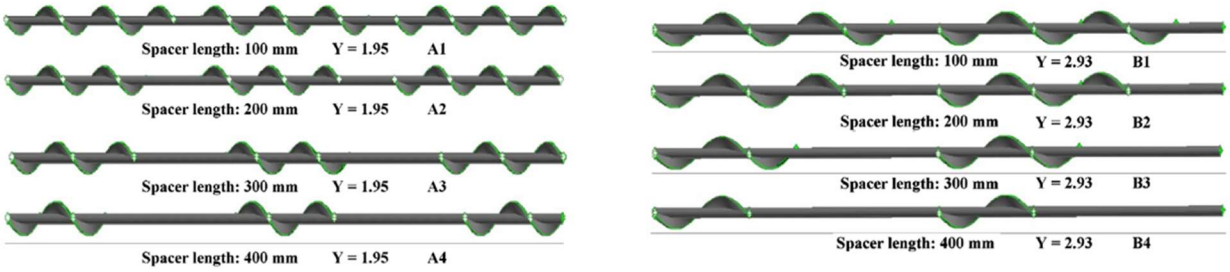

Figure 1.10. Helical screw inserts with various spacer length and twist ratio Y [16].

In 2009, Zhang, He and Tao studied shell-and-tube heat exchangers with middle-overlapped helical baffles and continuous baffles, shown in Figure 1.11 [17, 18]. They carried out a 3D simulation of the shell side flow using the renormalization group (RNG) k-ε model and the simulation results were compared with experimental data. Taking the heat transfer coefficient per unit pressure drop as the comparison criterion, the thermal performance of the non-continuous middle-overlapped helix angle case is better than the continuous helix angle case.

In 2010, Jayakumar, Mahajani et al. carried out CFD analyses on flow inside helically coiled tubes [19]. Different geometry parameters including pitch circle diameter, tube pitch and pipe diameter and their influence on heat transfer were explored. A correlation of coil side Nu based on Re and dimensionless curvature ratio is proposed.

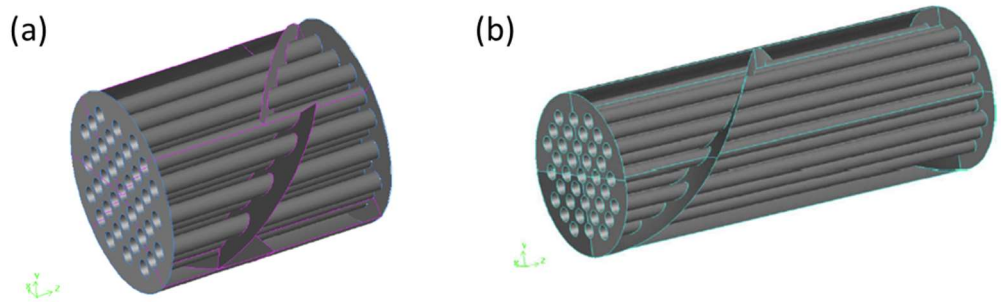

Figure 1.11. (a) shell-and-tube heat exchangers with middle-overlapped helical baffles. (b) shell-and-tube heat exchangers with continuous helical baffles [17, 18].

In 2010, Zachar studied the coil side heat transfer improvement of coiled-tube heat exchangers with a spirally corrugated wall compared to the common helically coiled heat exchangers [20]. The geometry is shown in Figure 1.12. A Nusselt correlation based on Dean number ($= Re\left(d_{pipe}/d_{coil}\right)^{0.5}$), corrugation depth, pitch value and tube diameter was built. The coiled tube with spirally corrugated wall showed 80-100% increase for the coil side Nu value while the relative pressure drop is 10-600% larger compared to the common coiled tube with a smooth wall.

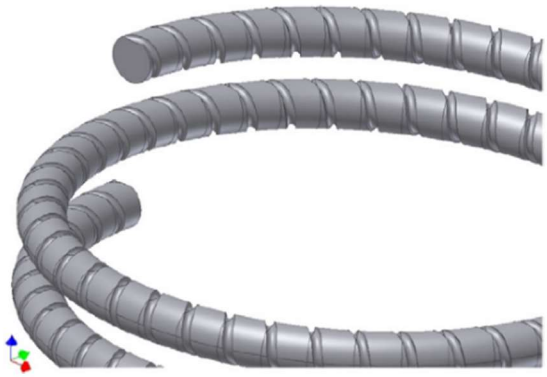

Figure 1.12. Helically coiled tube with spirally corrugated wall with corrugation depth 2.5 mm [20].

In 2013, Chen, Sheng et al. explored the flow and pressure distribution of a circumferential overlap trisection helical heat exchanger, shown in Figure 1.13 [21]. It was demonstrated that flow in the shell side rotates outward under centrifugal force and then rotates inward to the axis under the centripetal force due to the radial pressure difference. Thus, a secondary flow is generated and the fluid mixing is strengthened.

In 2013, Tan, Zhu et al. studied the flow and heat transfer characteristics in the shell side of a twisted oval tube heat exchanger with Realizable k-ε model [22]. The geometry is shown in Figure 1.14. The influences of twisted pitch length and aspect ratio of the oval were analyzed, and it was found that the intensity of the secondary flow increases with aspect ratio and decreases with pitch length.

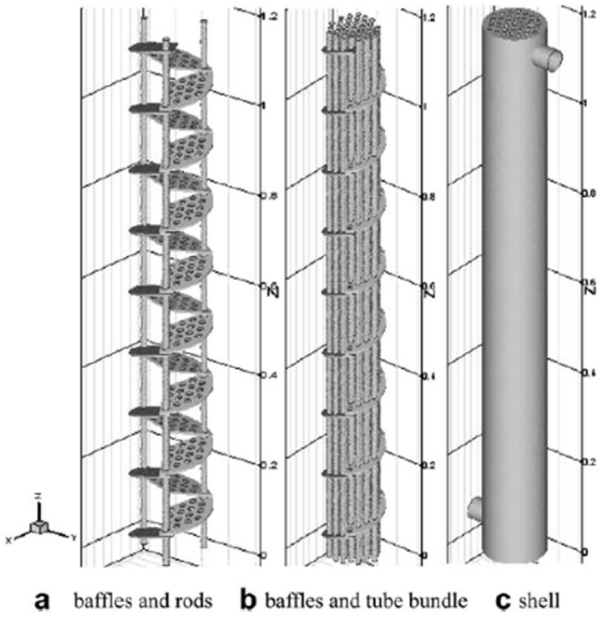

Figure 1.13. Structure of circumferential overlap trisection helical baffle heat exchanger [21].

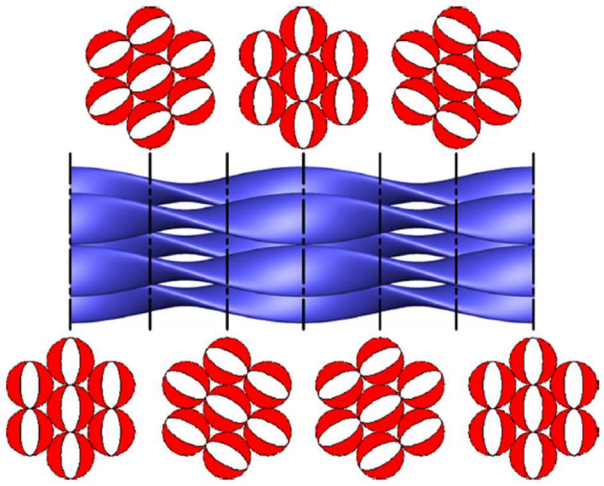

Figure 1.14. Sketch of the self-supported tube bundle of a twisted oval tube heat exchanger [22].

In 2015, Khoshvaght-Aliabadi and Pazdar et al. experimentally investigated heat transfer and flow characteristics of nanofluids flowing in the helical microtube with different coil diameters [23]. The helically microtubes are shown in Figure 1.15. The tube diameter is 787 μm. Both Nu and friction factor increase as the coil diameter decreases. Correlations of Nu and friction were developed based on Re, Pr, mass concentration of nanoparticle and curvature ratio.

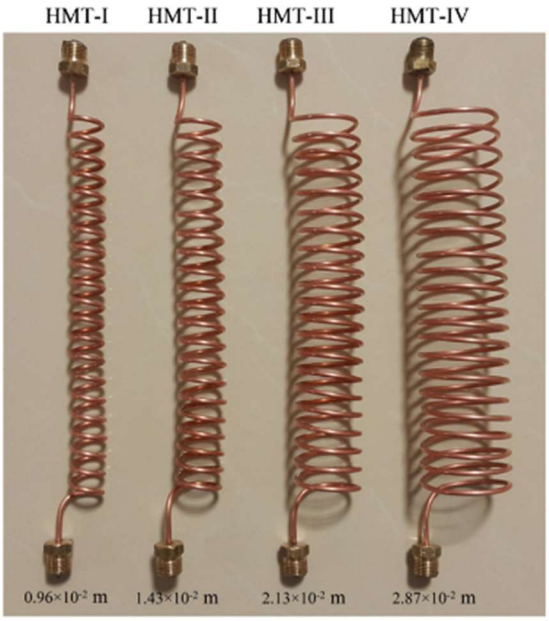

Figure 1.15. Helically microtube with different coil diameters [23].

In 2016, Alimoradi and Veysi carried out experiments and simulations on shell and coiled tube heat exchangers, and Nu correlations of both coil side and shell side were proposed [24]. A flow diagram of the experiment set up is shown in Figure 1.16. It was concluded that the effect of pitch length on the coil side heat transfer was negligible, while it influenced the Nu value on the shell side. Tube diameter and coil diameter had influence on the Nu value of both sides. They also compared four turbulent models, i.e., Standard k-ε, Realizable k-ε, RNG k-ε and Spalart Allmaras. By comparing the outlet temperatures of both sides, the difference among these four models was negligible.

In 2018, Rasheed and Salman et al. investigated heat transfer and flow characteristics of a nanofluid flowing in the helical microtube with different pitch lengths (10, 14 and 18 mm) using Fluent [25]. The micro tube model is shown in Figure 1.17. The tube diameter was 1.5 mm. The $k-\varepsilon$ model was adopted. The increase of Nu with the decrease of pitch was not noticeable, which was consistent with the experimental results of Alimoradi and Veysi, while the increase of friction

factor with the decrease of pitch was obvious. Thus, it was concluded that the largest pitch value leads to highest thermal performance factor for the coil side flow.

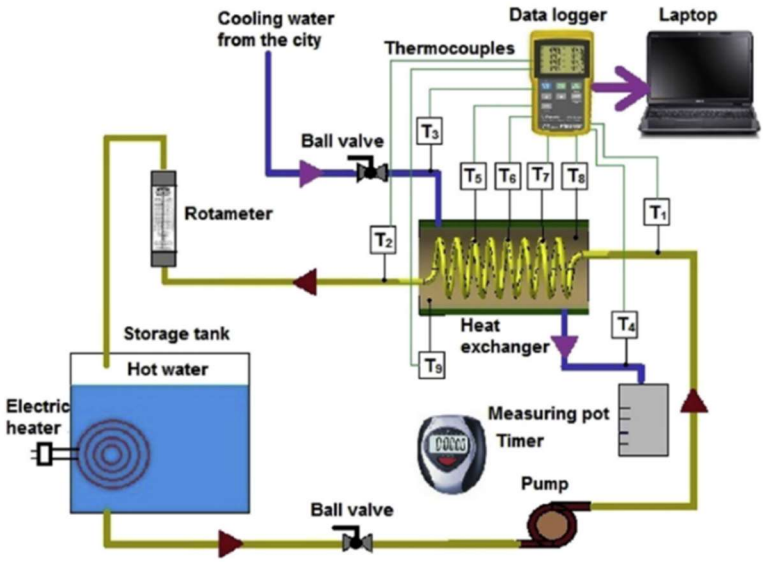

Figure 1.16. Flow diagram of the experiment set up of shell and coiled tube heat exchangers [24].

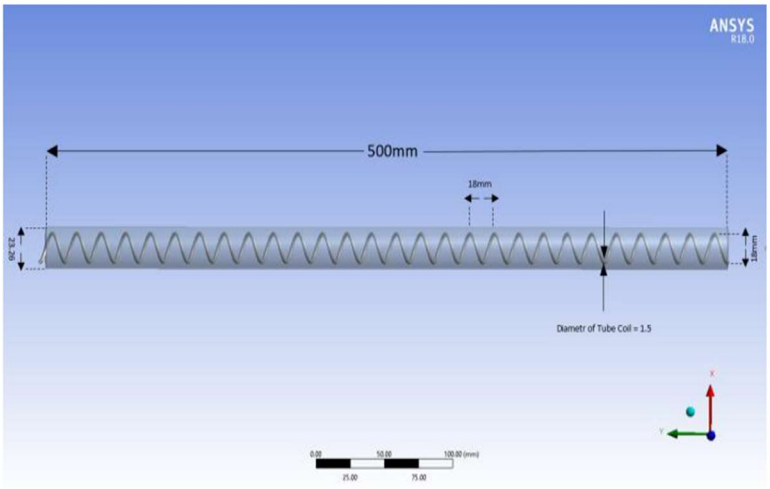

Figure 1.17. Micro tube model [25].

1.5. Research on spiral wound heat exchangers

Heat exchangers with compact helical tubes are applied widely in various industrial fields and cryogenic applications. Currently, the most common ones are the spiral wound heat exchangers, which consist of many layers of spiral tubes with different coil diameters in a closed shell. There have been many experimental and simulation studies on spiral wound heat exchangers and various correlations have been proposed.

In 2003, Neeraas and Fredheim et al. measured local heat transfer coefficient and frictional pressure drop in the shell side of spiral wound LNG heat exchangers [26]. Three kinds of working fluids were used, i.e., gas flow, liquid film flow and two-phase shear flow. The test heat exchanger shown in Figure 1.18 consisted of 3 layers of tubes and can be operated both in single-phase and two-phase flow. The measured Nu numbers were compared with the calculated results from the method developed by Gnielinski [27], where both laminar regime and turbulent regime were considered. The measured friction factor values were compared with the calculated results from the method developed by Barbe et al. with modification [28]. The agreement was very good, so both methods were recommended.

In 2012, Genic et al. presented the experimental results on the shell side heat transfer coefficient of spiral wound heat exchangers with different number of layers, different number of tubes on each layer and different winding directions, as shown in Figure 1.19 [29]. Two correlations of Nu were proposed, one based on the shell-side hydraulic diameter while the other based on the square root of the shell-side flow area. The ratio of viscosity at the fluid mean temperature over viscosity at the mean outer tube wall temperature was included in the formulas.

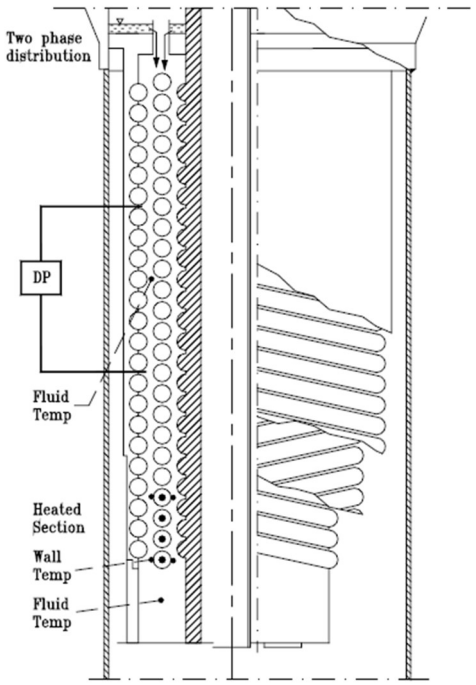

Figure 1.18. Test spiral wound heat exchanger [26].

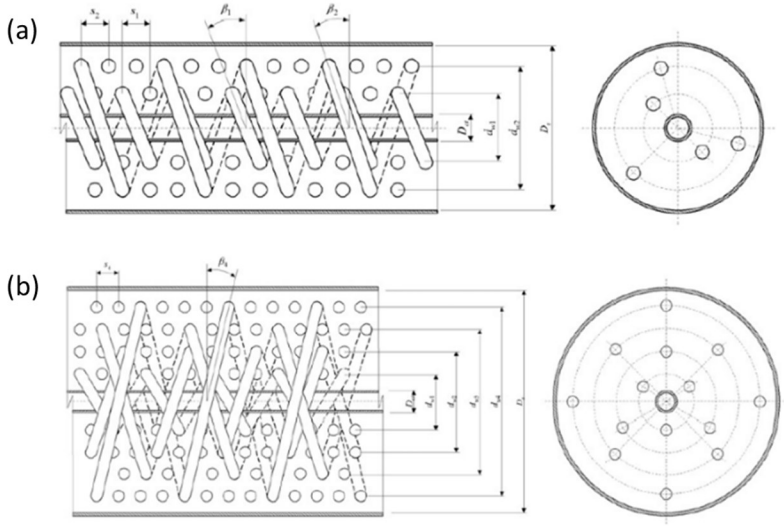

Figure 1.19. (a) Spiral wound heat exchanger with two layers wound in the same direction. (b) Spiral wound heat exchanger with four layers wound in the opposite direction [29].

In 2019, Abolmaali and Afshin carried out a CFD simulation to explore the heat transfer and flow characteristics for the shell side of spiral wound heat exchangers [30]. To determine

which turbulent model to select, different models including Shear Stress Transport (SST) $k-\omega$, RNG $k-\varepsilon$, Realizable $k-\varepsilon$ and Standard $k-\varepsilon$ were used to simulate the spiral wound heat exchanger tested by Neeraas et al. The model with the best agreement is SST $k-\omega$. The effects of the number of layers and pitch length in both the longitudinal and radial direction were explored, shown in Figure 1.20 as C, P_l and P_r respectively. Nu and friction factor correlations are based on Re, number of layers, tube diameter and pitch length in two directions.

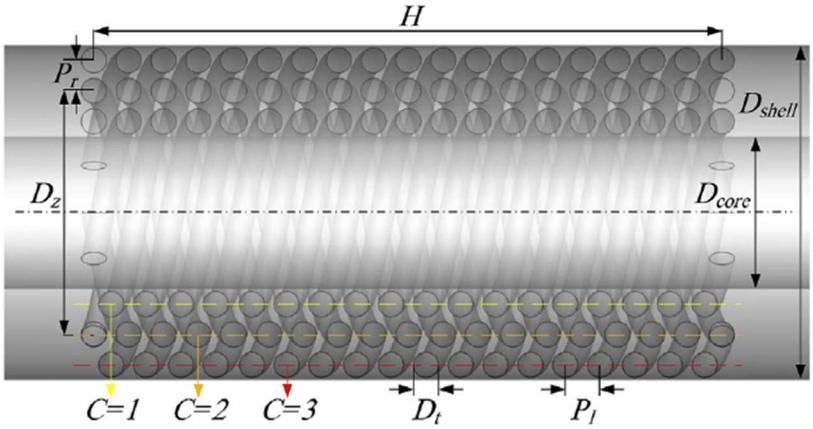

Figure 1.20. Sprial wound heat exchanger showing number of layers, pitch in longitudinal and radial direction [30].

In 2019, Sharqawy et al. conducted experiments to investigate the effects of flow configuration on the thermal performance of a spiral wound heat exchanger [31]. Three different flow configurations are shown in Figure 1.21. It was shown that the mixed axial-radial flow configuration led to the highest heat transfer coefficient as well as friction factor, followed by the axial and radial flow configuration. Correlations of Nu, Colburn-j factor and friction factor based on Re were developed for the three configurations.

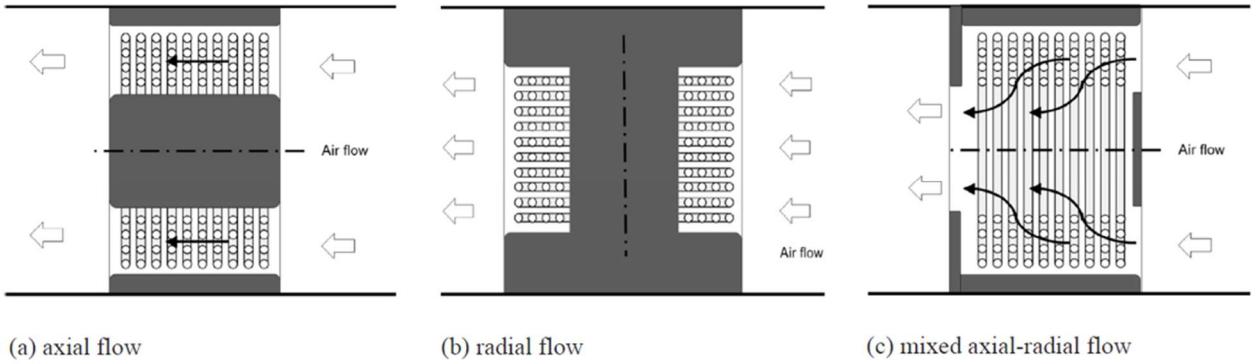

Figure 1.21. Three different configurations [31].

It should be noticed from the above studies that there are many geometry parameters in spiral wound heat exchangers or heat exchangers with various helical structures, some of which have little influence on the thermal performance of the heat exchanger while others make a big difference. To estimate the effect of the geometrical factors on flow and heat transfer and optimize the design, many researchers adopted the Taguchi method, which was invented by Taguchi and usually used in quality engineering and experimental design [32 33 34].

1.6. Content of this study

This study intends to design a novel recuperator based on meso-scale helical tube bundles. According to previous research, the flow and heat transfer characteristics in micro- and meso-scale channels are complicated and still unclear. Whether the transition to turbulence can be influenced by the characteristic length or other parameters rather than just by Re needs further exploration. Most studies on heat exchangers with various helical structures used the standard methods for conventional scale tubing (>1mm). Fluid flow and heat transfer characteristics for meso-scale helical tube heat exchangers should be explored numerically and experimentally, for both shell side and coil side. Most CFD simulation work adopted the $k-\varepsilon$ model (including RNG $k-\varepsilon$,

Realizable $k-\varepsilon$ and Standard $k-\varepsilon$), while the Shear Stress Transport $k-\omega$ model is said to be a more suitable option when predicting the details of the wall boundary layer characteristics. The applicability of those different turbulent models on this kind of geometry should be further explored.

In spiral wound heat exchangers, the coil diameters of the inner tubes on different layers are quite different, which will result in a large variation of the internal flow heat transfer coefficient [23]. This problem will further lead to a non-uniform flow and temperature distribution in both tube- and shell-side, reducing the effectiveness. In this paper, a novel geometry using twisted helical meso-scale tube-bundles with same length and coil diameter is proposed, of which the thermal performance has been studied and compared with that of spiral wound geometry.

In this study, for both the coil side and shell side, different models including Laminar, $k-\varepsilon$, $k-\omega$ and large eddy simulation (LES) are compared by simulating geometries which have been tested by experiments, specifically a helical microtube for coil side and a spiral wound heat exchanger for shell side. Eventually the SST $k-\omega$ model was used. To reduce the computational cost, Fluent simulations for the shell side flow and tube side flow are carried out separately. The thermal and hydraulic characteristics of the flow have been analyzed. Nu and friction factor correlations with Re and geometry parameters for both the shell side flow and tube side flow have been developed. These correlations are used in the whole heat exchanger model to calculate the effectiveness and pressure drop of the heat exchanger.

Another geometry tool that has been utilized to identify better thermal performance and to optimize the design, is the geometry-based conduction shape factor. Although it directly applies to solid conduction rather than convective heat transfer, it provides guidance regarding the influence of geometry on optimal thermal designs. The conduction shape factor tends to be another

characteristic length other than hydraulic diameter to describe the tube configuration, and it is included in the correlations leading to a better fitness. This study also uses the visualizations of the vortex structure of fluid flow around the twisted tube bundles and the associated analysis using the Q-criterion (described below). The relationship between average vorticity magnitude on a Q-criterion iso-surface and conductance of the heat exchanger appears promising, and this can be used to connect the fluid mixing intensity and the geometry configuration.

A whole heat exchanger design is proposed, consisting of a group of twisted tube bundles in parallel with each other and turning 180-degree turns eight different times to guarantee sufficient heat transfer length and yet meet the overall size constraints (<0.7 m height, width/length<0.3 m) simultaneously. At each of the 180-degree turns, a double header system is used to redistribute both the shell side and tube side flow.

A finite difference model is built to calculate the effectiveness and pressure drop. The pitch length has been found to have large influence on the pressure drop. To meet the pressure-drop and effectiveness requirements, the pitch length of the helical twisted tube-bundle is set as 50 mm, the tube inner diameter is set as 1 mm, and there are 432 tubes going in parallel. Several assumptions are made in the model, which may cause misestimation of the effectiveness. Accordingly, whether it is reasonable to use these assumptions or not is also discussed in this paper.

2. Geometry

2.1. Heat exchanger design specification

The overall design objectives of the sponsor are listed in Table 2.1. The working fluid is helium, and the temperature range extends from 300 K to 30 K, which means the thermal properties and the Re value of the working fluid vary significantly through the heat exchanger channel. To build a whole heat exchanger model and obtain its effectiveness and pressure drop, the Nu and friction factor correlation in a fully developed region based on the Re value and the geometry factor should be developed first, for both the tube- and shell-side. The largest acceptable pressure drop for both sides is 1 bar. The heat exchanger should achieve high effectiveness and be as compact and light as possible.

Table 2.1. Design objectives.

Working fluid	Helium
Temperature span	300 K to 30 K
Operating pressure	320 psig (supply side), 100 psig (return side)
Pressure drop	<0.5 bar for both sides (best), <1.0 bar (acceptable)
Flow rate	13 g/s
Materials	Stainless steel or copper
Mass	<60 lbs (best), <80 lbs (acceptable)
Approximate size	<0.7 m height, width/length<0.3 m
Effectiveness	>0.99 (best), >0.985 (acceptable)

2.2. Heat exchanger core geometry

2.2.1. Geometry design

A twisted helical-tube-bundle geometry is proposed in this study. First, several tubes twisting helically around each other form a bundle. Then, several bundles twisting together form

the geometry. The curve of each tube in the bundle is generated by different three-dimensional sinusoidal equations, and the equations are designed to produce the same end-to-end length and average coil diameter for each tube. This feature facilitates a uniform temperature and velocity distribution among tubes, otherwise the maldistribution will cause a larger thermal ineffectiveness.

For example, if a bundle consists of 4 tubes, then the 3D equations of each tube are shown by Equation (2.1) - (2.12). It should be noticed that each equation is basically the sum of two sine curves, where a, b are the amplitudes of each curve respectively. While the amplitude of each tube varies from (a-b) to (a+b), the bundle coil diameter equals the largest amplitude of the tubes, which is (a+b). The coefficient c relates to initial phase. The period length of the first sine curve is p, and n is set as integer, then the first sine curve period is an integer multiple of that of the second curve, which means p is also the pitch length of the tube. d is the number of tubes, in this case d = 4. The generated bundle of equation (2.1) - (2.12) is shown in Figure 2.1. Then several of the same bundles are twisted together around the mandrel to fill the heat exchanger space, which is demonstrated in Figure 2.2 with one bundle highlighted. Such an approach generates a group of tubes uniformly distributed, and among them the only difference is the phase.

$$X_{1,t} = a \cdot \cos\left(\frac{2\pi t}{p}\right) + b \cdot \cos\left(\frac{2n\pi t}{p} + c \cdot \frac{\pi}{d}\right) \tag{2.1}$$

$$Y_{1,t} = a \cdot \sin\left(\frac{2\pi t}{p}\right) + b \cdot \sin\left(\frac{2n\pi t}{p} + c \cdot \frac{\pi}{d}\right) \tag{2.2}$$

$$Z_{1,t} = t \tag{2.3}$$

$$X_{2,t} = a \cdot \cos\left(\frac{2\pi t}{p}\right) + b \cdot \cos\left(\frac{2n\pi t}{p} + (c+2) \cdot \frac{\pi}{d}\right) \tag{2.4}$$

$$Y_{2,t} = a \cdot \sin\left(\frac{2\pi t}{p}\right) + b \cdot \sin\left(\frac{2n\pi t}{p} + (c+2) \cdot \frac{\pi}{d}\right) \tag{2.5}$$

$$Z_{2,t} = t \tag{2.6}$$

$$X_{3,t} = a \cdot \cos\left(\frac{2\pi t}{p}\right) + b \cdot \cos\left(\frac{2n\pi t}{p} + (c+4) \cdot \frac{\pi}{d}\right) \tag{2.7}$$

$$Y_{3,t} = a \cdot \sin\left(\frac{2\pi t}{p}\right) + b \cdot \sin\left(\frac{2n\pi t}{p} + (c+4) \cdot \frac{\pi}{d}\right) \tag{2.8}$$

$$Z_{3,t} = t \tag{2.9}$$

$$X_{4,t} = a \cdot \cos\left(\frac{2\pi}{p}\right) + b \cdot \cos\left(\frac{2n\pi t}{p} + (c+6) \cdot \frac{\pi}{d}\right) \tag{2.10}$$

$$Y_{4,t} = a \cdot \sin\left(\frac{2\pi t}{p}\right) + b \cdot \sin\left(\frac{2n\pi t}{p} + (c+6) \cdot \frac{\pi}{d}\right) \tag{2.11}$$

$$Z_{4,t} = t \tag{2.12}$$

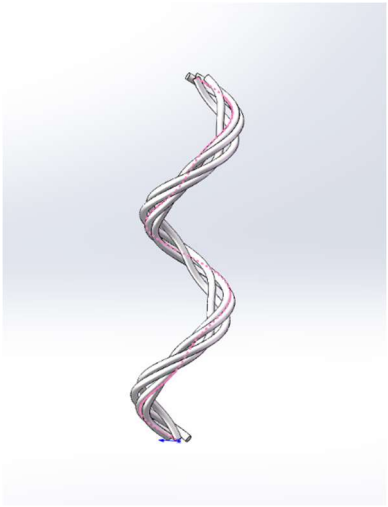

Figure 2.1. A bundle of 4 tubes.

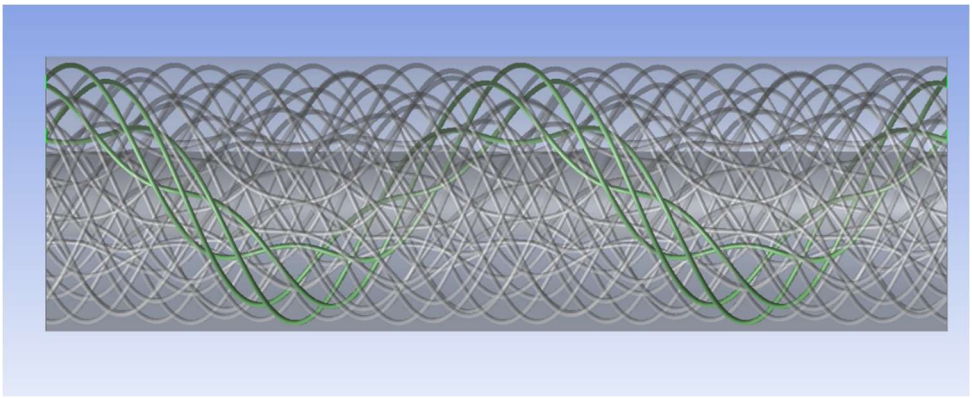

Figure 2.2. Whole geometry (100 mm long part) with one bundle highlighted.

2.2.2. Geometry features

Both spiral wound heat exchanger geometry and twisted helical bundle geometry configurations are shown in Figure 2.3. Spiral wound heat exchanger contains many layers of helically coiled tubes and is already widely used in various industrial fields. For the spiral wound geometry shown in Figure 2.3(a), the pitch on each layer is related to their coil diameter so that the tubes in different layers also end up with the same length, thereby avoiding a non-uniform flow distribution. However, most of the fluid in the shell-side passes directly through the gap between two adjacent layers, which weakens the turbulence and the associated heat transfer coefficient. Also from Figure 2.3, it is demonstrated that in a spiral wound heat exchanger, tubes in each layer stay in the same layer without changing their position in the radial direction, while in twisted helical bundle heat exchanger, all tubes continually change their position in the radial direction by spiraling inward and outward during one revolution. This could enhance the fluid mixing and promote uniformity of the temperature distribution in the radial direction.

Two longitudinal (which means parallel to the axial direction) cross sections staggered by 35° of the twisted helical bundle geometry are shown in Figure 2.4. Unlike those of the spiral wound geometry, the shapes of the longitudinal cross sections vary in the circumferential direction,

and the continuously changing cross-sectional shape is expected to enhance the heat transfer coefficient. The comparison of these two geometries from the inlet view is shown in Figure 2.5. It is reasonable to expect that the flow will move across more tube banks in the twisted helical bundle heat exchanger, which could augment fluid mixing and meanwhile increase both form drag and friction drag.

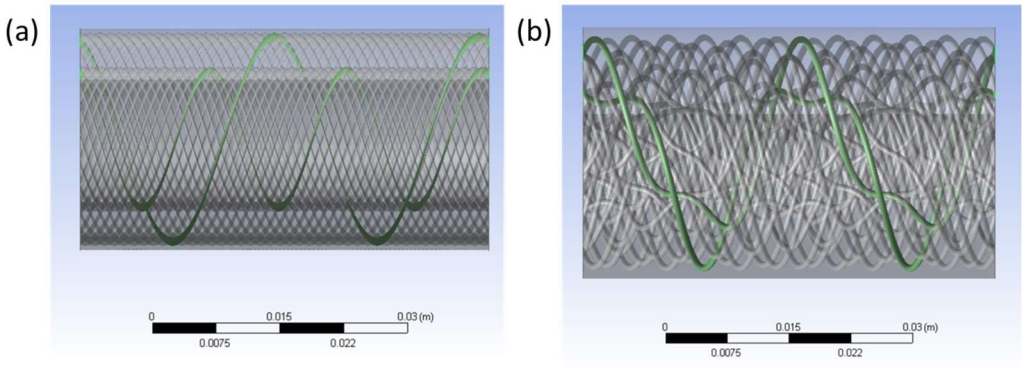

Figure 2.3. Comparison of how tube wound in (a) spiral wound heat exchanger (b) twisted helical-tube-bundle heat exchanger.

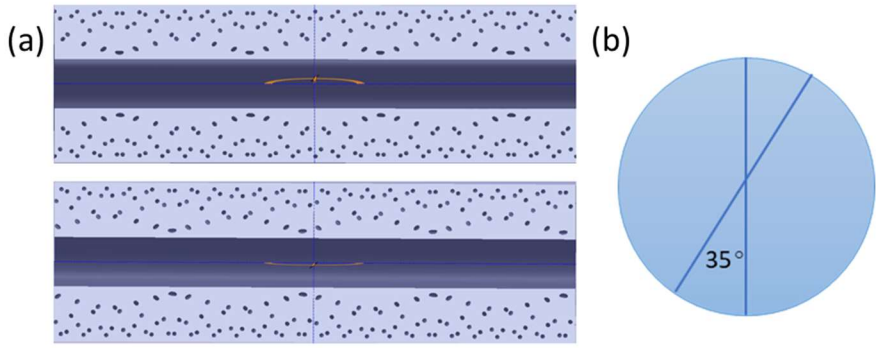

Figure 2.4. (a) The distribution of tubes on two longitudinal cross sections staggered by 35°, (b) The relative position of the two cross sections from the inlet view.

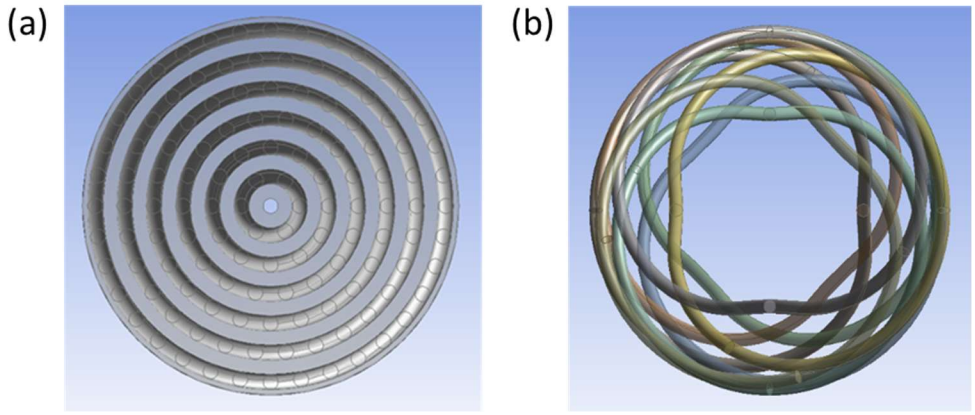

Figure 2.5. Comparison of (a) spiral wound heat exchanger (b) twisted helical-tube-bundle heat exchanger from the inlet view.

2.2.3. Parameters of concern

All features mentioned above will increase the heat transfer coefficient as well as the pressure drop, as there is always some trade-off between high heat transfer coefficient and low pressure drop. To satisfy both effectiveness and pressure drop requirements, the influence of various geometry parameters on both thermal and hydraulic performance should be quantified. In other words, the correlations of Nu and friction factor based on the geometry parameters should be built.

The twisted helical bundle geometry can be specified by number of bundles, number of tubes in one bundle, amplitude of tubes, pitch length and tube diameter. To build the correlations of Nu and friction factor and optimize the design, geometries with different combinations of parameter values have been simulated using Fluent, and the influence of these geometry factors have been explored.

3. Shell side CFD Model

Time cost and memory requirement of meshing and simulating the whole geometry are unbearably high since there could be more than one hundred million cells for a 100 mm long part. Therefore, the shell side flow and tube side flow are simulated respectively. The shell side model is introduced in this chapter, including geometry, mesh generation, governing equations and model verification.

3.1. Shell side geometry and parameter of concern

The shell side flow is the type of flow that continuously goes across a bunch of tubes at different angles. The number of tubes and the tube diameter each have a large influence on the heat transfer area. The development of the boundary layer and flow separation are closely related to the angle of the tubes, so the pitch length is also an important parameter. The tube number and pitch length also decide the distance between tubes in the axial direction, which determines the space for vortex shedding and turbulence development.

Based on above analysis, the tube number, pitch length and tube diameter are all important to both thermal and hydraulic performances. To explore their influences and optimize the design, different values of these parameters are chosen and combined to build different shell side geometry, and the values of geometric parameters are shown in Table 3.1. For the tube number parameter, both the tube number in one bundle and the number of bundles are changed. And even for the geometry with same tube number, there are different arrangements, e.g., a geometry consisting of 9 bundles of 4 tubes and a geometry consisting of 6 bundles of 6 tubes.

Table 3.1. Values of geometry parameters.

Tube diameter (mm)	0.6, 0.8, 1
Pitch length (mm)	25, 40, 50
Tube number and distribution (m×n means one bundle consists of m tubes and the geometry consists of n bundles)	36 (6×6, 4×9) 30 (6×5, 6×5) 28 (4×9) 27 (3×9) 25 (5×5) 20 (2×10)

3.2. Mesh generation

For the shell side model, the mesh is generated using the tetrahedral independent method. Since there are many curves and small gaps in the geometry, not only the maximum and minimum cell size but also the curvature normal angle and the number of cells across a gap have a large influence on the cell, as shown in table 3.2. The curvature normal angle is the maximum angle that one mesh's face or surface can span. The number of cells across a gap is the minimum number of layers of cells generated in the gaps. These parameters have been manipulated to obtain different cell numbers for the mesh independence analysis, and results show that the heat transfer coefficient and pressure drop tend to be steady when the number of cells is larger than 9.6 million, for a shell side twisted model with 36 tubes, a pitch length of 50 mm and a whole length of 50 mm. The size settings of the mesh are listed in Table 3.3. One example mesh is shown in Figure 3.1, and the minimum orthogonal quality is around 0.367.

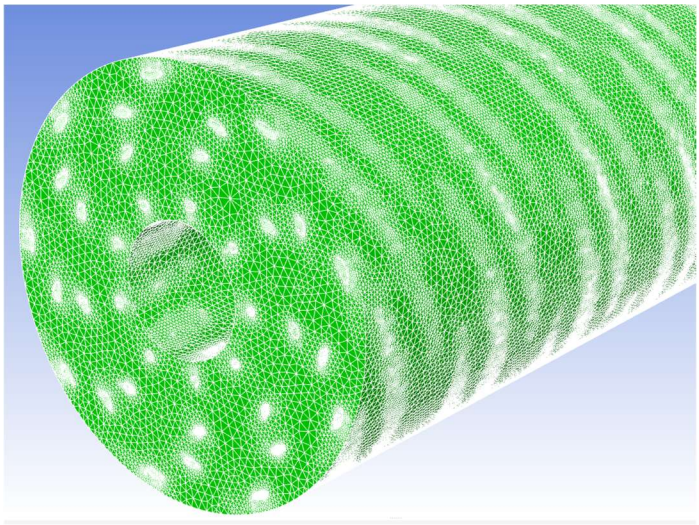

Figure 3.1. The mesh of a geometry with 9 bundles, 4 tubes in one bundle.

Table 3.2. The influences of curvature normal angel and number of cells across a gap on cell number.

Case number	Mesh size(m)	Max size (m)	Curvature normal angle (°)	Number cells across gap	Cell number
1	2e-3	2.5e-3	15	4	5108669
2	2e-3	3e-3	14	5	8164476
3	2e-3	2.5e-3	14	5	8164549

Table 3.3. Sizing of mesh.

Method	Patch independent tetrahedrons
Max size (m)	2e-3
Growth rate	1.2
Curvature min size (m)	1e-4
Curvature normal angle	15 °
Proximity Min size (m)	1e-4
Number cells across gap	4

3.3. Turbulence model

3.3.1. Flow properties

The heat exchanger uses helium gas as the working fluid and operates between 300 K and 30 K. Since the thermal properties of helium vary significantly in this temperature range, which are shown in Figure 3.2-3.4, as does the Re value along the heat exchanger, thermal variation should be considered when calculating the whole heat exchanger effectiveness. A fully developed region of the shell side flow is simulated to obtain the Nu value and friction factor correlations based on the Re value and geometry parameter. Each geometry should be simulated under different working conditions to explore the dependence on Re value. The simulation is carried out under 3 inlet temperatures, 30 K, 160 K and 300 K respectively. Since the simulation domain is short (100 mm), the changes of thermal properties due to temperature variation are negligible, accordingly the thermal properties are assumed to be constant in each case.

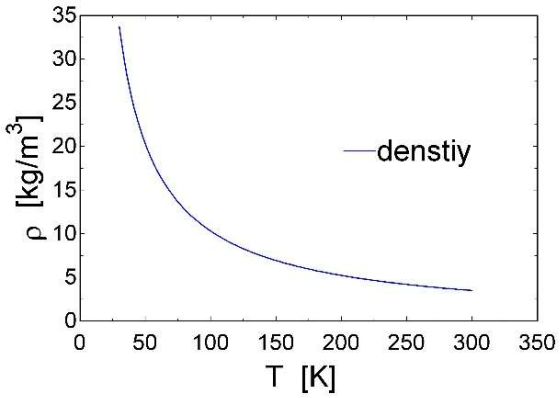

Figure 3.2. The variation of helium density with temperature under 2200 kPa.

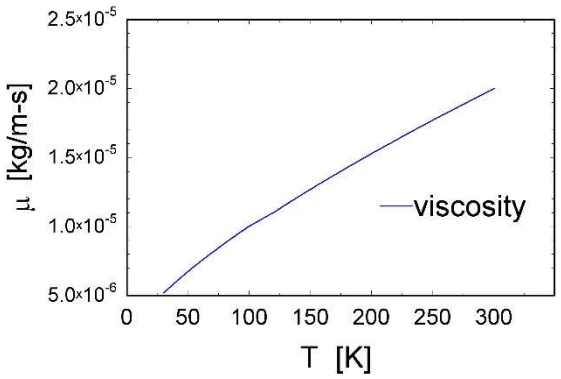

Figure 3.3. The variation of helium viscosity with temperature under 2200 kPa.

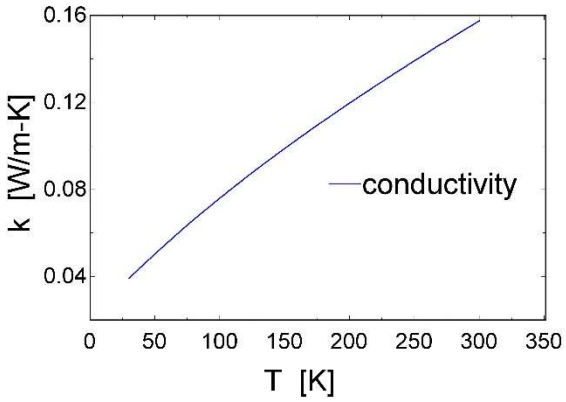

Figure 3.4. The variation of helium thermal conductivity with temperature under 2200 kPa.

3.3.2. Governing equations

Turbulence model used in the Fluent simulation is introduced in this section. The SST k-ω model is adopted in this case. The k-ω model belongs to the class of two-equation models, which employs the turbulent viscosity hypothesis to relate the Reynolds stresses to the mean velocity gradients. Consequently, the Reynolds-averaged Navier-Stokes (RANS) equations can be complete.

In Reynolds averaging, the velocity field $u(x,t)$ is decomposed into its mean and the fluctuation:

$$u_i = \bar{u}_i + u_i' \tag{3.1}$$

where $\bar{u}_i$ and u_i' are the mean and fluctuating velocity components respectively, and the equations in this section follow the Einstein summation convention. The RANS equations are derived by substituting this decomposition into the continuity and momentum equations, taking an average and dropping the overbar on the mean velocity. With the solution variables representing averaged values, the RANS equations almost have the same appearance as the Navier-Stokes equations, except an extra term, i.e., the Reynolds stresses $\overline{u_i'u_j'}$. Therefore, there are more unknowns than equations and the equations are uncomplete.

$$\frac{\partial \rho}{\partial t} + \frac{\partial (\rho u_i)}{\partial x_i} = 0 \tag{3.2}$$

$$\frac{\partial u_i}{\partial t} + u_j \frac{\partial u_i}{\partial x_j} = -\frac{1}{\rho}\frac{\partial p}{\partial x_i} + \nu \frac{\partial}{\partial x_i}\left(\frac{\partial u_i}{\partial x_j} + \frac{\partial u_j}{\partial x_i}\right) + \frac{\partial}{\partial x_i}\left(-\overline{u_i'u_j'}\right) \tag{3.3}$$

To make the equations complete, the Reynolds stresses should be determined by a turbulence model. One common approach is via the turbulent viscosity hypothesis, according to which the Reynolds stresses are given by

$$\overline{u_i'u_j'} = \frac{2}{3}k\delta_{ij} - \frac{\mu_t}{\rho}\left(\frac{\partial u_i}{\partial x_j} + \frac{\partial u_j}{\partial x_i}\right) \tag{3.4}$$

Where k and $\mu_t$denote the turbulent kinetic energy and turbulent viscosity. In the two-equation models, two additional transport equations are solved to obtain two other turbulence parameters, e.g., k and the turbulence dissipation rate ε in k-ε model, k and the specific

dissipation rate ω the in k-ω model etc. Then the turbulent viscosity can be calculated by these two variables. The transport equations for k and ω are shown below:

$$\frac{\partial}{\partial t}(\rho k) + \frac{\partial}{\partial x_i}(\rho k u_i) = \frac{\partial}{\partial x_j}\left(\Gamma_k \frac{\partial k}{\partial x_j}\right) + G_k - Y_k \tag{3.5}$$

$$\frac{\partial}{\partial t}(\rho \omega) + \frac{\partial}{\partial x_i}(\rho \omega u_i) = \frac{\partial}{\partial x_j}\left(\Gamma_\omega \frac{\partial \omega}{\partial x_j}\right) + G_\omega - Y_\omega \tag{3.6}$$

Where G_k and G_ω respectively denote the generation of k and ω due to the mean velocity gradients. Y_k and Y_ω are the dissipation of k and ω due to turbulence. Γ_k and Γ_ω are the effective diffusivity of k and ω. These terms are modeled as described below.

The production of k and ω:

$G_k = \mu_t S^2$, S is the modulus of the mean rate-of-strain tensor

$$G_\omega = \alpha \frac{\omega}{k} G_k \tag{3.7}$$

where

$$\alpha = \frac{\alpha_\infty}{\alpha^*}\left(\frac{\alpha_0 + Re_t/R_\omega}{1 + Re_t/R_\omega}\right) \tag{3.8}$$

$$\alpha^* = \alpha_\infty^*\left(\frac{\alpha_0^* + Re_t/R_\omega}{1 + Re_t/R_\omega}\right) \tag{3.9}$$

$$Re_t = \frac{\rho k}{\mu \omega} \tag{3.10}$$

with constants $R_k = 6, \alpha_0^* = 0.024, \alpha_\infty^* = 1, \alpha_\infty = 0.52, \alpha_0 = \frac{1}{9}$.

The dissipation of k and ω:

$$Y_k = \rho \beta^* f_{\beta^*} \omega^2 \tag{3.11}$$

$$Y_\omega = \rho\beta f_\beta \omega^2 \tag{3.12}$$

Since the calculation of $\beta^*, f_{\beta^*}, \beta, f_\beta$ and related constants is kind of cumbersome and irrelevant to the subject of this study, it is not listed here and detailed formulas can be found in the fluent theory guide [35].

The effective diffusivities of k and ω:

$$\Gamma_k = \mu + \frac{\mu_t}{\sigma_\kappa} \tag{3.13}$$

$$\Gamma_\omega = \mu + \frac{\mu_t}{\sigma_\omega} \tag{3.14}$$

Where σ_κ and σ_ω are the turbulent Prandtl number for k and ω. The turbulent viscosity μ_t is obtained by k and ω.

$$\mu_t = \frac{\rho k}{\omega} \frac{1}{\max\left[\frac{1}{\alpha^*}, \frac{SF}{0.31\omega}\right]} \tag{3.15}$$

Where

$$F = tanh\left(max\left[2\frac{\sqrt{k}}{0.09\omega y}, \frac{500\mu}{\rho y^2 \omega}\right]\right) \tag{3.16}$$

S is the strain rate magnitude and y is the distance to the next surface

Here, in the SST $\kappa - \omega$ model, the turbulent viscosity formula is modified based on the standard $\kappa - \omega$ model, to account for the transport effects of the principal turbulent shear stress [35]. The transport turbulent shear stress is significantly important when predicting the onset and amount of flow separation from smooth surfaces. In consequence, the SST k-ω model is more accurate and reliable for a class of flows, like flow across airfoils and the shell side flow across tubes in our case.

3.3.3. Boundary conditions

The boundary conditions are shown in Figure 3.5. Both the wall of the mandrel and the outer wall are adiabatic. The velocity and temperature are specified at the inlet and the pressure is specified at the outlet. A constant heat flux boundary condition is used on the wall where heat transfer occurs.

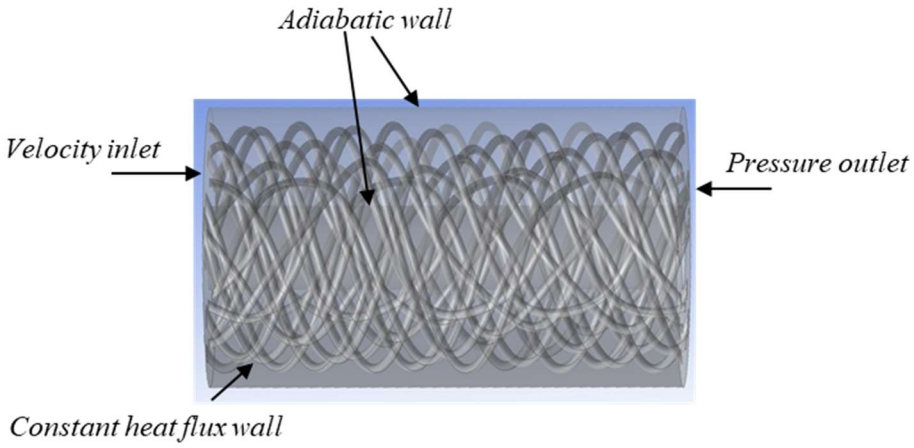

Figure 3.5. Boundary conditions of the shell side flow model.

Since the amount of heat flux ($20W/m^2$) applied to the wall is small compared to the real value in such kind of heat exchanger, the temperature of the flow in the domain is close to uniform, as is that of the wall. Accordingly, the difference between the average flow temperature and the average wall temperature is used to calculate the heat transfer coefficient. The hydraulic diameter is defined as four times the volume of flow region divided by the heat exchange area. Since both the wall of the mandrel and the shell wall are adiabatic, then they do not need to be considered when calculating the Nu value. However, when flow passes along these two walls, it is affected by friction drag due to shear stress. Therefore, the area of these two walls is considered when

calculating the friction factor, which means two different hydraulic diameter definitions are used for heat transfer problem and pressure drop problem respectively:

$$D_{h,Nu} = \frac{4V}{A_{exchange}} \tag{3.17}$$

$$D_{h,f} = \frac{4V}{A_{exchange}+A_{shell}+A_{mandrel}} \tag{3.18}$$

The corresponding Re values are defined by:

$$Re_{Nu} = \frac{\rho u D_{h,Nu}}{\mu} \tag{3.19}$$

$$Re_f = \frac{\rho u D_{h,f}}{\mu} \tag{3.20}$$

The Nu value is calculated using equation (3.21-3.22), where q is the heat flux at the helical tube bundles, $\overline{T_{wall}}$ is the average wall temperature, and $\overline{T_{bulk}}$ is the average bulk temperature. The friction factor is calculated using equation (3.23-3.24).

$$h = \frac{q}{\overline{T_{wall}}-\overline{T_{bulk}}} \tag{3.21}$$

$$Nu = \frac{hD_{h,Nu}}{K} \tag{3.22}$$

$$\Delta P = P_{in} - P_{out} \tag{3.23}$$

$$f = \frac{2\Delta P D_{h,f}}{\rho L {U_{in}}^2} \tag{3.24}$$

3.3.4. Entrance effect and computational domain

When simulating the model with a whole length of 50 mm, it has been found that even under similar Re values, the Nu value at 30 K is much smaller than that at 300 K. For example,

for a model with 36 tubes and a Re value around 2400, the Nu value at 30 K is 61.8 while for the same Re value, the Nu value at 300 K is 101.8. One possible explanation is that the entrance effect and transition to turbulence may be different for the two cases. Exploring this idea, the Nusselt number and friction factor have been determined for different sections of the modelled geometry, as shown in Table 3.4. The Re values are calculated based on the velocity at the inlet of each section. Both values associated with the second half of the geometry are smaller than those averaged over the whole geometry, while those from the fourth quarter increase again. These values indicate that the flow has not reached the fully developed region in the 50 mm long model, and the entrance effect is promoted by high temperature and high velocity.

To reduce the influence of the entrance effect, the length of the geometric model is extended to 100 mm. Both the Nusselt number and friction factor calculated from various parts of this model are shown in Figure 3.6 and Figure 3.7. For all three working conditions, the change of both values from the second half to the last quarter is small, less than 1%, which indicates that the flow is fully developed in the second half. It should be noticed that for a 100 mm long model, the Nu value at 30 K is a little larger than that at 300 K, even though the Re value at 30 K is a little smaller, while as described above, for a 50 mm long model, the Nu value at 30 K is much smaller than that at 300 K. This difference may be caused by an early transition to turbulence under high temperature and high velocity. An experimental study also found that with a high inlet temperature and velocity, the transition occurs earlier and the transition zone in which the Nusselt number remain constant is longer [13]. More data under different working conditions is needed to explain this phenomenon. In the following part of this thesis, the Nu and friction factor are calculated from the second half of the 100 mm long models.

Table 3.4. Nu and friction factor calculated from different parts, for a model 50 mm long.

	Inlet temperature (K)	Inlet velocity(m/s)	Re	Nu	Friction factor
Whole	300	1.5001	2442.5	101.8	1.30
Second half	300	1.8214	2965.6	96.8	0.77
Fourth quarter	300	1.6269	2648.9	98.4	0.95

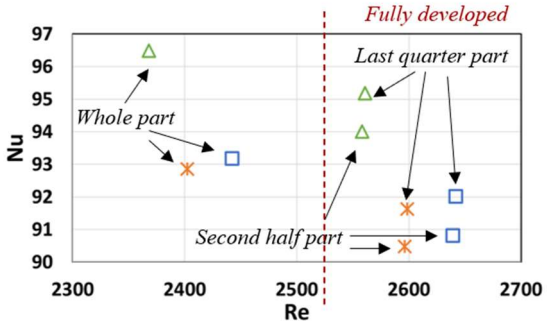

Figure 3.6. Nu calculated from different parts of a 100 mm long model.

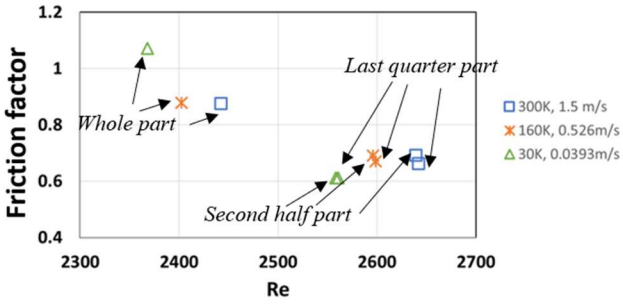

Figure 3.7. Friction factor calculated from different parts of a 100 mm long model.

3.4. Model verification

Fluent is used to simulate the heat transfer performance of a short shell-side part of this novel geometry. There is no experimental data for this twisted helical bundle heat exchanger yet. By simulating a spiral wound heat exchanger using different turbulence equations (k-epsilon model, k-omega model, and LES model) and comparing the results with experimental data from literature, the k-omega model is found to be the most suitable one to simulate this kind of geometry.

The comparison for shell side flow was carried out by simulating the heat exchangers with helical coils tested in literature [29]. The geometry and mesh are shown in Figure 3.8. The diameter

of the small tube is 10 mm, the pitch length of the tube at the first layer is 26.24 mm and that of the tube at the second layer is 39.38 mm, and the coil diameter is 70 mm and 92 mm at the two layers respectively. The mesh is generated using the patch independent tetrahedron method. In this case, a sweep method is not applicable since the ratio of pitch and coil diameter is too small. The working fluid is water with a mass flow rate of 0.56 – 2.24 kg/s and an inlet temperature of 293 K. A constant heat flux boundary condition is used. The comparison between the different models is shown in Figure 3.9. Nu_cor is the Nu value calculated from the correlation developed from the experimental data, so it demonstrates that the $k-\omega$ model has a slightly better agreement with the experimental data than the $k-\varepsilon$ model, and the advantage becomes more obvious as Re value increases.

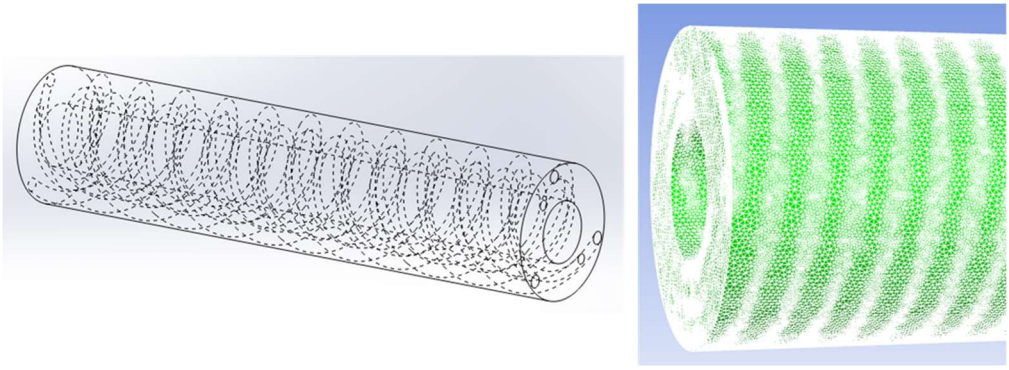

Figure 3.8. Shell side computation domain and mesh for model comparison.

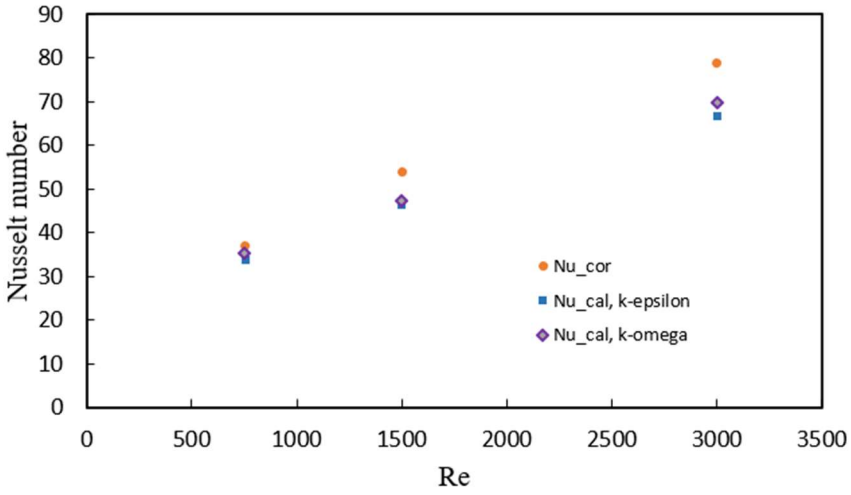

Figure 3.9. Comparison among various models for shell side flow.

4. Shell side simulation result analysis

Fluent simulation is carried out on 17 different shell side geometries under 6 different working conditions. In this chapter, the thermal and hydraulic performance of different geometries and the influence of geometric parameters are analyzed both qualitatively and quantitatively. To qualitatively demonstrate the difference between geometries, the flow and temperature profiles are displayed and compared. To quantify the influence of various geometric parameters, the Nu value and friction factor of different geometries are obtained and correlations are developed. The geometry providing the largest shell side conductance is determined. To study the mechanism behind the relation between the geometry and the heat transfer capacity, the vortex visualization method is utilized, and the vorticity magnitude of flow is computed and analyzed.

4.1. Flow field and temperature field of different geometries

In this section, the flow and temperature fields of two geometries are compared, one with 36 tubes (6×6), pitch length as 25 mm and tube diameter as 0.8 mm (Figure 4.1), the other with 20 tubes (2×10), pitch length as 50 mm and tube diameter as 0.6 mm (Figure 4.2). It should be noted that the first geometry is more compacted than the latter.

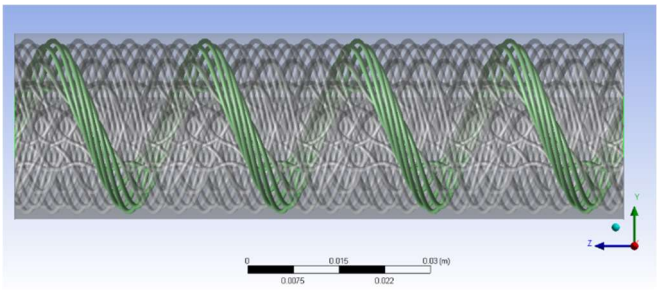

Figure 4.1. Geometry with 36 tubes, pitch length as 25 mm and tube diameter as 0.8 mm, with one bundle of 6 tubes highlighted.

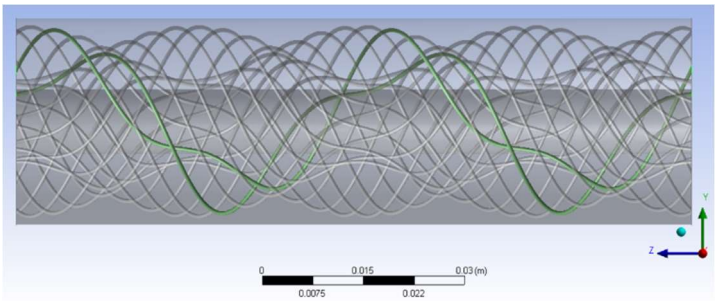

Figure 4.2. Geometry with 20 tubes, pitch length as 50 mm and tube diameter as 0.6 mm, with one bundle of 2 tubes highlighted.

For the geometry with 36 tubes, pitch length 25 mm and tube diameter 0.8 mm, the temperature distributions at steady state of two sections perpendicular to each other and parallel to the axis direction are shown as Figure 4.3. It is demonstrated that the distribution of tubes on the two sections are quite different. While the distribution of tubes in the radial direction in both sections seems not uniform, every tube continually changes its radial position in one cycle. These spiral-in-and-out tubes promote the fluid mixing, and the distribution of temperature in the radial direction tends to be more and more uniform along the flow direction.

The temperature and velocity distributions of the sections perpendicular to the axis direction under steady state are shown in Figure 4.4 and Figure 4.5 respectively. Each section is separated by 10 mm and the distribution of tubes on the section also varies with the position. In the first half (the left half) of the geometry, the temperature and velocity distributions change a lot, which implies a developing region. In the second half of the geometry, the distributions tend to be steady, and a fully developed region is assumed. Thus, the average Nu value and friction factor are calculated from the second half of the geometry.

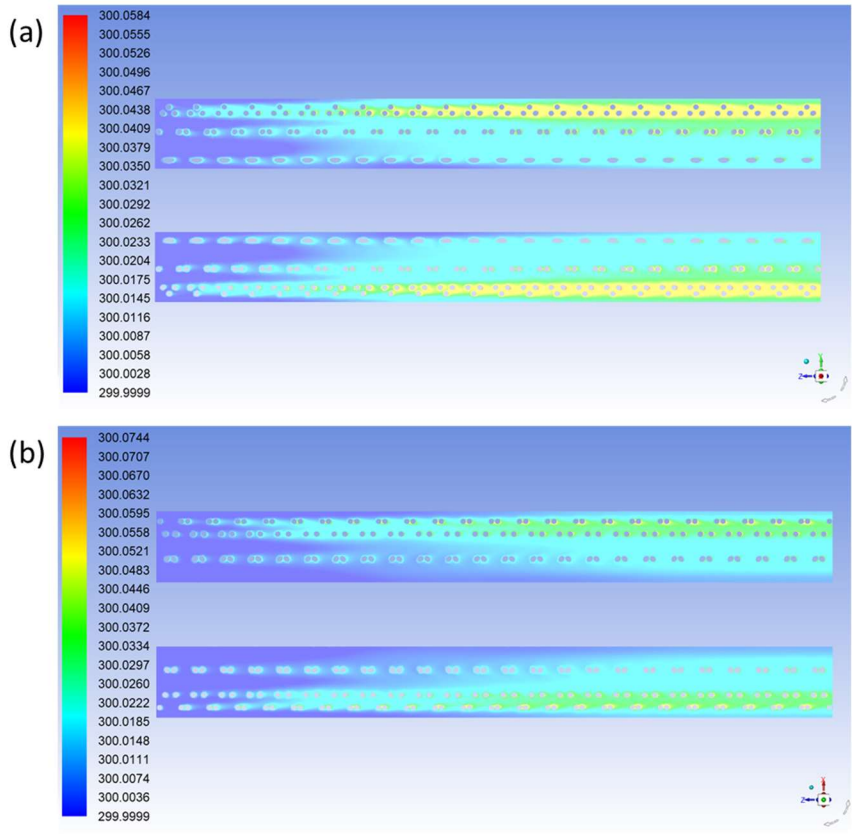

Figure 4.3. The temperature distributions of two sections perpendicular to each other and parallel to the axis direction. (a) iso-surface x=0, (b) iso-surface y=0.

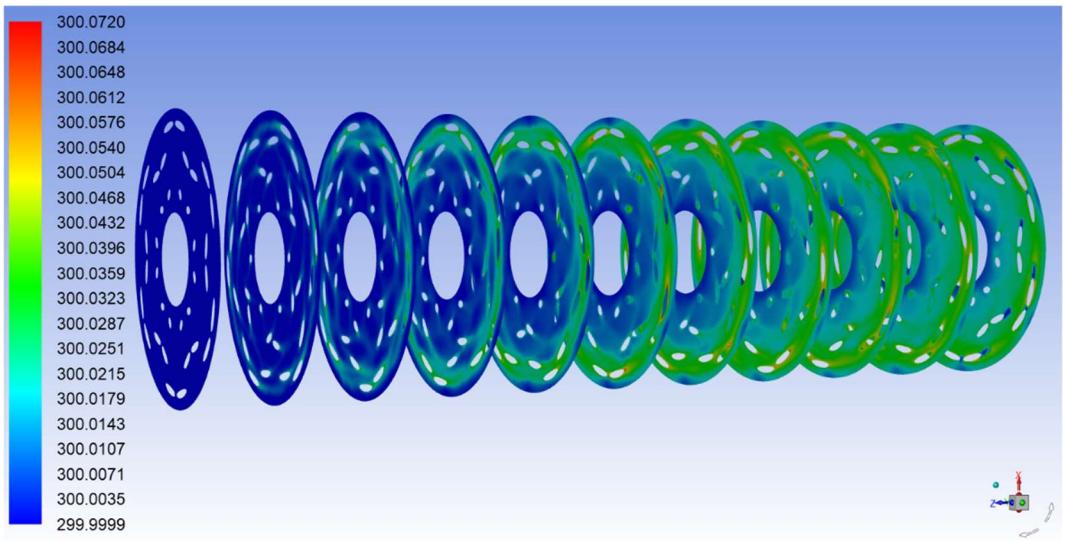

Figure 4.4. Temperature field under steady state of the geometry with 36 tubes, pitch length 25 mm, tube diameter 0.8 mm.

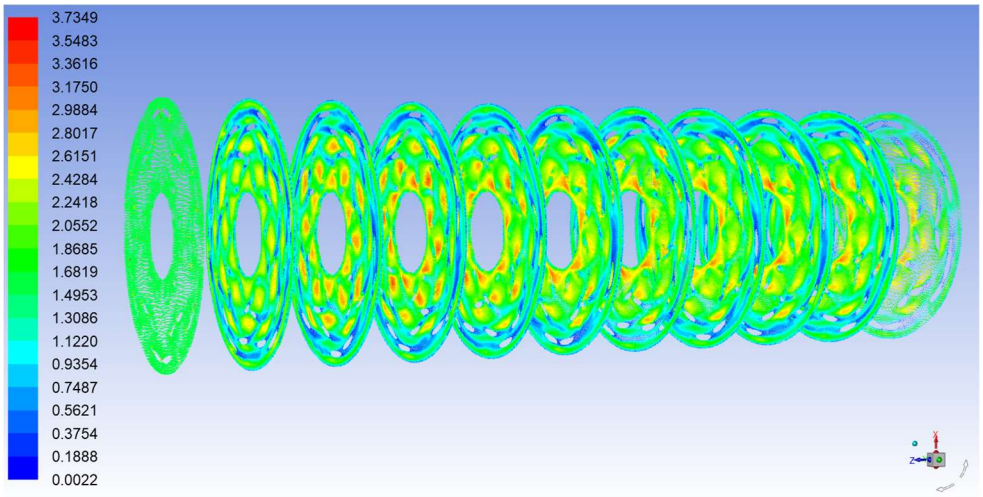

Figure 4.5. Velocity field (m/s) under steady state of the geometry with 36 tubes, pitch length 25 mm, tube diameter 0.8 mm.

For the geometry with 20 tubes, pitch length 50 mm and tube diameter 0.6 mm, the temperature and velocity distributions are shown as Figure 4.6 and 4.7 respectively. Compared with the geometry with 36 tubes, the distributions seem more uniform, while the temperature barely increases in the first half (left half) of the geometry.

Counterintuitively, this less compact geometry provides a larger Nu value and friction factor. Since there is more space behind each tube for a vortex structure to develop, both the heat transfer coefficient and friction factor are larger compared to those of the geometry with 36 tubes. However, due to a smaller tube number, longer pitch length and smaller tube diameter, the heat transfer area of the geometry with 20 tubes is much smaller than that of the geometry with 36 tubes, therefore a larger Nu value does not guarantee a larger conductance. In fact, the conductance of this geometry with 20 tubes is smaller than that of the geometry with 36 tubes, even with a larger Nu value, which will be discussed in the following sections.

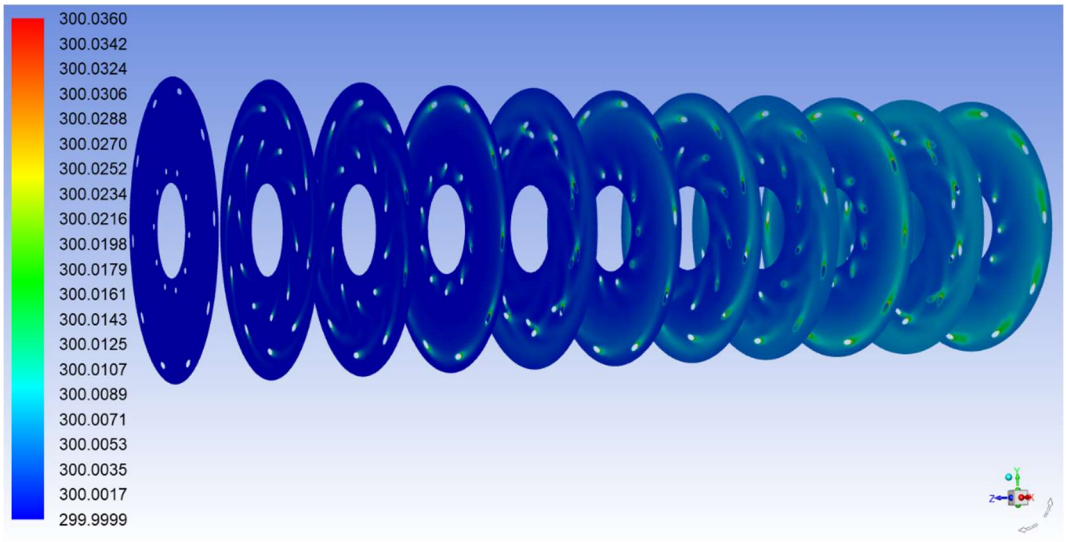

Figure 4.6. Temperature field under steady state of the geometry with 20 tubes, pitch length 50 mm, tube diameter 0.6 mm.

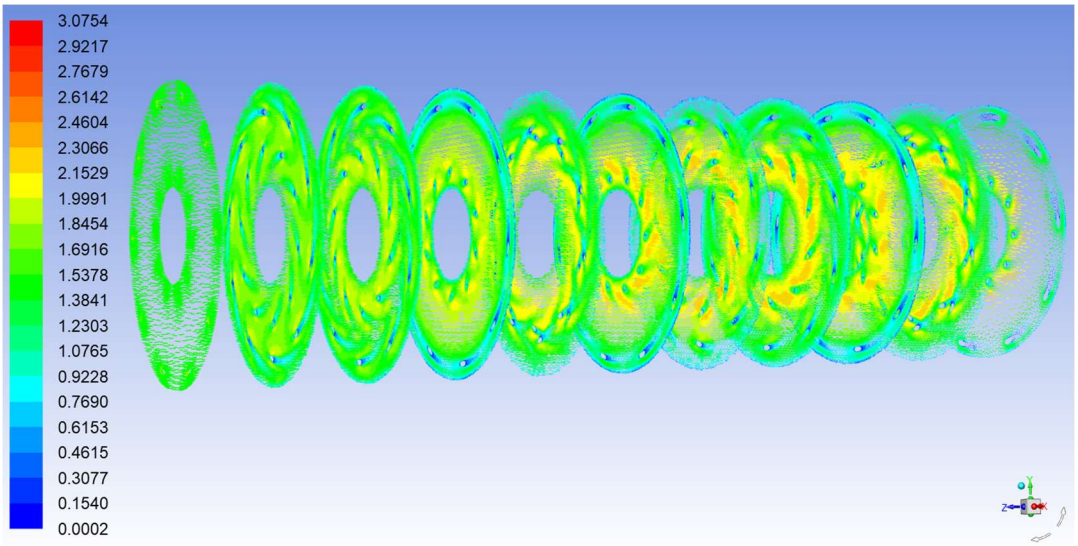

Figure 4.7. Velocity field under steady state of the geometry with 20 tubes, pitch length 50 mm, tube diameter 0.6 mm.

4.2. Nu and friction factor correlation

4.2.1. Introduction of conduction shape factor

The thermal performance of the twisted helical tube heat exchanger is influenced strongly by geometry parameters. Tube number, pitch value, inner tube diameter and tube distribution have been explored. The dimensionless pitch value is defined by the following equation, where p is the pitch length, D is the inner tube diameter.

$$\tilde{p} = \frac{p}{D} \tag{4.1}$$

It should be noticed that two completely different configurations can have the same dimensionless pitch length, e.g., a geometry with p=25 mm, D=0.5 mm and a geometry with p=50 mm and D=1 mm, shown in Figure 4.8. Two geometries with the same tube number, pitch length and inner tube diameter will have the same dimensionless pitch length and hydraulic diameter, but their configurations could be very different, e.g., a geometry with 4 tubes in one bundle, 9 bundles in total and a geometry with 6 tubes in one bundle, 6 bundles in total, or a more extreme case shown in Figure 4.9. A different distribution of tubes may lead to a different separation area formed behind tubes, which will have a large influence on the vortex shedding and the form drag, leading to different heat transfer and hydraulic performances.

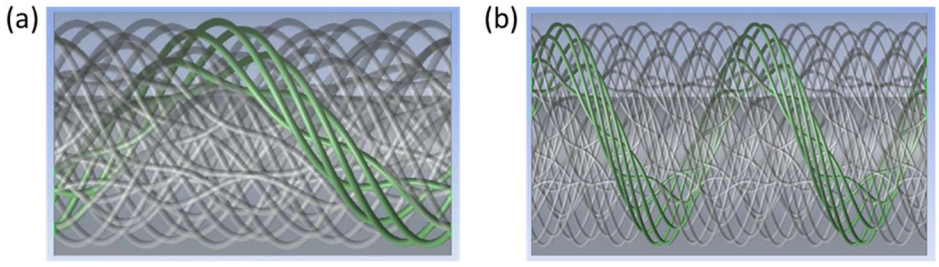

Figure 4.8. (a) geometry with pitch length as 50 mm and tube diameter as 1 mm, (b) geometry with pitch length as 25 mm and tube diameter as 0.5 mm.

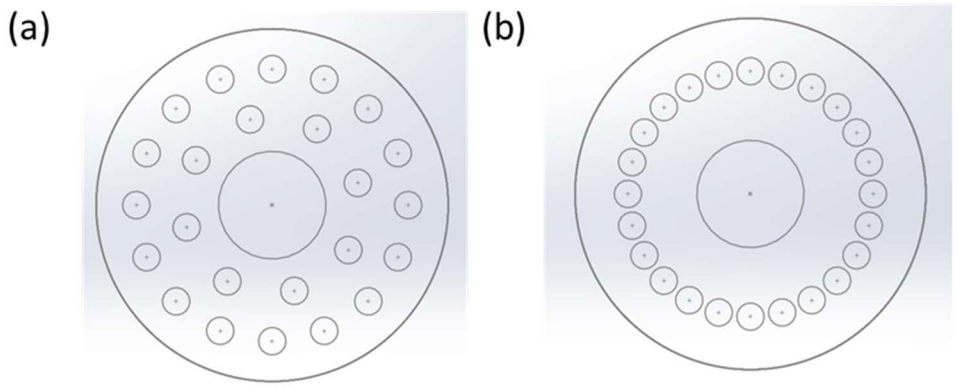

Figure 4.9. Extreme case of two totally different configurations with the same hydraulic diameter and Re value.

Therefore, there exist limitations to use hydraulic diameter and dimensionless pitch length to describe and specify the geometries. To quantify the intrinsic geometric relationship of tubes in a specific geometry, a concept from conductive heat transfer purview is "borrowed", which is the conduction shape factor S defined as:

$$S = \frac{1}{kR} \tag{4.2}$$

Where k is the conductivity of the material separating the surfaces and R is the thermal resistance between surfaces. The conduction shape factor represents the ratio of the effective area for conduction to the effective length for conduction, which is a measurement of how easy heat can be transferred through conduction between different surfaces. In our case, the conduction shape factor between one tube surface and all the other tube surfaces, the mandrel and the shell inner surface is investigated. Since the geometry is too complicated to calculate the effective area, the effective length or the thermal resistance, a steady state conduction model in Fluent is used. For every geometry, the flow area is changed to be solid, e.g., Cu. The temperature of one tube wall is fixed, e.g., $T_{one} = 250\ K$, and the temperature of all the other tube surfaces, the mandrel and the shell inner surface is fixed at a different value, e.g., $T_{othe} = 300\ K$. The inlet and outlet

are set as adiabatic walls. The choice of solid and boundary temperatures is arbitrary since it does not influence the result. Then the heat flux between the one specific tube wall and all other surfaces is calculated by Fluent, and the conduction shape factor between one specific tube with all other surfaces is calculated by:

$$S = \frac{q}{k(T_{oth} - T_{one})} \tag{4.3}$$

In our case, the conduction shape factor is introduced as a metric of geometry rather than a measurement of conductive heat transfer. A case with 27 tubes, 3 tubes in one bundle is shown in Figure 4.10. In the following part of this thesis, the conduction shape factor of one tube refers to the conduction shape factor between this tube wall and all the other surfaces. In Figure 4.10, the conduction shape factors of the three tubes are calculated separately, and the temperature fields at steady state are displayed. All the three tubes have the same value S=0.28 m, thus it can be concluded that all the 27 tubes have the same conduction shape factor value due to the circular symmetry. The consistency of the conduction shape factor indicates the uniform distribution of the tubes, which is significantly important for the performance of a heat exchanger.

The consistency of the conduction shape factor for different tubes in one geometry is general, while differences between different geometries exist and are obvious, which is shown in Figure 4.11. Generally, the geometry with a more compact configuration (more tubes, shorter pitch length) has a larger conduction shape factor. The conduction shape factor has a strong correlation with both the Nu value and friction factor. The Nu number and friction factor of different geometries versus Re are shown in Figure 4.12 and 4.13. The geometries with a conduction shape factor smaller than 0.3 m have an obviously larger Nu value than other geometries. This is consistent with the conclusion of the previous section. Since the free space behind tubes is larger

in geometries with a smaller shape factor, the vortex structure is more developed, thus the Nu value is higher. Furthermore, in a geometry with a small shape factor, there is some jet flow in the large open space where there is no tube, as shown in Figure 4.14(b), which is the case that should be avoided for heat exchanger design.

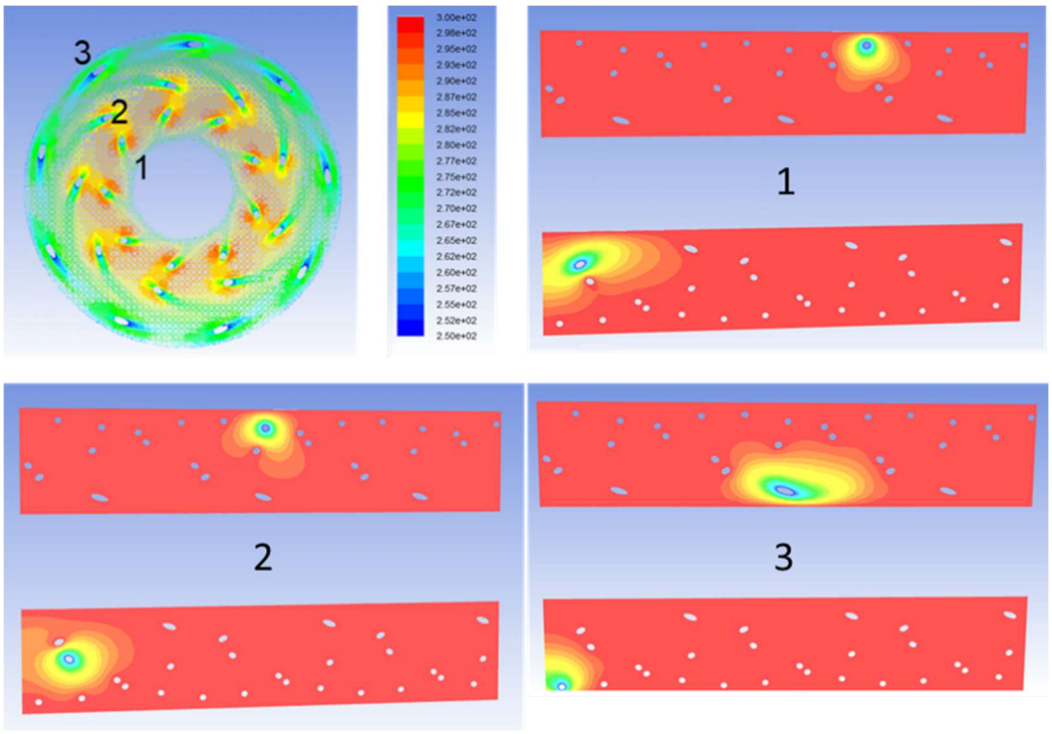

Figure 4.10. Conduction temperature field used to calculate the shape factor. Only three tubes' conduction shape factors need to be calculated due to circular symmetry. In each graph, the temperature of one tube is set to be 250 K while the temperature of other tubes is set to be 300 K. The temperature profiles of a cross section along the geometry under stead state under these three situations are demonstrated.

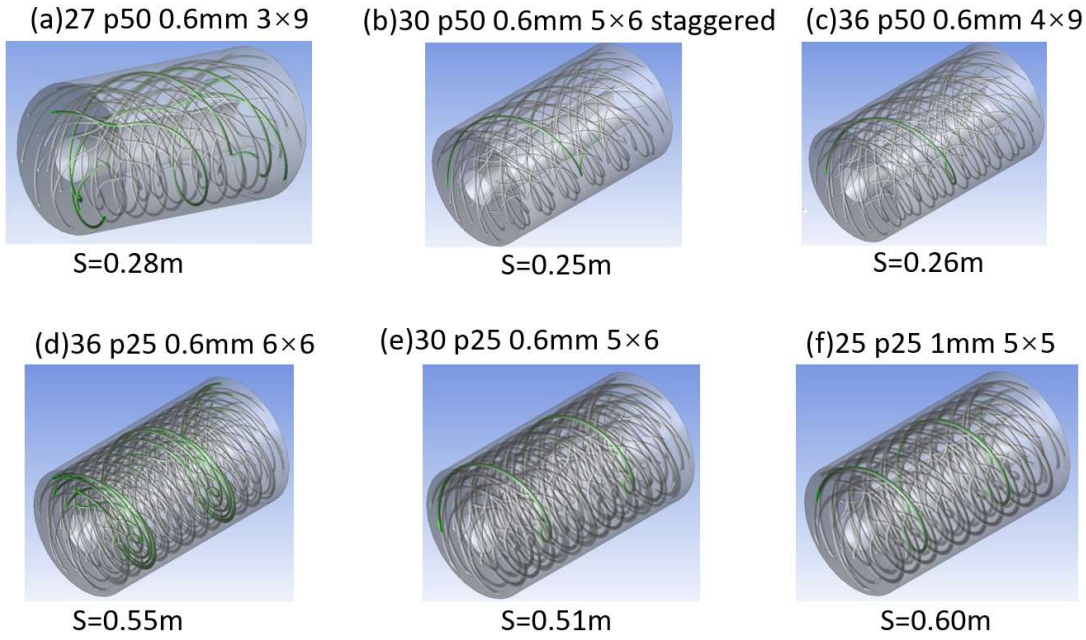

Figure 4.11. Shape factors of various geometries. "27 p50 0.6 mm 3×9" denotes that there are 27 tubes in the geometry, the pitch length is 50 mm, the outer diameter of the tube is 0.6 mm, and there are 3 tubes in one bundle, 9 bundles in total. "staggered" means that the initial phase of tubes are changed, shown in Figure 4.15.

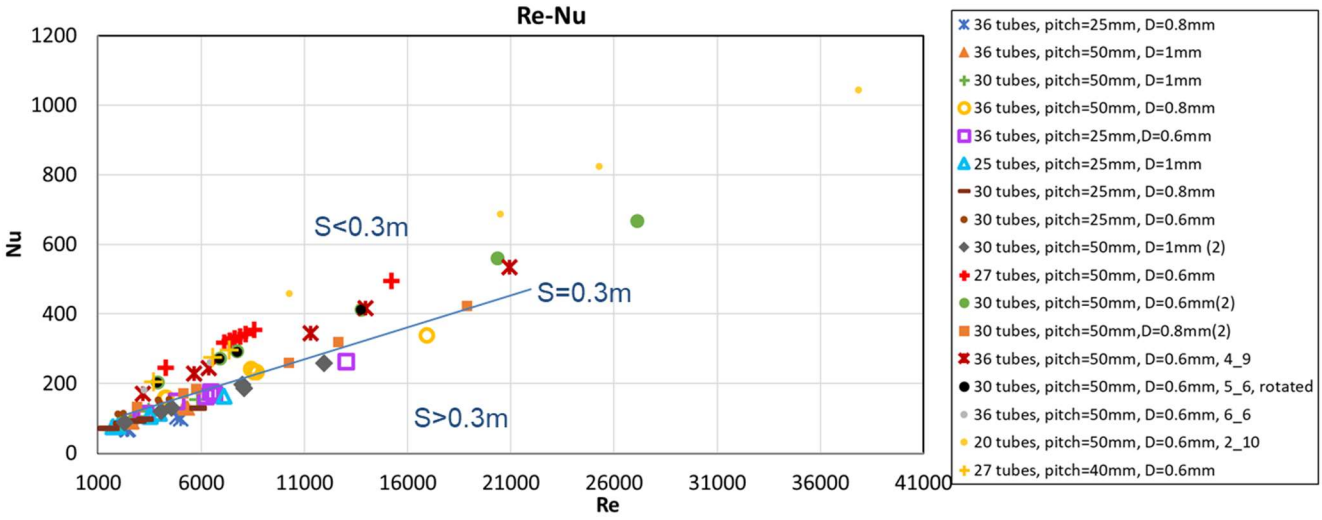

Figure 4.12. Nu-Re graph of different geometries.

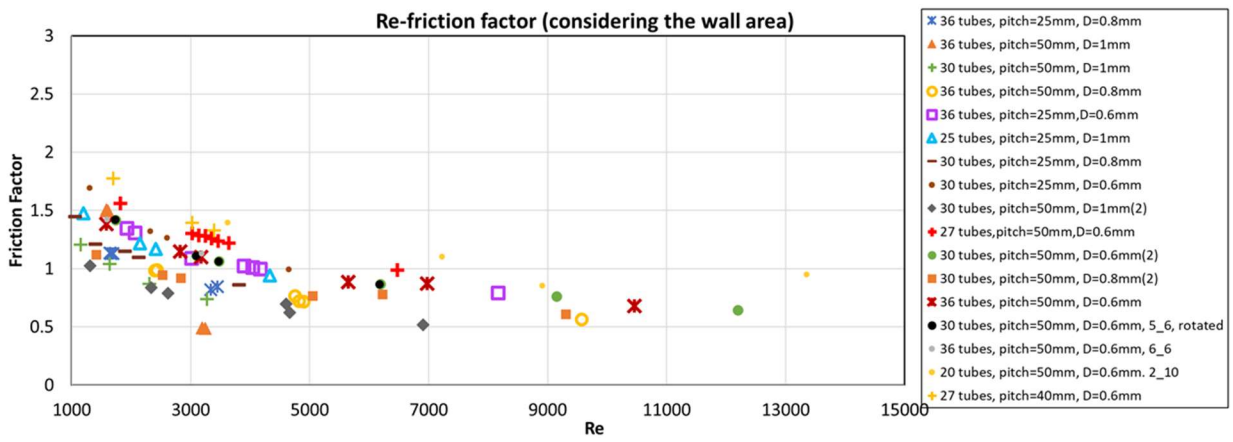

Figure 4.13. Friction factor-Re graph of different geometries.

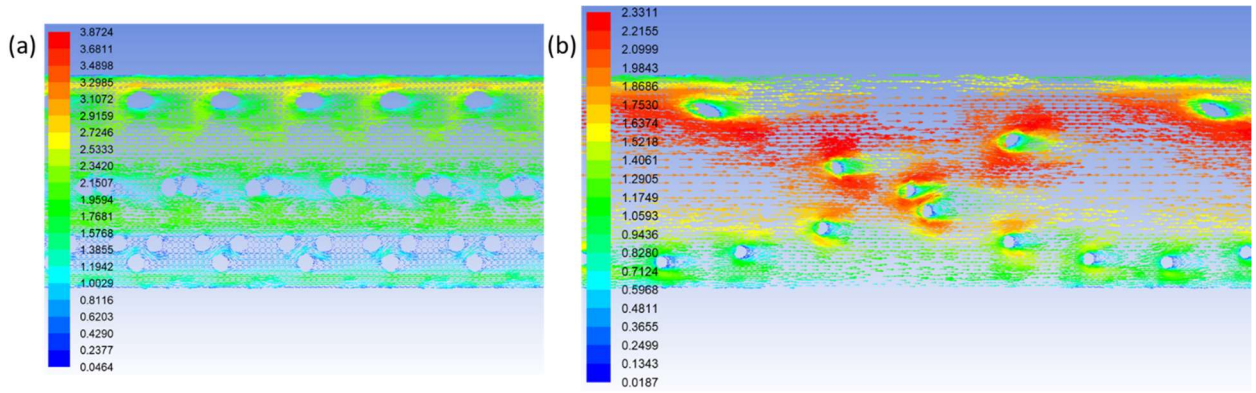

Figure 4.14. Velocity profile details for geometry (a) 36 tubes, pitch length 25 mm, D=0.8 mm and S=0.73 mm (b) 20 tubes, pitch length 50 mm, D=0.6 mm and S=0.25 m.

Different from what we expected, the distribution pattern has no effect on the shape factor and thermal performance as long as the tube number is the same, which means tubes distributed as 4×9 and 6×6 provide the same Nu values and friction factors. Staggering tube bundles by changing the initial phase of tubes (shown in Figure 4.15) at the inlet also make no difference since the tube bundles will stagger with each other anyway when they spiral inward and outward in one

cycle, which can be derived from the various section shapes shown in Figure 4.4. Therefore, the tube number should be included in the formula rather than the tube distribution.

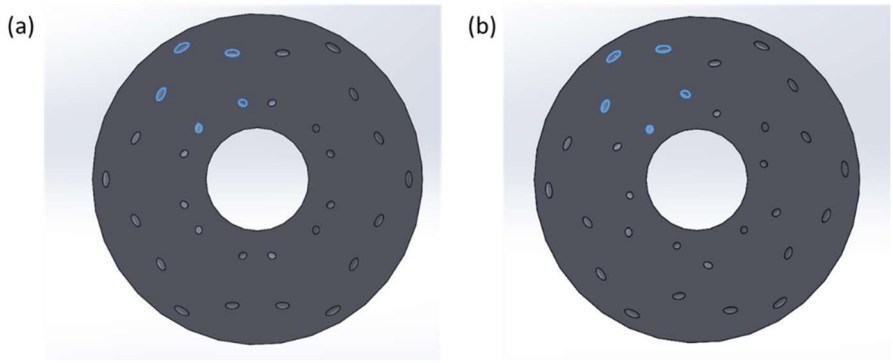

Figure 4.15. Inlet view of (a) Unstaggered tube bundles (b) Staggered tube bundles. The pentagon is one bundle of 5 tubes.

4.2.2. Nu and friction correlation

Nu and friction correlations for shell side flow are developed based on the simulation results of 17 geometries under 6 working conditions. The inlet temperature is set to be 30 K, 160 K and 300 K respectively, and inlet velocity is set to be 2 different values under each temperature. Besides the Re value, dimensionless geometric parameters are included in the Nu and friction factor formulas. For the Nu correlation, the dimensionless pitch length and tube number are included, and a good fitness is obtained. While for the friction factor correlation, the fitness is poor (R-Square value=0.6063) if only the pitch length and tube number are included. To improve the goodness of fit of the friction factor correlation, two extra dimensionless geometric parameters are included in the formula. One is the dimensionless shape factor, which is defined by the conduction shape factor divided by the pitch length. The other is the distance between two adjacent tubes in one bundle.

Since the path of every tube is generated by equations, the distance between two arbitrary tubes can be calculated. Figure 4.16 shows the distance variation along the heat exchanger between one specific tube and 8 other tubes. Tubes are numbered in Figure 4.16 (a) to distinguish them, and tubes 1-6 belong to the same bundle, while tubes 7-9 belong to the adjacent bundle. A whole period (50 mm) is divided into 1000 sections along the axis direction, and the distance between tube 1 and other 8 tubes at each axis position is calculated. From Figure 4.16 (b), it can be noted that the distance between two tubes in the same bundle stays the same along the whole period despite the complicated twisting. For two tubes in different bundles, if they locate at corresponding positions (such as tube 1 and tube 7, with the same initial phase), the distance between them also stays the same along the heat exchanger direction. While for two tubes in different bundles but not at corresponding positions (such as tube 1 and tube 8, tube 1 and tube 9), the distance between them varies periodically along the axis direction. Based on above information, the distance between two adjacent tubes in one bundle is a constant and it reflects the compactness of the geometry, so it is included in the friction factor correlation.

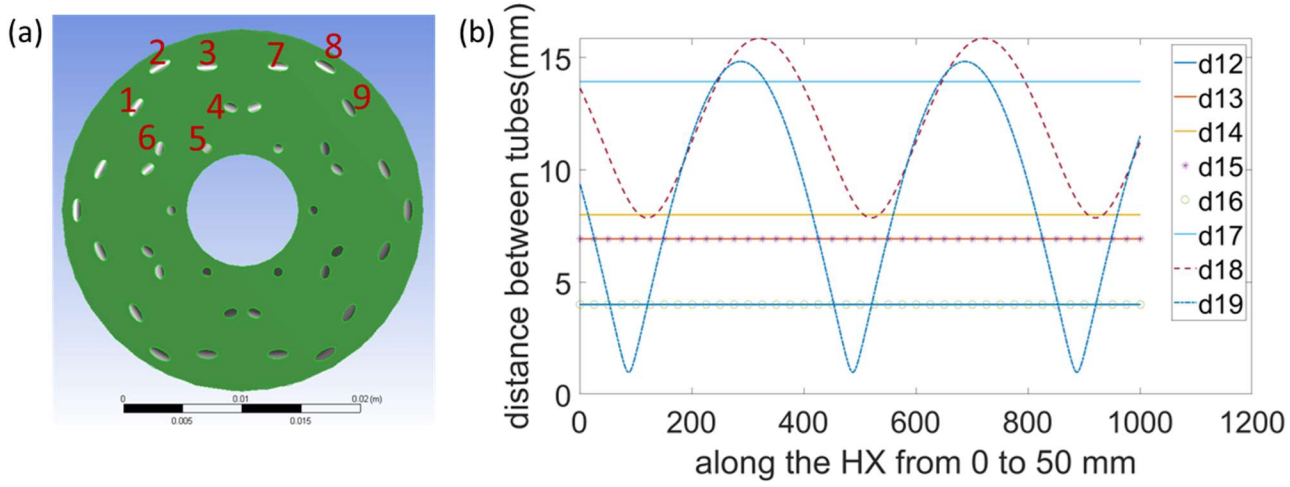

Figure 4.16. Distance variation along the heat exchanger between tubes

The correlations are shown as equation (4.4) and Equation (4.5), where N is the tube number. The Nu correlation field is shown as Figure 4.17 with R-Square as 0.99, so the goodness of fitting is quite good. The friction correlation field is shown as Figure 4.18 with R-Square as 0.9287. DD is the distance between two adjacent tubes in one bundle. The pitch length p and the distance between two adjacent tubes in one bundle DD are scaled into non-dimensional length by the tube outer diameter D_{out}. The conduction shape factor S is scaled by the pitch length. Including the dimensionless shape factor and distance between adjacent tubes into the formula significantly improve the goodness of fitting. These correlations will be used in the whole heat exchanger model to calculate the effectiveness and the pressure drop.

$$Nu = 0.5833Re^{0.60825}\left(\frac{p}{D_{out}}\right)^{0.66005}N^{-0.618} \tag{4.4}$$

$$f = 6.7026Re^{-0.39059}\left(\frac{p}{D_{out}}\right)^{0.38582}\left(\frac{DD}{D_{out}}\right)^{0.27427}\left(\frac{S}{p}\right)^{0.26130}N^{-0.39882} \tag{4.5}$$

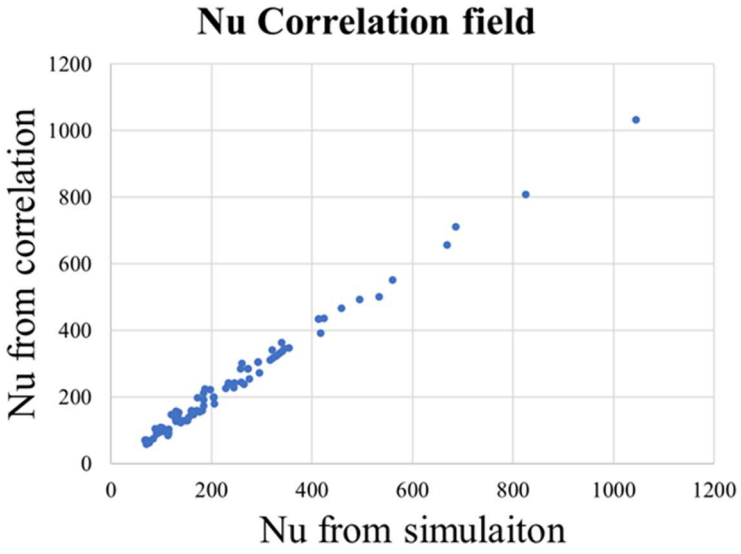

Figure 4.17. Nu correlation field.

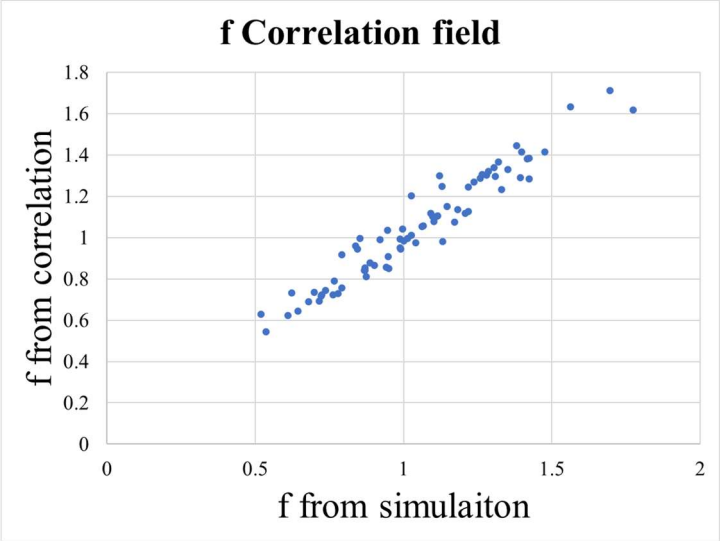

Figure 4.18. Friction factor correlation field.

4.3. Conductance

For the design of a heat exchanger, what really matters is the amount of heat transferred rather than the heat transfer coefficient. Therefore, the heat transfer area is equally important, and the conductance values of a 100 mm length of different geometries are compared. Conductance is defined by equation (4.6).

$$C = hA_{heat\ transfer} \tag{4.6}$$

Since conductance has not been non-dimensionalized, the comparison of conductance should be carried out under different temperatures, as shown in Figure 4.19 and Figure 4.20. Here the legend “30 p50 0.8” means a geometry with 30 tubes, pitch length as 50 mm and tube diameter as 0.8 mm. The mass flow rate at the inlet rather than the Re number is fixed in practical application scenarios, so the conductance variation with mass flow rate of different geometries is compared. The variation with Re number is also displayed here since the Re changes a lot along the heat

exchanger due to the variation of thermal properties from 300 K to 30 K, i.e. the density and viscosity.

Combined with the Nu-Re graph, it should be noticed that the geometry with the largest Nu value does not guarantee the largest conductance. For the same geometry under the same Re value, the conductance at 300 K is larger than that at 30 K. It is more difficult for helium to transfer heat at 30 K than at 300 K, which is the driving force for using different geometry designs at the hot end and the cold end in some heat exchangers. In this case, although both the conductance-Re relation and conductance-mass flow rate relation vary with temperature, the geometry providing the largest conductance at 300 K and the geometry providing the largest conductance at 30 K are the same one. This is very promising since it indicates the same design can be used from the hot end to the cold end of the heat exchanger.

The dash lines in Figures 4.19(b) and 4.20(b) are calculated from the Nu correlation in last section, which demonstrates a good fit with the original Fluent-simulated results.

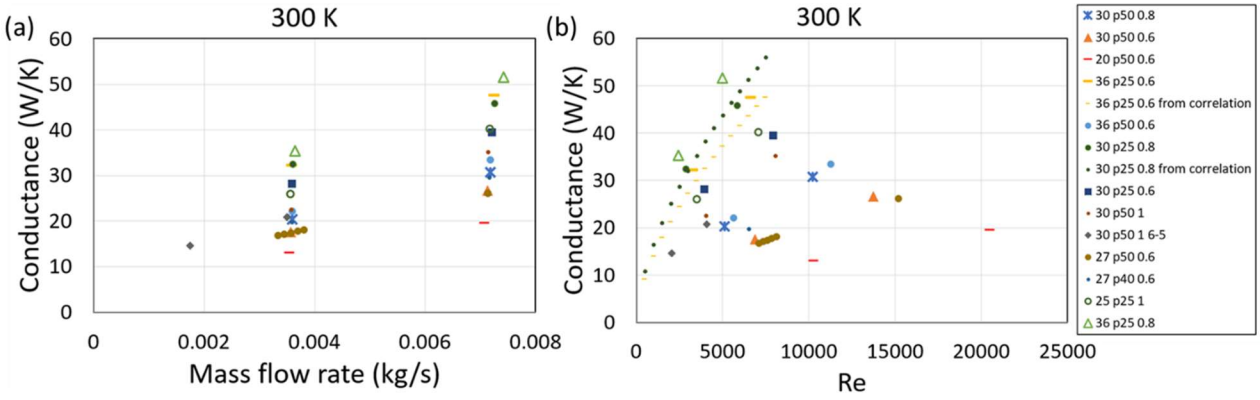

Figure 4.19. Conductance of different geometries at 300 K versus (a) mass flow rate (b) Re.

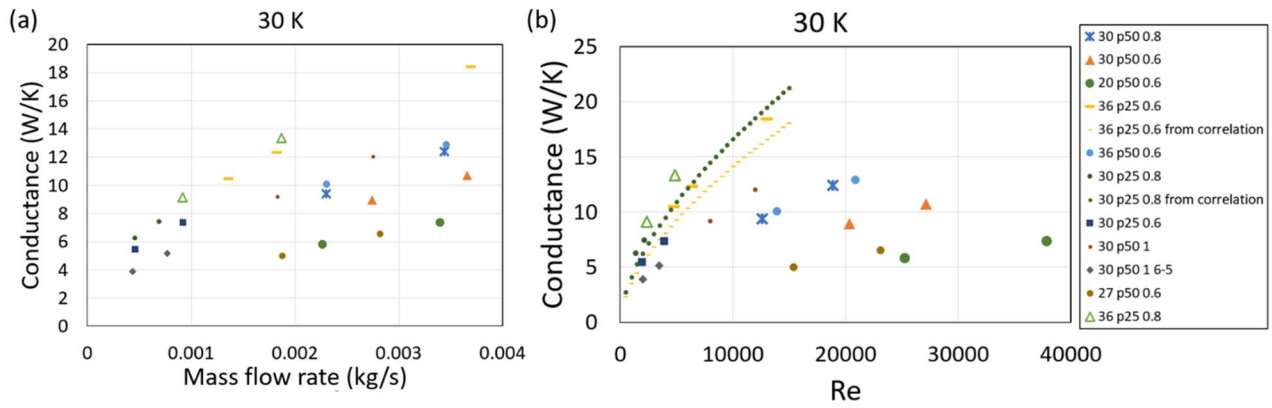

Figure 4.20. Conductance of different geometries at 30 K versus (a) mass flow rate (b) Re.

4.4. Vortex visualization and conductance

An intermittent structure in fluid flow is referred to as the large-scale coexistence of an irrotational and rotational fluid near the edge of a turbulent region. Studies have shown that the overall energy production and dissipation is larger in this region due to the steep velocity gradient. Also, the resulting stronger vorticity creates stronger pressure fluctuations, which in turn leads to a faster redistribution of energy to the transverse velocity components [36]. To optimize the heat exchanger design, the vortical structure is visualized using the Q-criterion [37]. In Einstein notation, the value Q comes from the definition of the velocity gradient tensor du_i/dx_j, as shown in equation (4.7):

$$\frac{du_i}{dx_j} = \frac{1}{2}\left(\frac{du_i}{dx_j} + \frac{du_j}{dx_i}\right) + \frac{1}{2}\left(\frac{du_i}{dx_j} - \frac{du_j}{dx_i}\right) \tag{4.7}$$

The first term on the right-hand side is known as the strain rate tensor SR (usually S is used but in this paper S is already used as the shape factor), and the second term on the right hand side is known as the vorticity tensor Ω:

$$SR = \frac{1}{2}\left(\frac{du_i}{dx_j} + \frac{du_j}{dx_i}\right) \tag{4.8}$$

$$\Omega = \frac{1}{2}\left(\frac{du_i}{dx_j} - \frac{du_j}{dx_i}\right) \tag{4.9}$$

Then Q is defined using the magnitude of SR and Ω:

$$\mathrm{Q} = \frac{1}{2}(\|\Omega\|^2 - \|\mathrm{SR}\|^2) \tag{4.10}$$

From the definition, the positive values of Q are indicative of areas where the vorticity dominates while negative values of Q are indicative of areas where the strain rate dominates. A vorticity magnitude contour on Q iso-surfaces is used to visualize the vortical structure. Due to the wide range of vorticity magnitudes, iso-surfaces of different Q values will result in far fewer and less structures, as illustrated in Figure 4.21. Since iso-surface Q=1E3 shows a very limited number of structures while iso-surface Q=1E5 shows an excessive number of structures, iso-surface Q=1E4 is selected and further analyzed.

The average vorticity magnitude on iso-surface Q=1E4 has a strong relation with the corresponding conductance, as shown in Figure 4.22. The relationship is not linear, and the slope decreases from the 30 K data set to the 300 K data set, which means that the same change of vorticity causes a larger change of conductance at 30 K than at 300 K. Even at the same vorticity magnitude, there exist differences among the conductance of different geometries. And the difference of conductance among various geometries at the same vorticity magnitude is smaller at 30 K, and then gradually increases as temperature increases. These two phenomena imply that at the lower temperature, turbulence and fluid mixing is a more dominant factor of the overall heat transfer behavior. Another takeaway is that there are other parameters than vorticity magnitude influencing the overall conductance.

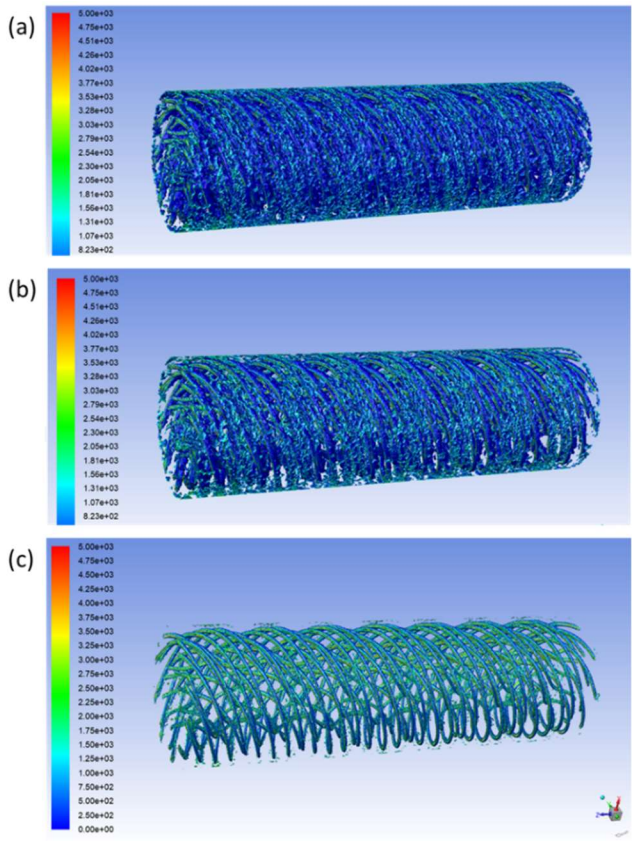

Figure 4.21. Contour of vorticity magnitude on iso-surface (a) Q=1E3 (b) Q=1E4 (c) Q=1E5.

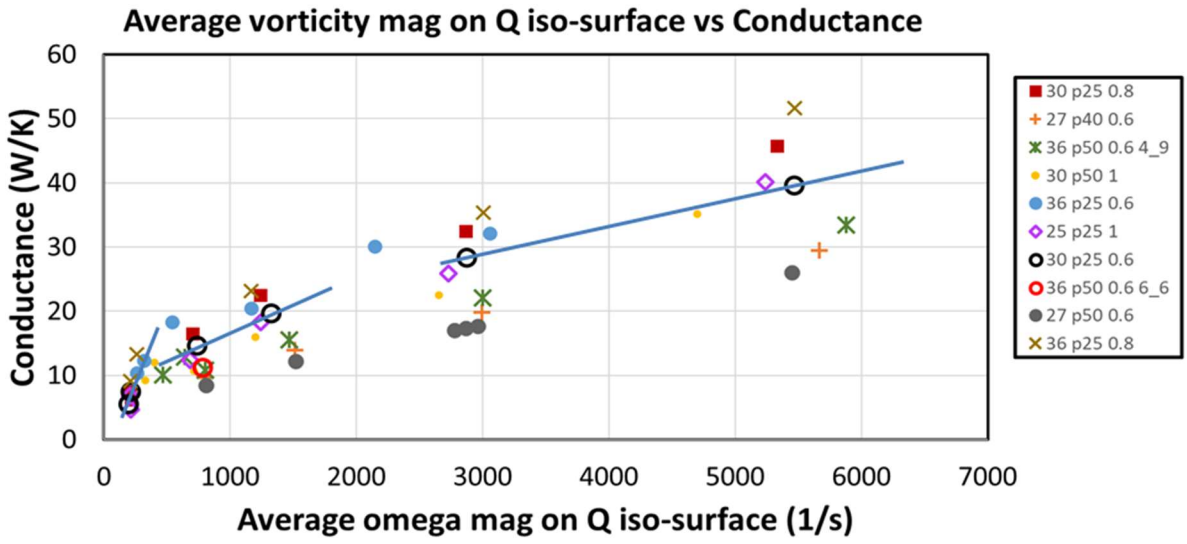

Figure 4.22. Relationship between the average vorticity magnitude on Q iso-surface and conductance.

Neither vorticity nor conductance is a dimensionless parameter, so two methods are tried to develop a correlation between them. One is including other thermal and fluid properties into the relation. It is found out that the viscosity *mu* multiplied by the specific heat capacity *cp* multiplied by the fluid velocity *u* and divided by the conductance *C* leads to a physical quantity with the same unit (1/s) as the vorticity magnitude. The relation between this physical quantity and the vorticity magnitude is shown in Figure 4.23.

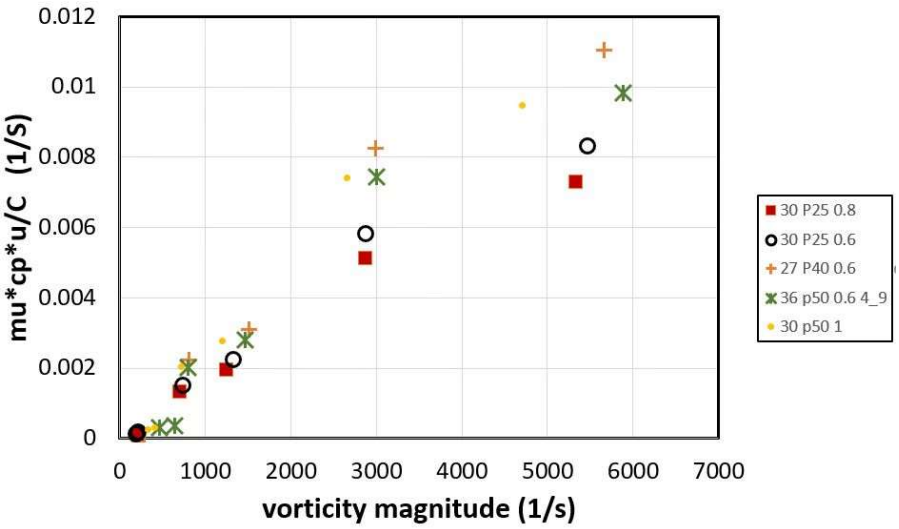

Figure 4.23. Relation between a new physical quantity and vorticity magnitude. This new physical quantity combines viscosity, specific heat capacity, velocity and conductance and has the same unit as the vorticity magnitude.

Another method is non-dimensionalizing both conductance and vorticity magnitude. The conductance is scaled into a non-dimensional parameter by the product of conductivity and hydraulic diameter. The vorticity magnitude ω is scaled by multiplying by the hydraulic diameter then dividing by the velocity. It should be noted that the geometric parameter, hydraulic diameter, is also included in this method. The relationship between these two new dimensionless parameters is shown in Figure 4.24.

Unfortunately, no clear relations can be developed using these two techniques. From both plots, the difference among data caused by temperature is obvious. A coefficient measuring how dominant the mixing is on the heat transfer behavior at different temperatures should be proposed. Other thermal or geometric parameters may need to be included into the relation or be used to scale the conductance and vorticity magnitude, and this will be subject of future work.

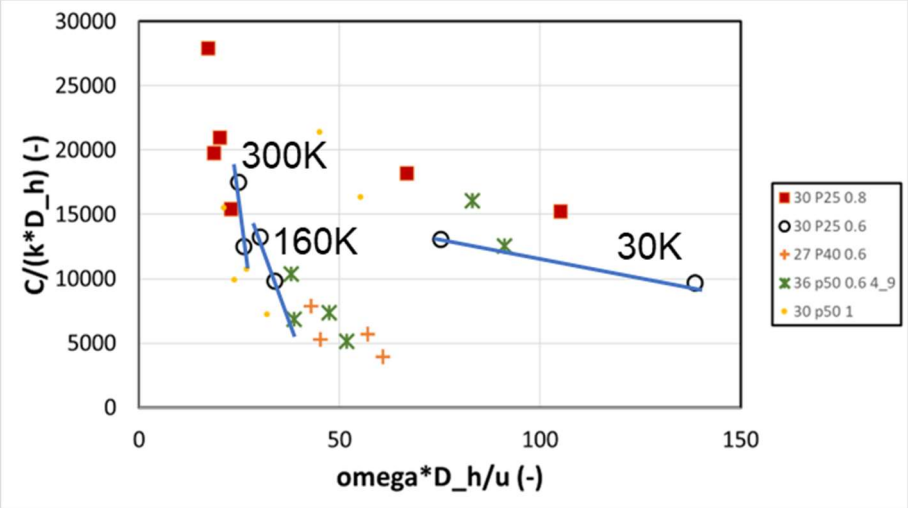

Figure 4.24. Relationship between dimensionless conductance and dimensionless vorticity magnitude.

5. Tube side model

5.1. Tube side geometry and parameter of concern

In a twisted helical tube bundle geometry, all the tubes have the same length, average coil diameter and heat transfer area. The only difference among the tubes in a bundle is the initial phase. The phase difference between two adjacent tubes is $2\pi/n$, assuming n is the number of tubes in one bundle. A 1 mm axial section of a geometry with 8 tubes in one bundle is shown in Figure 5.1. With the primary flow direction for the shell side in the axial direction, one may observe that tubes near the mandrel extend in a direction more similar to counter flow configuration, while tubes near the outer shell extend in a direction more similar to cross flow configuration. Due to the angle difference, the heat transfer area of different tubes is different in this short section. Although all tubes will change their angles and position and go through the same heat exchanger area in one period, this initial phase difference may cause local non-uniform temperature distributions.

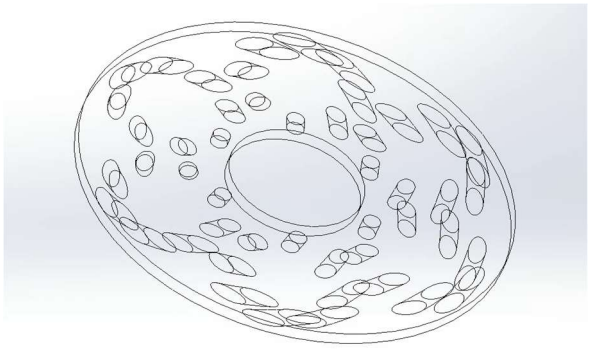

Figure 5.1. Initial phase difference among tubes in one bundle. In this short section, tubes near the mandrel are closer to counter flow configuration, while tubes near the outer shell are closer to cross flow.

Besides the phase difference among tubes in the same bundle, the influence of other geometry parameters are studied, including the tube diameter, pitch length and coil diameter. The

tube side simulation is carried out on the following 9 geometries in Figure 5.2, where a and b are the coefficients from the formula generating the tubes, and the value (a+b) is the bundle radius.

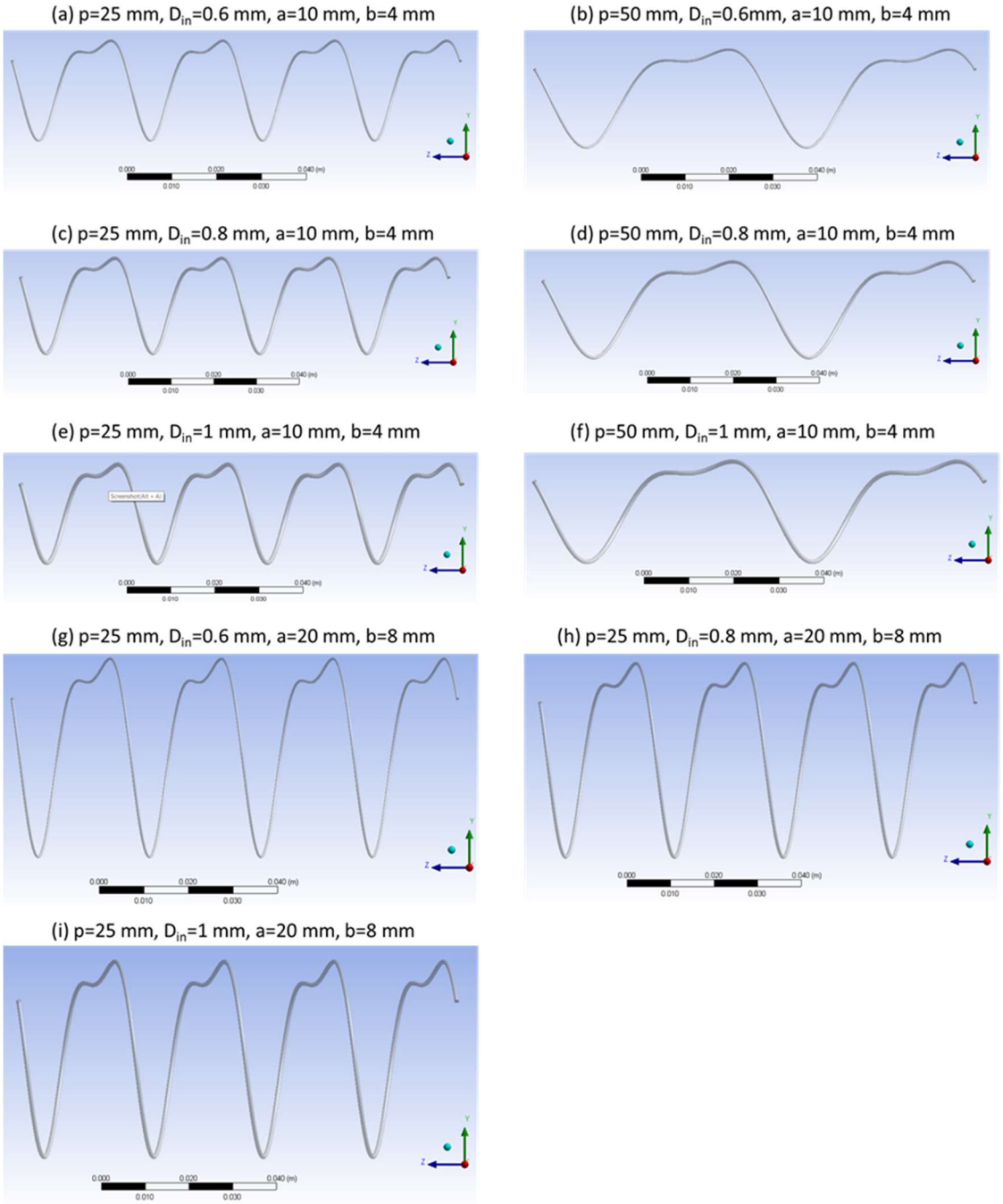

Figure 5.2. Tubes with different pitch length (p), inner diameter (D_{in}) and bundle diameter (a+b), a and b are coefficients in the equations generating the tube curves.

5.2. Meshing setting

Tube side flow is a type of wall-bounded flow, for which an accurate near wall region prediction is significantly important. The solution variables of Navier-Stokes equations have a large gradient in the near wall region due to the viscosity effect. To deal with the near wall region, two dimensionless parameters are utilized, i.e., the dimensionless wall distance y^+ and the dimensionless velocity u^+. The dimensionless wall distance y^+ is defined by:

$$y^+ = \frac{yu_\tau}{\nu} \tag{5.1}$$

Where y is the distance from the wall, ν is the kinematic viscosity and u_τ is the friction velocity defined by:

$$u_\tau = \sqrt{\frac{\tau_\omega}{\rho}} \tag{5.2}$$

Where τ_ω is the wall shear stress:

$$\tau_\omega = \rho\nu \left(\frac{d\langle U\rangle}{dy}\right)_{y=0} \tag{5.3}$$

The dimensionless wall distance y+ can be interpreted as a local Reynolds number. It has a similar formula as the Re number and its value helps determine which kind of stress is dominant, the viscous stress or Reynolds stress. Figure 5.3 shows how the fractional contributions of the two kinds of stresses vary with y+. In the region where y+ is less than 50, the wall shear stress accounts for a non-negligible proportion. In the region where y+ is less than 5, the wall shear stress accounts for more than 80% of the total stress, thus this region is the viscosity dominated region, and is known as the viscous sublayer.

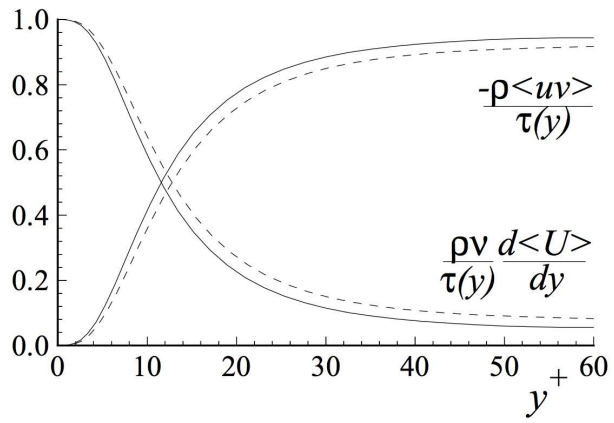

Figure 5.3. Profiles of fractional contributions of the viscous and Renolds stresses to the total stress. DNS data of kim et al. (1987): dashed lines, Re=5600; solid lines, Re=13750 [37].

The law of the wall shows the dimensionless velocity distribution over the dimensionless wall distance in the near wall region. The dimensionless velocity is defined by

$$u^+ = \frac{u}{u^\tau} \tag{5.4}$$

Figure 5.4 shows the law of the wall. In the viscous sublayer (y+<5), the dimensionless velocity has a linear relation with the dimensionless wall distance. In the log-law region (y+>30), as the name suggests, the two dimensionless parameters follow a log formula. This distribution behavior is similar for all turbulent flows. The k-ω SST model has the robustness to resolve the viscous sublayer [35]. If the first cell height is in the viscous layer, it will resolve the boundary layer by evaluating the velocity at each cell. If the first cell is in the log layer, the software will make an empirical assumption about the viscous sublayer, referred to as using a wall function. To make sure the viscous sublayer is resolved, the value of y+ should be about 1.

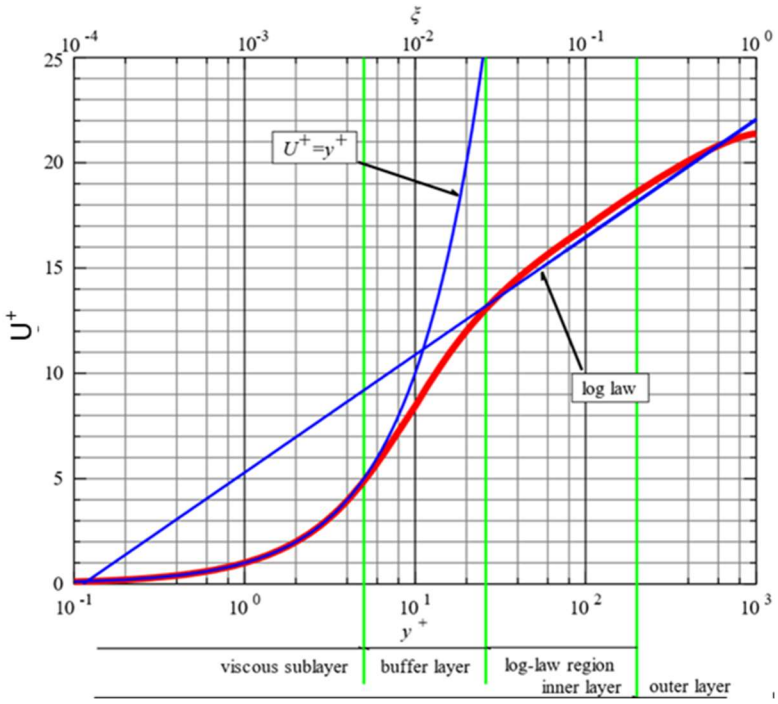

Figure 5.4. The Law of the wall [38].

A single tube with diameter as 1 mm, pitch length as 25 mm and length as 100 mm (shown in Figure 5.5) has been simulated to analyze mesh independence. Cell size and inflation layer are changed to generate meshes with different cell number, and the settings are listed in Table 5.1. Figure 5.6 and Figure 5.7 show the variation of the Nu and pressure drop values versus cell number. Both Nu and pressure drop values become steady when the cell number is more than 4.33 million. The average y+ values of each mesh are also shown in Table 5.1. The average y+ value reaches about 1 when the cell number is 4.33 million. The y+ value is strongly influenced by the number of inflation layers. When the inflation layer is not enough (for example, when the inflation layer is 8 for this geometry), even with a smaller cell size and larger cell number, the average y+ value is still larger than 1.

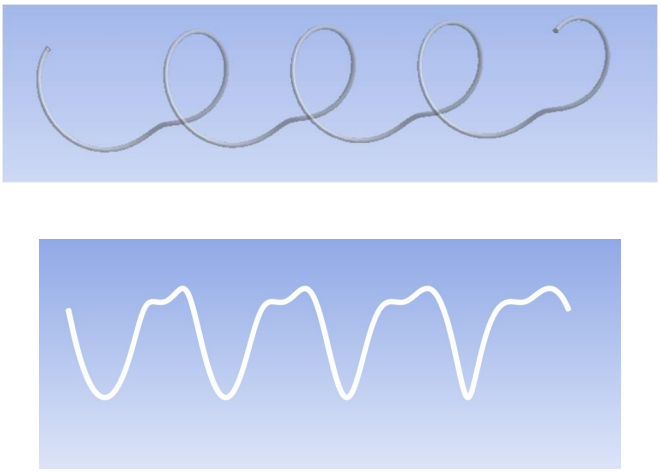

Figure 5.5. A single tube with diameter as 1 mm, pitch length as 25 mm and length as 100 mm and its 2D projection.

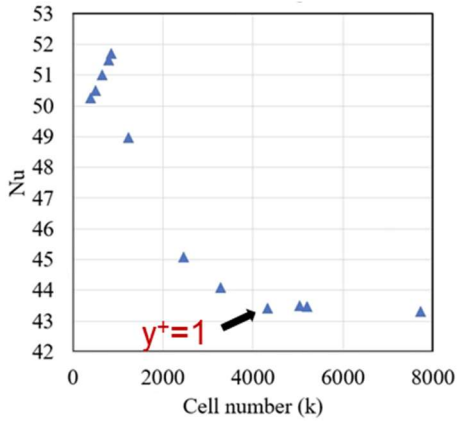

Figure 5.6. Nu value variation versus cell number.

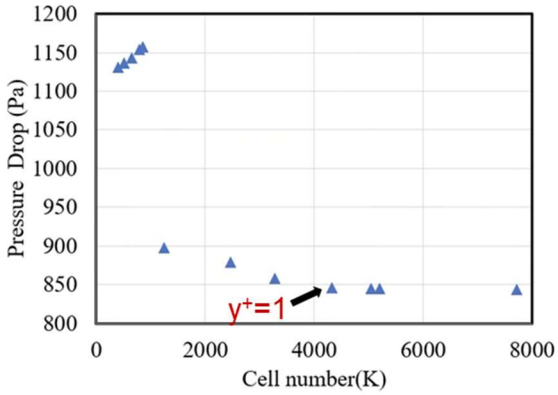

Figure 5.7. Pressure drop variation versus cell number.

Table 5.1. Relations among meshing setting, cell number and average y+ value.

Cell number	Ave. y_plus	Cell size (m)	Inflation layer	Growth rate
400k	33.9	9e-5	No inflation	
504k	32.0	8e-5		
653k	30.4	7e-5		
795k	28.2	6e-5		
860k	27.3	5e-5		
2459184	2.4076	8e-5	8	1.2
3278387	2.0651	7e-5	8	1.2
4328744	0.9907	7e-5	12	1.2
5042623	0.4787	7e-5	16	1.2
5198184	1.7784	6e-5	8	1.2
7721958	1.4689	5e-5	8	1.2

Based on above analysis, a cell size of 7e-5 m and inflation layer 12 are used in the following tube side simulation cases. The generated mesh is demonstrated in Figure 5.8. The sweep method is used so that the face mesh is the same from the inlet surface to the outlet surface.

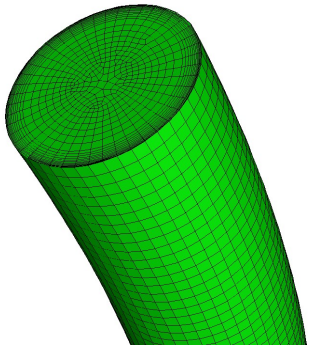

Figure 5.8. Example mesh with enough inflation layers.

5.3. Fluent setting and governing equations

The turbulence model for the tube side flow simulation is the same as the one applied for the shell side flow simulation, the SST k-ω model, since it can resolve the viscous sublayer. The velocity is specified at the inlet, and the pressure is specified at the outlet. The pressure at the inlet is calculated by Fluent, and then the pressure drop can be obtained. Three boundary conditions along the tube wall are explored and compared, i.e., constant heat flux boundary condition, constant temperature boundary condition and convection boundary condition. It is determined that the constant heat flux boundary condition is closer to the realistic situation, which will be discussed in detail later. The constant heat flux at the wall is set to be -20 W/m^2.

To reduce the entrance effect, the Nu value and friction factor are calculated from the second half of the simulation domain (in the axial direction), using following equations:

$$h_{tube} = \frac{\dot{q}}{\overline{T_{bulk}} - \overline{T_{wall}}} \tag{5.5}$$

$$Nu_{tube} = \frac{h_{tube} D_{h,tube}}{k} \tag{5.6}$$

$$\Delta P_{tube} = P_{in,tube} - P_{out,tube} \tag{5.7}$$

$$f_{tube} = \frac{2\Delta P_{tube} D_{h,tube}}{\rho L {U_{in}}^2} \tag{5.8}$$

Where the hydraulic diameter is the inner diameter of the tube, the average bulk temperature and average wall temperature are calculated from the second half of the domain. The velocity and inlet pressure in the Re and friction factor formula are the average values on the middle cross section of the domain. The length L is the developing length of the tube calculated by integral.

5.4. Model verification

Since there is no experimental data for the twisted tube proposed in this study, the comparison for the coil side flow was carried out by simulating the helical coiled microtube tested in literature [23]. The geometry and mesh are shown in Figure 5.9. The tube diameter is 0.787 mm, pitch value is 7.5 mm, and coil diameter is 9.6 mm. The mesh is generated using a sweep method with the sweep size as 0.1 mm. The working fluid is water with an inlet velocity of 0.78-4 m/s and an Inlet temperature of 295 K. Both constant wall temperature and constant heat flux boundary conditions were explored and compared. It turned out that constant heat flux boundary condition has a better agreement with the experimental data. The comparison between different models is shown in Figure 5.10. Here the 4 revolutions model means the tube rotates 4 cycles and the 10 revolutions model means the tube rotates 10 cycles. For each model, Nu values calculated from the 4 revolutions model are larger than those from the 10 revolutions model due to a strong entrance effect. When L/D is long enough (10 revolution model), Laminar, LES and $k-\omega$ models fit best with experiment results.

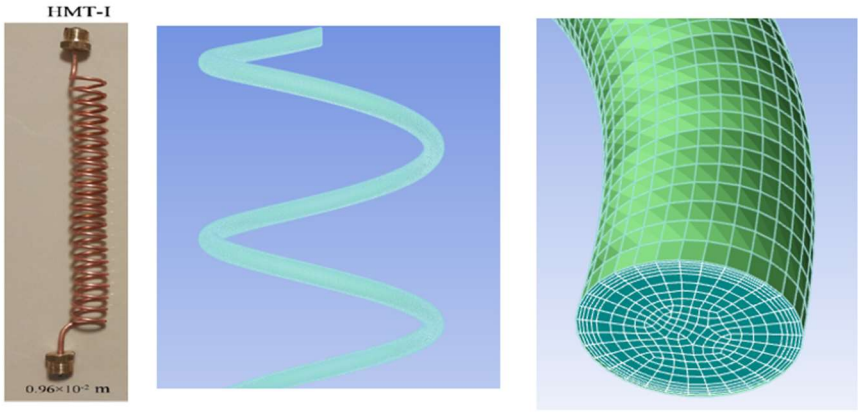

Figure 5.9. Coil side computation domain and mesh for model comparison.

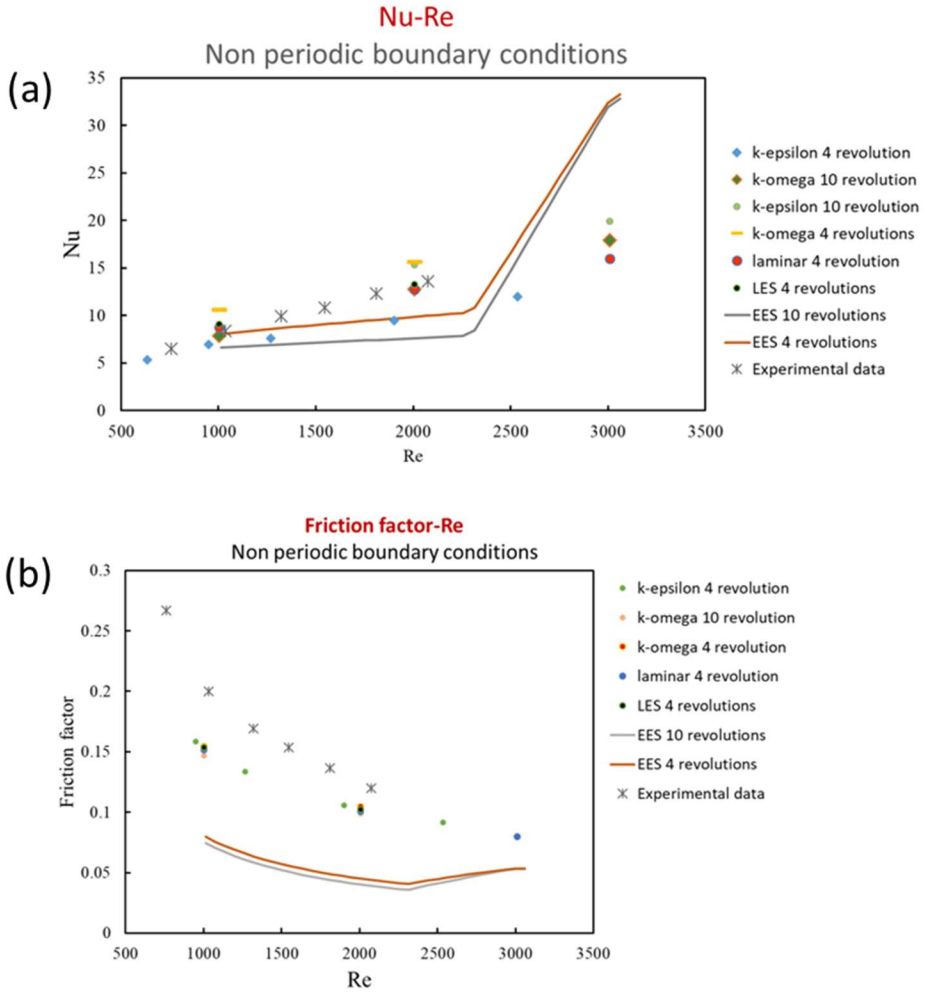

Figure 5.10. Comparison among various models for coil side flow (a) Nu-Re (b) Friction factor-Re.

According to the comparison, the $k-\omega$ model is more suitable for simulating the flow behavior in a helical coiled tube than the $k-\varepsilon$ model. Besides, the $k-\omega$ model is less time consuming than LES model, so it is reasonable to choose the $k-\omega$ model based on the comparison with experimental data and its capability to solve the viscous sublayer.

6. Tube side simulation results analysis

In this chapter, the tube side flow performance is studied both qualitatively and quantitatively. The flow structure is shown by the profiles of different solution variables, i.e., temperature, velocity, pressure, and turbulence kinetic energy. The variation of those profiles versus the Re value and among different geometries are analyzed. To quantitatively determine the influence of various geometry parameters, the Nu and friction factor correlations for tube side flow are developed.

6.1. Profiles of solution variables

The centrifugal force induced by the helical structure acts on the tube side flow, generating secondary flow, promoting fluid mixing, and enhancing the heat transfer efficiency. The flow structure varies with the Re value and geometry, and studying the relationship between them will help to optimize the design.

6.1.1. Profiles of solution variables variation versus Re

The distribution profiles of temperature, velocity, and pressure of flow through helical tubes show an obvious difference with those of flow through straight tubes, so that the strong influence of the centrifugal force can be observed. For each tube, the fluent simulation is carried out under 6 working conditions, where the inlet temperature is set to be 30 K, 160 K and 300 K respectively, and the velocity is set to 2 different values for each of the inlet temperatures. Therefore, the flow with 6 different Re values are simulated. A cross section in the middle of the computational domain is chosen to help analyze the flow structure, as a representative of fully

developed flow since it is far away from both the inlet and outlet. The cross section is perpendicular to the wall and flow direction, as shown in Figure 6.1.

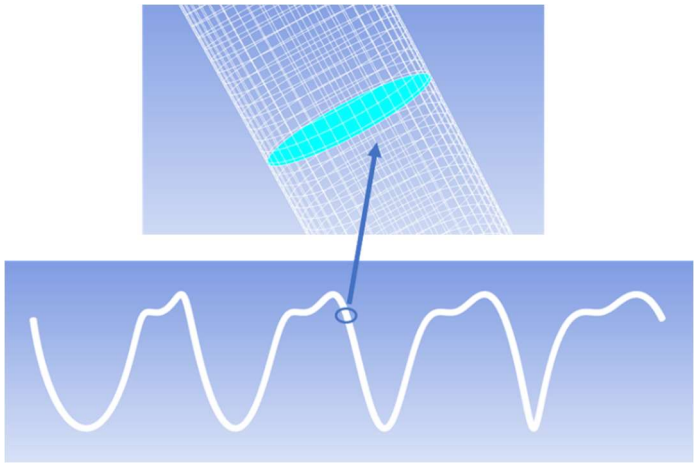

Figure 6.1. The position of the following cross section, and the shape of the cross section is a circle.

The temperature and velocity distribution profiles on this cross section under 6 working conditions are displayed in Figure 6.2 and Figure 6.3 separately. The geometry shown in this section has a pitch length of 25 mm and a diameter of 0.6 mm. The high temperature and high velocity occur at the area far away from the spiral axis, and the radial offset of the peak temperature and peak velocity is the largest at the smallest Re value condition. The radial offset gradually decreases as the Re value increases, which means that the turbulent mixing of fluid can weaken the influence of the centrifugal force to some extent.

The thickness of both the thermal boundary layer and viscous boundary layer decreases as the Re value increases, observed from the near wall region of Figure 6.2 and Figure 6.3. Both boundary layers are thicker at the wall area near the spiral axis, which means the temperature and velocity gradients are smaller there. Therefore, for flow inside a helically coiled tube, most heat transfer occurs at the area far away from the spiral axis.

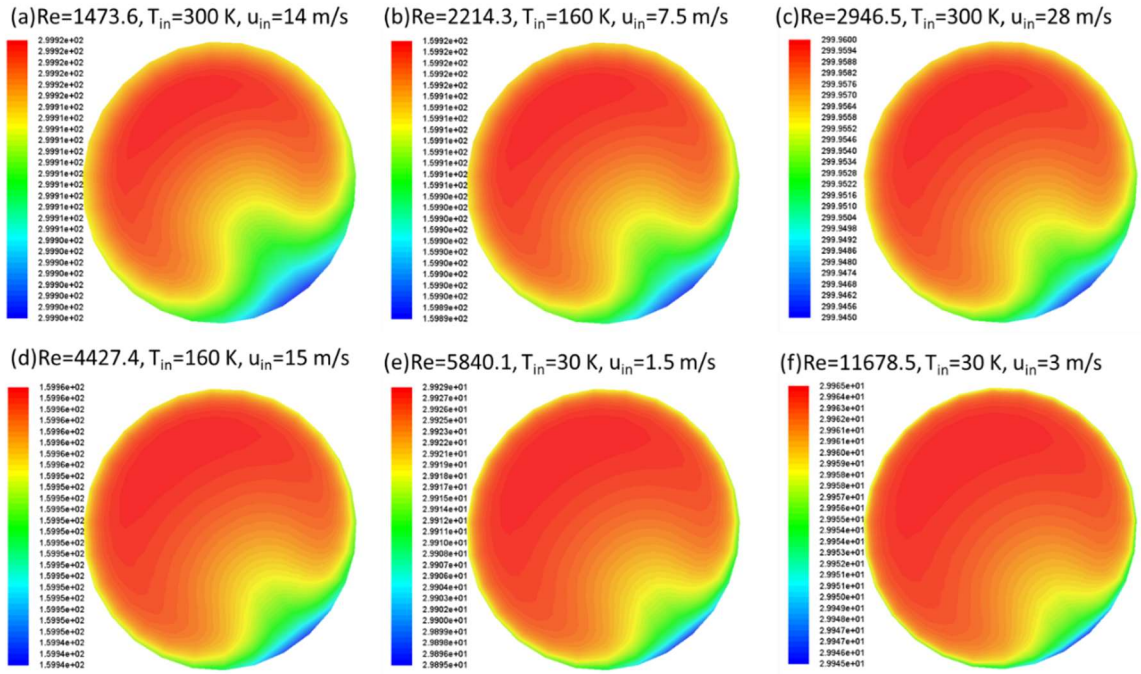

Figure 6.2. The temperature (K) distribution on the middle cross section under 6 working conditions, p=25 mm, D_{in}=0.6 mm.

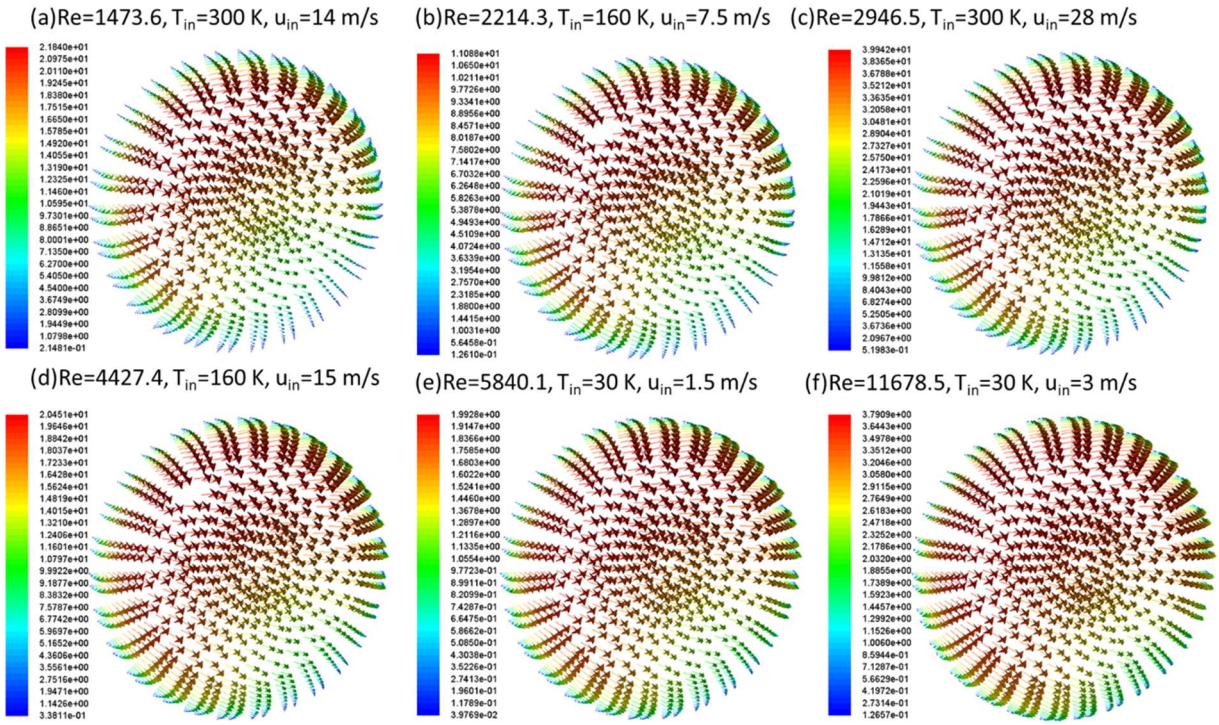

Figure 6.3. The velocity (m/s) distribution on the middle cross section under 6 working conditions, p=25 mm, D_{in}=0.6 mm.

It should be noted that under the context of a such large temperature range (300 K to 30 K), a large Re value does not mean a large heat transfer coefficient, due to the extremely low viscosity and low conductivity of helium at low temperatures. In fact, in Figure 6.2 and Figure 6.3, the heat transfer coefficient under working condition (f), which is 2768.166 W/m^2-K, is similar or even smaller than the one under working condition (a), which is 2928.58 W/m^2-K, while the Re value under the former case is much larger than that under the latter case. It is much harder for helium to transfer heat at 30 K than at 300 K, and this may be the key to improve the helium heat exchanger performance in future designs.

The turbulent kinetic energy also does not increase linearly with the Re value. The turbulent kinetic energy is defined using the following equation:

$$TKE = \frac{1}{2}\left(u'^2 + v'^2 + w'^2\right) \tag{6.1}$$

Where u', v' and w' are the velocity fluctuations in three directions. The turbulent kinetic energy is an important indicator of the mixing ability of turbulence, reflecting the growth and weakness tendency of a vortex. The turbulent kinetic energy distribution profiles on the middle cross section under the 6 working conditions are shown in Figure 6.4. In the situations of low Re values, there exist two obvious high turbulent kinetic energy areas, one is the wall area far away from the spiral axis, and another is near the velocity peak. As the Re value increases, the one near the velocity peak gradually fades and disappears. The distribution of turbulent kinetic energy tends to be more uniform in the case of high Re values.

The value of the turbulent kinetic energy provides more information than the distribution pattern. The order of the working conditions from small turbulent kinetic energy magnitude to large is (e) < (f) < (b) < (a) < (d) < (c), and the order of the working conditions from small heat

transfer coefficient to large is (e) < (b) < (f) < (a) < (d) < (c). The orders are not exactly the same, but can still show some trends. Basically, high turbulent kinetic energy means high heat transfer coefficient. It can be found out that the turbulent kinetic energy values at 300 K, shown in Figure 6.4 (a) (c), are orders of magnitude larger than those values at 30 K, shown in Figure 6.4 (e) (f), even though the Re value in the former situation is much smaller. For helium, it is much easier to generate flow fluctuations under high temperatures when the Re value is fixed.

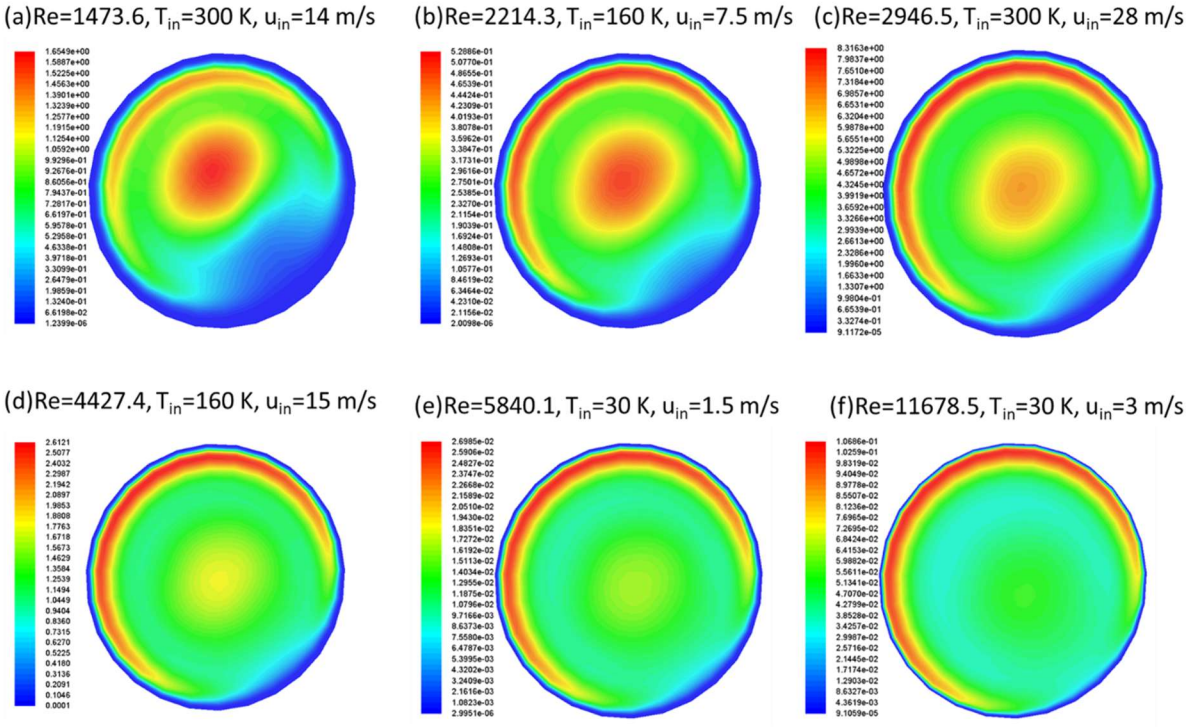

Figure 6.4. The turbulent kinetic energy (m^2/s^2) distribution on the middle cross section under 6 working conditions, p=25 mm, D_{in}=0.6 mm.

As shown in Figure 6.5, the pressure distribution profiles appear very similar under different Re values. The shape of the pressure distribution, with almost straight contour lines, is different than the temperature, velocity, and kinetic energy distributions shown above. The pressure difference on the cross section does not change linearly with the Re value. And it should

be noted that there is hardly any pressure difference under the working condition in Figure 6.5 (e), which also provides the least velocity fluctuation and smallest heat transfer coefficient.

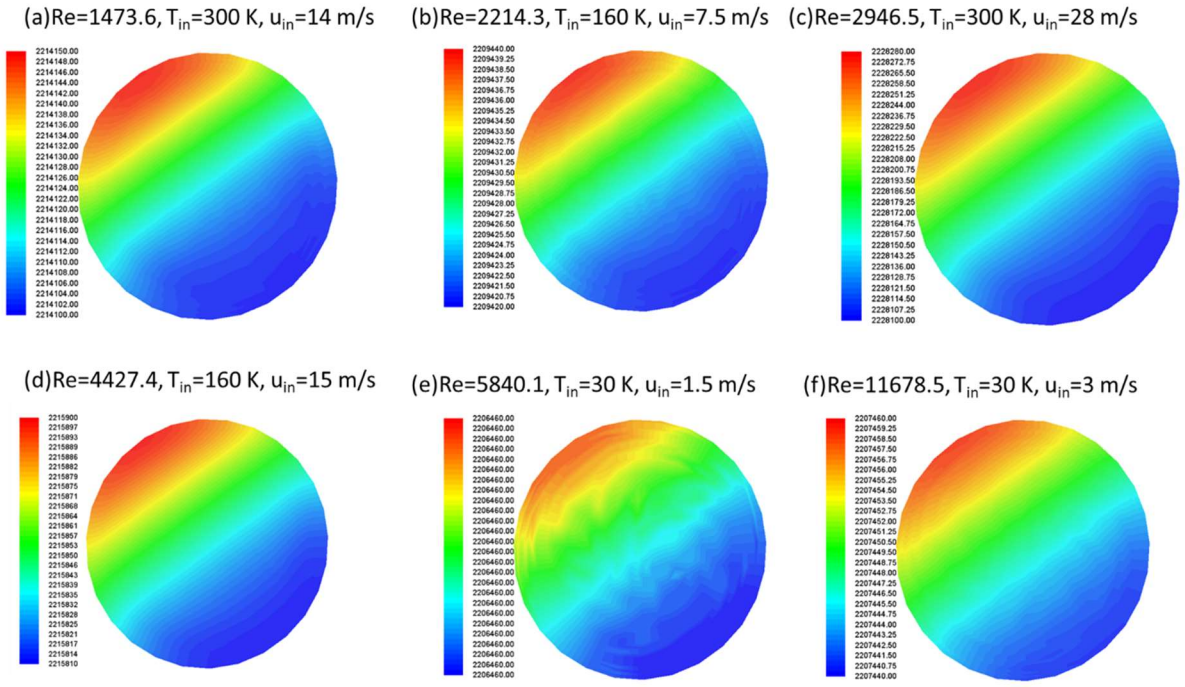

Figure 6.5. The pressure (Pa) distribution on the middle cross section under 6 working conditions, p=25 mm, D_{in}=0.6 mm.

6.1.2. Influence of geometries

The influence of geometric parameters on the flow pattern is also explored. There are 6 geometries shown in Figure 6.6, with the combination of 3 different inner diameters and 2 different pitch lengths. Based on the comparison of turbulent kinetic energy distribution among these geometries under the same working conditions, it can be observed that the change caused by increasing the diameter is quite similar to the case of increasing the Re value in Figure 6.4. This is reasonable since the Re value does increase as the characteristic length becomes larger. While the

turbulent kinetic energy distributions at the near wall region look quite similar, it can be determined that the velocity fluctuation in the core area of the tube tends to be stronger as the pitch length decreases and the inner diameter decreases.

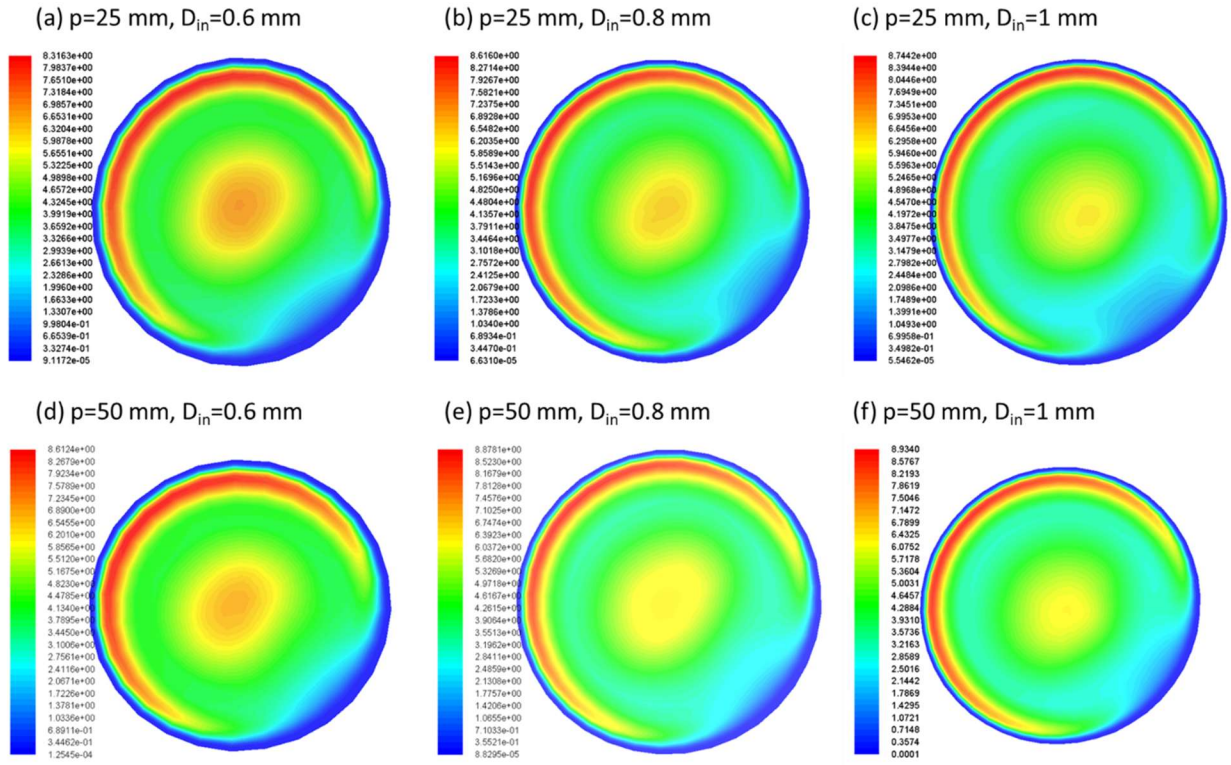

Figure 6.6. The turbulent kinetic energy (m^2/s^2) in the middle cross section of 6 different geometries, under the working condition T_{in}=300 K, u_{in}=28 m/s.

6.2. Nu and friction factor correlation

To quantitatively determine the tube side flow performance of different geometries and build a whole heat exchanger model, the Nu and friction factor correlations are developed. Figure 6.7 and Figure 6.8 show the variation of the Nu and friction factor based on the Re value and geometric parameters, from the simulation of 9 geometries under 6 working conditions. The influence of bundle diameter is quite small, so the bundle diameter is not included in the

correlations. The correlations are shown below, with R-square values as 0.997 and 0.985 respectively, so the goodness of fit is pretty good.

$$Nu = 0.06105Re^{0.71054}\left(\frac{p}{D}\right)^{-0.02156} \tag{6.2}$$

$$f = 2.68097Re^{-0.43137}\left(\frac{p}{D}\right)^{-0.07549} \tag{6.3}$$

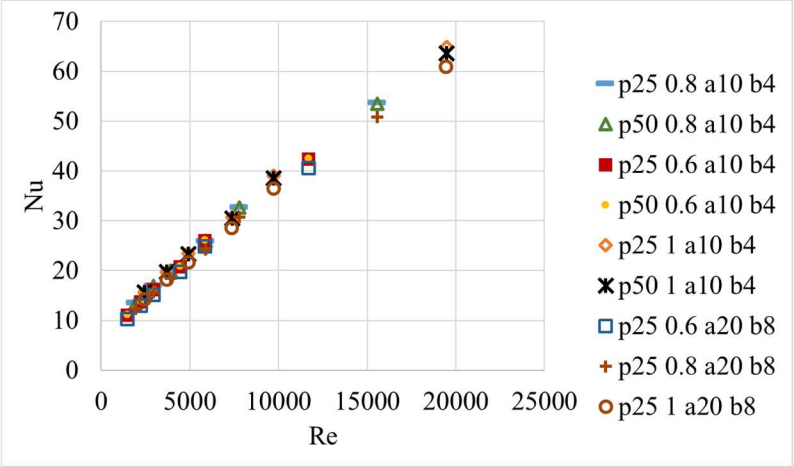

Figure 6.7. The Nu value versus Re value for different geometries. The legend "p25 0.8 a10 b4" means the pitch length is 25 mm, the inner diameter of tube is 0.8 mm, the bundle radius of tube is a+b=14 mm, where a and b are coefficients in the equations generating the tube path.

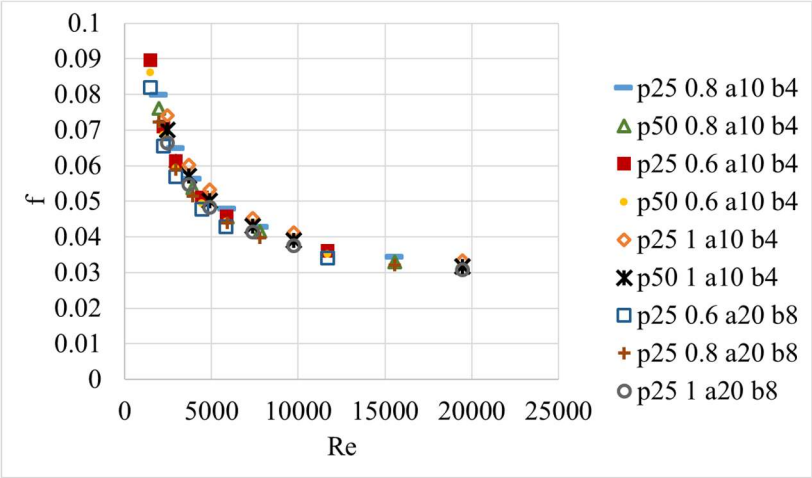

Figure 6.8. The friction factor versus Re value for different geometries. The legend "p25 0.8 a10 b4" means the pitch length is 25 mm, the inner diameter of tube is 0.8 mm, the bundle radius of tube is a+b=14 mm, where a and b are coefficients in the equations generating the tube path.

7. Whole heat exchanger assembly design

In previous chapters, the Nu and friction factor correlations of both shell side and tube side flow are developed, which can be used in the whole heat exchanger model. To make sure the whole heat exchanger model has enough heat exchange length to achieve the objective effectiveness, an overall design is proposed in this chapter, including the details of the assembly configuration and the header design.

7.1. Heat exchange length

Based on the size requirements for the recuperator in this study, the width/length should be less than 0.3 m, and height should be less than 0.7 m. In this geometry, several tubes are twisted into one bundle, and several bundles are twisted into one group. The bundle diameter of a group of tubes consisting of several bundles is 0.028 m, and the shell outer diameter is 0.031 m. To make sure there is enough heat transfer length, 9 groups of tubes go in parallel and turn 180 degree turns for 8 times to occupy a space with both length and width of 0.3 m. The length of the heat exchange section without the header between two adjacent turns is 0.6 m, and there will be 9 identical sections running in series, thus the whole heat exchange length is 5.4 m.

A graph of 9 groups of tubes arranged in parallel is shown in Figure 7.1. In this geometry, one bundle consists of 8 tubes and one group consists of 6 bundles, so totally there will be 432 tubes going in parallel. Figure 7.1 only shows the tube configuration, while each group has an outer shell which is not displayed. The whole heat exchanger model is introduced in detail in the next 2 chapters, and the geometry in Figure 7.1 is found to reach all design objectives.

Figure 7.1. Nine groups of tubes go in parallel, and each group has an outer shell in the actual situation which is not displayed here.

A schematic diagram of the complete arrangement of the tube-shells is shown in Figure 7.2 and Figure 7.3. Two packing configurations are shown respectively, i.e., the square packing method and hexagonal packing method. Here, each blue circle represents a group of tube bundles going in or out of the paper, and the diameter of each shell is 31 mm. The thin red rectangles represent the insulation layer to prevent heat transferred between adjacent groups of 9 shells. The total dimension of the square configuration shown in Figure 7.2 is 279 mm without considering the thickness of the insulation layer. Using the hexagonal packing configuration shown in Figure 7.3 can shorten this distance by 24.9 mm.

Figure 7.3 demonstrates how flow goes through the heat exchanger, by using the same number representing those shells in parallel and using the same letter representing those shells in series. Flow in shells A1, B1, …, I1 goes in parallel into the paper, then turns 180 degrees in the

header at the end, then goes through shells A2, B2, …, I2 out of paper, and so on until A9, B9, …, I9.

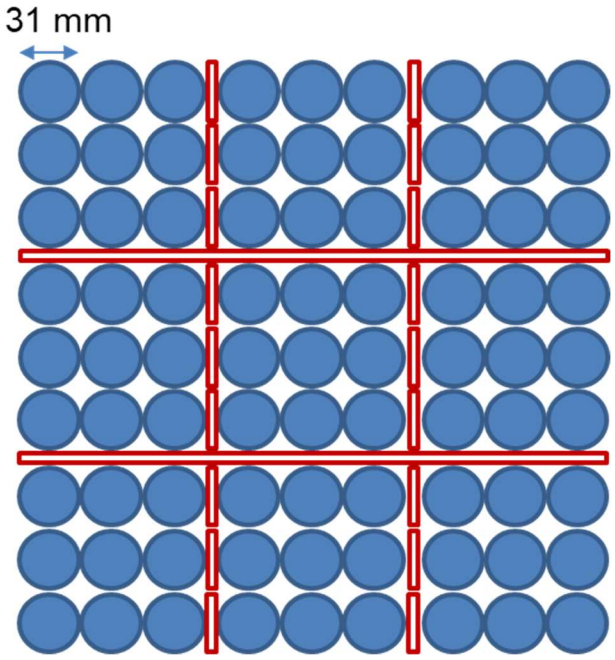

Figure 7.2. Square packing configuration with each blue circle representing one group of tube bundles going in or out of paper, and the thin red rectangles as insulation layers.

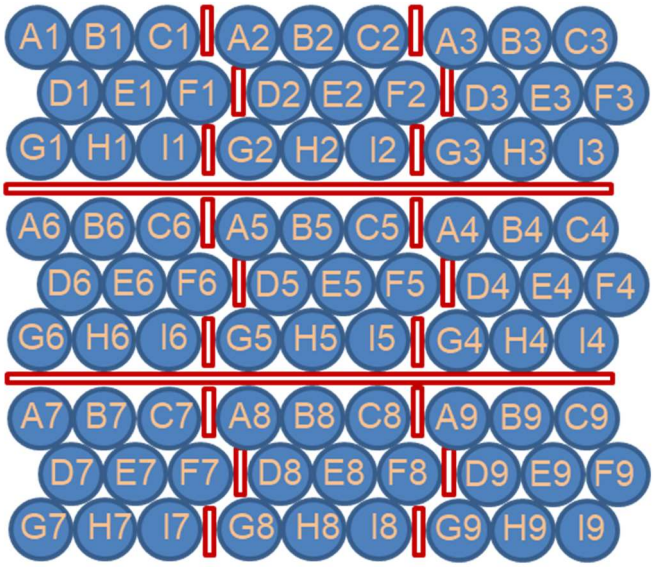

Figure 7.3. Hexagonal packing configuration with each blue circle representing one group of tube bundles going in or out of the paper, and the thin red rectangles as insulation layers.

7.2. Double header system

Although the heat exchanger is designed to realize uniform flow and temperature distribution in both shell and tube side, by promoting fluid mixing in the shell side and generating tubes with the same developing length and average coil diameter, the maldistribution problem may still exist due to unintended variations in the manufacturing process. To reduce the penalty caused by the maldistribution of flow and velocity, both the shell and tube side flow are mixed and redistributed respectively at 180-degree each turn.

For a shell and tube heat exchanger, usually the inlet and outlet of the shell side flow is located at the side of the shell. In this design, the inlet and outlet of the shell side flow are located at the end of the shell as are those of the tube side flow to reduce the heat exchanger size. To mix and redistribute the flow of both sides at the end of each shell, a double header system is designed, shown in Figure 7.4. The details at the end of each shell are shown in Figure 7.5.

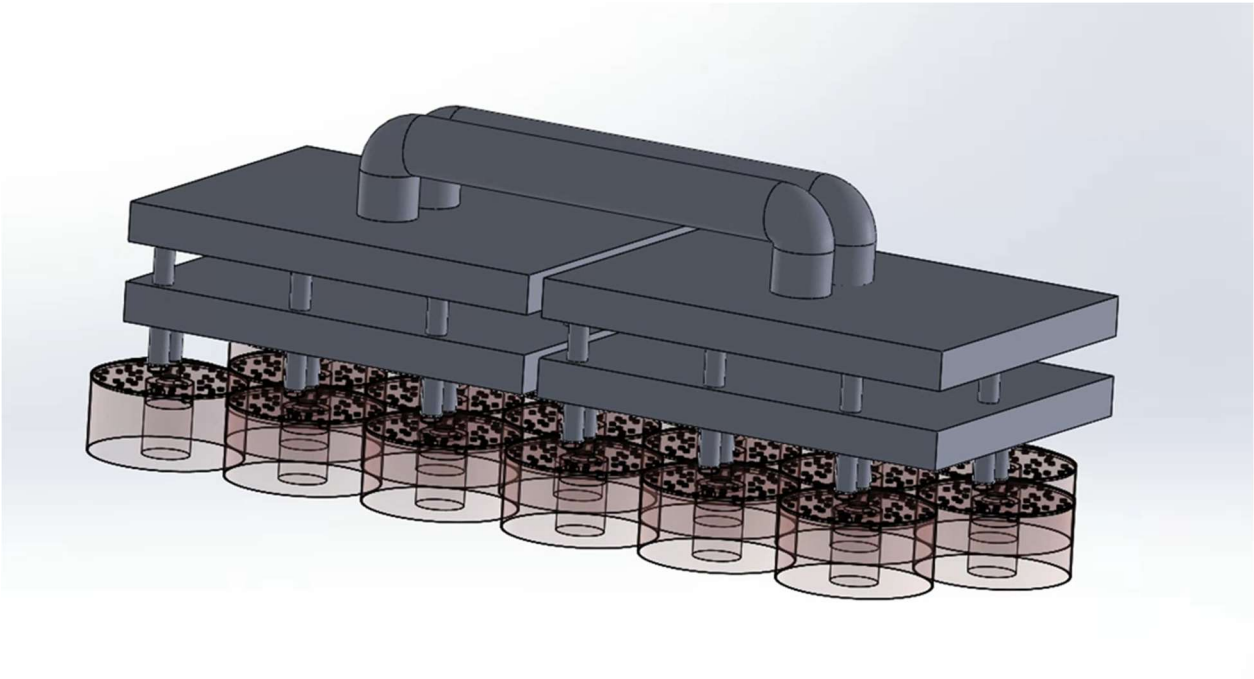

Figure 7.4. Double header system at each turn.

As shown in Figure 7.5, at the outlet of the tube side flow, the fluid will go into a small header first, while flow from a group of tube bundles will be pre-mixed first, and then go into the larger header, where flow from 9 groups of tube bundles will be mixed. Correspondingly, at the inlet of tube side flow, the fluid will be redistributed into 9 shells from the large header first, and then in each shell the fluid will be redistributed into its 48 micro-tubes. This mixing and redistribution occurs 8 times along the whole heat exchanger length, reinforcing the velocity and temperature uniformity for the tube side flow.

For the shell side flow, the end of the mandrel is made to be hollow, as shown in Figure 7.5, and then the shell side flow can go through the mandrel into the double header system shown in Figure 7.4, being mixed and redistributed.

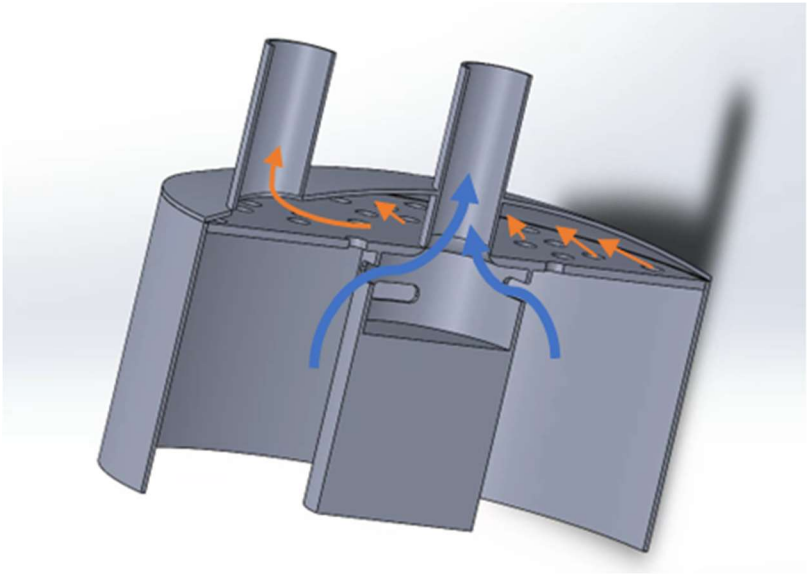

Figure 7.5. Design details at the end of each shell.

Figure 7.6 and Figure 7.7 display the flow path inside the double header system, for the shell side flow and tube side flow respectively. The shell side flow is redistributed in the lower header and goes straight through the upper header, while tube side flow goes straight through the

lower header and is redistributed in the upper header. In this way, both shell and tube side flow will be redistributed at each turn.

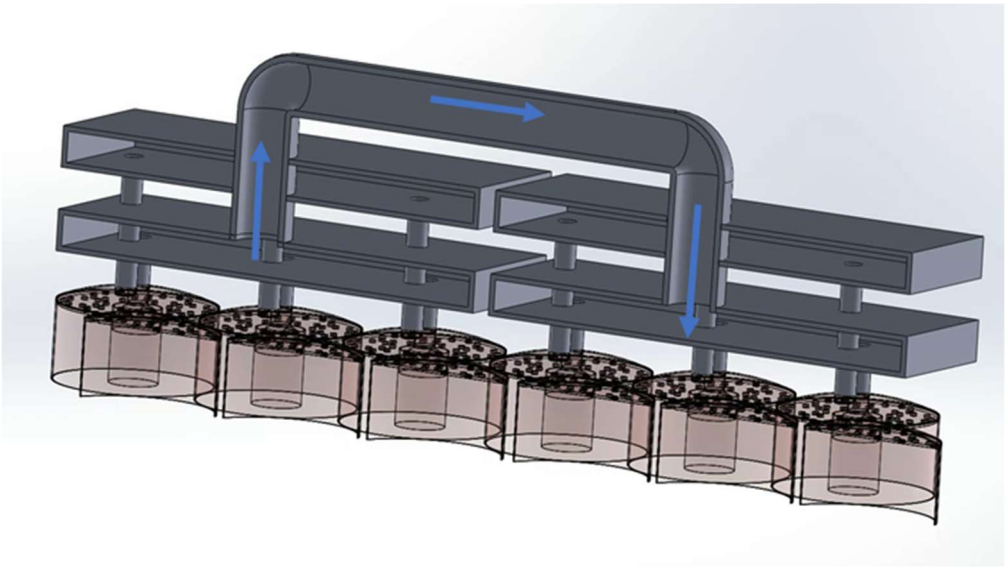

Figure 7.6. Shell side flow path in the double header system.

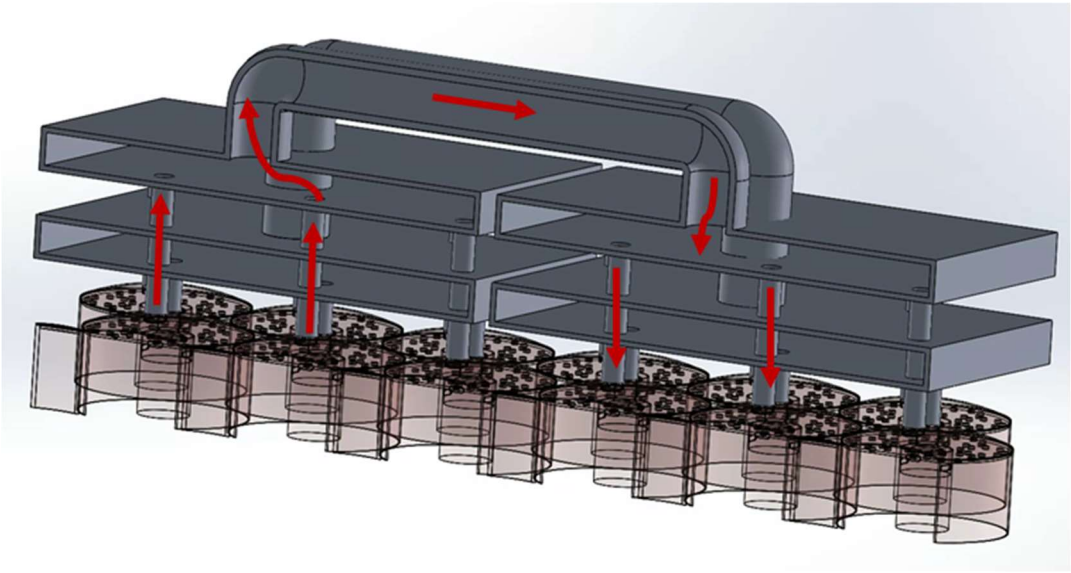

Figure 7.7. Tube side flow path in the double header system.

The pressure drop at each turn and header is related to the shape and size of the headers and the thermal properties of helium. The thermal properties of helium change dramatically from

300 K to 30 K, so the header loss is different at the hot end and the cold end. These minor losses will be discussed and calculated in the next two chapters, after the whole heat exchanger model is introduced and the thermal properties' profiles are obtained.

8. Whole heat exchanger finite difference model

A 1-D finite difference model is built to calculate the effectiveness and pressure drop of the whole heat exchanger, with axial conduction, parasitic heat load and varying thermal properties being considered. Details on the model are introduced in this chapter, including the control volume, energy balance equations, matrix assembly and algorithm.

8.1. Control volume and energy balance equations

While this geometry is a 3-D complicated geometry, it is hard to build a 3-D numerical model, so a 1-D model for a counter flow heat exchanger is applied to simplify the problem. The calculation deviation caused by this simplification will be discussed later. The control volume of the 1-D model is shown in Figure 8.1, including the i^{th} control volume of the hot side, the metal part, and the cold side. In this study, the tube side is the high-pressure hot side, and the shell side is the low-pressure cold side.

For the hot side and cold side, the thermal properties in the i^{th} control volume are evaluated at the average temperature of the $(i-1)^{th}$ node and the i^{th} node. This average temperature is also used to calculate the temperature difference between the fluid side control volume and the metal control volume. Besides the enthalpy flow into and out of the node and the convection heat transferred between the fluid and the metal, the parasitic radiation heat load on the shell side is also considered in the cold side control volume.

For the metal part, the axial conduction is taken into account. The thermal conductivity used to calculate the conduction heat flux between two adjacent metal control volumes is evaluated at the average temperature of those two control volumes.

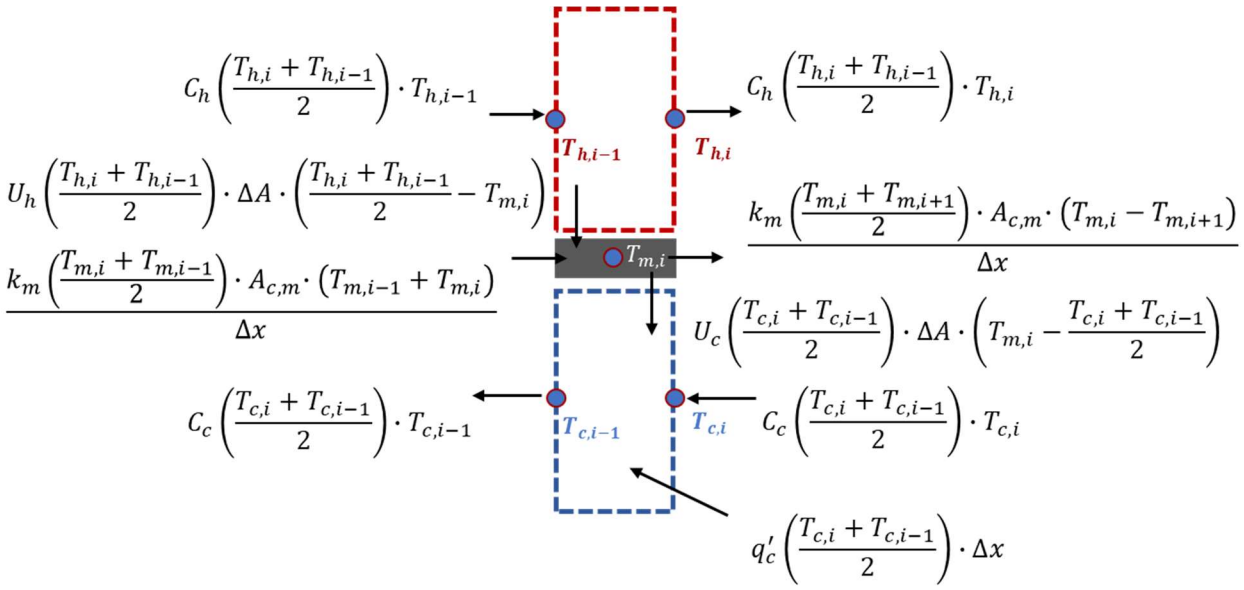

Figure 8.1. Control volume of the i[th] section of the hot side, metal, and cold side.

The energy balance equations for the hot side and cold side control volume can be written:

$$C_h\left(\frac{T_{h,i}+T_{h,i-1}}{2}\right)\cdot T_{h,i-1}=C_h\left(\frac{T_{h,i}+T_{h,i-1}}{2}\right)\cdot T_{h,i}+U_h\left(\frac{T_{h,i}+T_{h,i-1}}{2}\right)\cdot \Delta A_h\cdot\left(\frac{T_{h,i}+T_{h,i-1}}{2}-T_{m,i}\right),\qquad i=2,\dots,n+1 \tag{8.1}$$

$$C_c\left(\frac{T_{c,i}+T_{c,i-1}}{2}\right)\cdot T_{c,i}+U_c\left(\frac{T_{c,i}+T_{c,i-1}}{2}\right)\cdot \Delta A_c\cdot\left(T_{m,i}-\frac{T_{c,i}+T_{c,i-1}}{2}\right)+q'_c\left(\frac{T_{c,i}+T_{c,i-1}}{2}\right)\cdot \Delta x=C_c\left(\frac{T_{c,i}+T_{c,i-1}}{2}\right)\cdot T_{c,i-1},\qquad i=2,\dots,n+1 \tag{8.2}$$

Where C_h and C_c are the heat capacity rate of the hot and cold fluid separately, U_h and U_c are the heat transfer coefficients at the hot side and cold side respectively, ΔA_h and ΔA_c are the heat transfer area of the hot side and cold side in one control volume, q'_c is the parasitic heat load on the shell side per unit length, and Δx is the unit length. Note that the heat capacity rate, heat transfer coefficients and parasitic heat load are functions of the local fluid temperature. The heat transfer coefficients are obtained from the Nu correlations developed in previous chapters.

The energy balance for each metal control volume can be written:

$$U_h\left(\frac{T_{h,i}+T_{h,i-1}}{2}\right)\cdot\Delta A_h\cdot\left(\frac{T_{h,i}+T_{h,i-1}}{2}-T_{m,i}\right)+\frac{k_m\left(\frac{T_{m,i}+T_{m,i-1}}{2}\right)\cdot A_{c,m}\cdot\left(T_{m,i-1}-T_{m,i}\right)}{\Delta x}=$$

$$\frac{k_m\left(\frac{T_{m,i}+T_{m,i+1}}{2}\right)\cdot A_{c,m}\cdot\left(T_{m,i}-T_{m,i+1}\right)}{\Delta x}+U_c\left(\frac{T_{c,i}+T_{c,i-1}}{2}\right)\cdot\Delta A_c\cdot\left(T_{m,i}-\frac{T_{c,i}+T_{c,i-1}}{2}\right),\quad i=2,\dots,n+1 \tag{8.3}$$

Where k_m is the thermal conductivity of the metal at the local temperature, and $A_{c,m}$ is the cross-sectional area of the metal.

8.2. Matrix assembly

To increase the universality of the numerical model and reveal the physical parameters that govern the equation, the energy balance equations, boundary conditions and performance metrics are scaled to be non-dimensional [39]. The nondimensional temperature Θ is defined as:

$$\Theta\equiv\frac{T-T_{c,in}}{T_{h,in}-T_{c,in}} \tag{8.4}$$

The overall heat exchanger length is divided into N+2 sections, shown in Figure 8.2 with the length of the first and last sections as 0 to unify the equation form of the control volumes at the edges and the internal control volumes. Therefore, the length of each internal section can be written:

$$\Delta x=\frac{L}{N} \tag{8.5}$$

The dimensionless axial node position *X* and dimensionless section length ΔX are scaled by the overall heat exchanger length:

$$\mathrm{X}\equiv\frac{x}{L} \tag{8.6}$$

$$\Delta X \equiv \frac{\Delta x}{L} \tag{8.7}$$

For the hot or cold side fluid, there are N+1 nodes, and the non-dimensional axial position of each node is shown as $X_{f,1..N+1}$ in Figure 8.3. For the metal part, there are N+2 nodes, and the non-dimensional axial position of each node is shown as $X_{m,1..N+2}$. The internal nodes of the metal part are located in the middle of each section, while the nodes at the 2 edges of the metal part are located at the two ends of the overall length.

Figure 8.2. The N+2 sections with the length of the first and last one as 0.

Figure 8.3. The non-dimensional axial node position for hot and cold side flow.

Figure 8.4. The non-dimensional axial node position for the metal part.

The heat transfer coefficients on the hot and cold side of the heat exchanger (U_h and U_c, respectively) are scaled to be the number of transfer units (β_h *and* β_c, respectively) by:

$$\beta_h(\Theta_h) \equiv \frac{U_h(T_h) \cdot A_{h,total}}{\min(C_{h,in}, C_{c,in})} \tag{8.8}$$

$$\beta_c(\Theta_c) \equiv \frac{U_c(T_c)\cdot A_{c,total}}{\min\,(C_{h,in},C_{c,in})} \tag{8.9}$$

The thermal conductivity of metal is scaled to be the axial conduction parameter (λ) by:

$$\lambda(\Theta_m) \equiv \frac{k(T_m)\cdot A_{c,m}}{L\cdot\min\,(C_{h,in},C_{c,in})} \tag{8.10}$$

The parasitic heat load is scaled to be the dimensionless parasitic heat transfer rates according to:

$$\chi_c(\Theta_c) = \frac{q'_c(T_c)\cdot L}{\min\,(C_{h,in},C_{c,in})\cdot(T_{h,in}-T_{c,in})} \tag{8.11}$$

The capacity rate on the hot and cold side of the heat exchanger (C_h and C_c, respectively) are scaled to be the number of transfer units ($\mu\ and\ \nu$, respectively) by:

$$\mu(\Theta_h) = \frac{C_h(T_h)}{\min\,(C_{h,in},C_{c,in})} \tag{8.12}$$

$$\nu(\Theta_c) = \frac{C_c(T_c)}{\min\,(C_{h,in},C_{c,in})} \tag{8.13}$$

Dimensionless energy balance equations can be obtained by substituting these definitions into the energy balance equations (8.1) (8.2) (8.3).

The hot side inlet boundary condition can be written as:

$$\Theta_{h,1} = 1 \tag{8.14}$$

The cold side inlet boundary condition can be written as:

$$\Theta_{c,N+1} = 0 \tag{8.15}$$

The hot and cold end of the metal part are set to be adiabatic boundary conditions as:

$$\Theta_{m,1} = \Theta_{m,2} \tag{8.16}$$

$$\Theta_{m,N+1} = \Theta_{m,N+2} \tag{8.17}$$

The non-dimensional energy balance equations with the four boundary conditions form a set of 3n+4 equations, with the same number of unknowns, i.e., the non-dimensional temperature of the hot side, metal, and cold side, $\Theta_{m,1}$, $\Theta_{m,2}$,…, $\Theta_{m,N+2}$, $\Theta_{h,1}$, $\Theta_{h,2}$,…, $\Theta_{h,N+1}$, $\Theta_{c,1}$, $\Theta_{c,2}$,…, $\Theta_{c,N+1}$. These equations can be solved through sparse matrix decomposition, and the algorithm is introduced in next section.

8.3. Algorithm

From the set of equations it can be seen that the coefficients of the matrix are varied with the solution temperature profiles. A weighted relaxation technique is applied to solve the nonlinear system, and its flowchart is illustrated in Figure 8.5. First, the numerical parameters, supplied functions of dimensionless parameters, and boundary conditions are entered. The initial temperature profiles are assumed as follows for hot side, cold side, and metal part respectively.

$$\Theta_{h,i} = 1 - \frac{(i-1)}{N}, i = 1..N+1 \tag{8.18}$$

$$\Theta_{c,i} = 1 - \frac{(i-1)}{N}, i = 1..N+1 \tag{8.19}$$

$$\Theta_{m,i} = 1 - \frac{(i-1)}{N+1}, i = 2..N+1 \tag{8.20}$$

Then the coefficients of the matrix are obtained based on the temperature profiles, supplied functions of thermal properties, and the dimensionless energy balance equations. The matrix is sparse since the number of coefficients are quite small compared with the size of the matrix. The solution profiles in the current step ($\Theta^*_{h,i}$, $\Theta^*_{c\,i}$, and $\Theta^*_{m,i}$) are obtained by decomposing the matrix.

The maximum absolute difference between the new solution ($\Theta^*_{h,i}$, $\Theta^*_{c\,i}$, and $\Theta^*_{m,i}$) and the solution from previous step ($\Theta_{h,i}$, $\Theta_{c,i}$, $\Theta_{m,i}$, note that if this is the first iteration, then compare with the assumed initial temperature profiles) is calculated. If the maximum absolute difference is larger than the relaxation tolerance, the temperature profiles $\Theta_{h,i}$, $\Theta_{c,i}$, $\Theta_{m,i}$ are updated by a weighted average of the old and new solutions. Then the matrix is assembled and decomposed again, and the procedure is repeated. If the maximum absolute difference is smaller than the relaxation tolerance, the model is determined to have converged, the final solution profiles are obtained, and these can be used to calculate the performance of the heat exchanger.

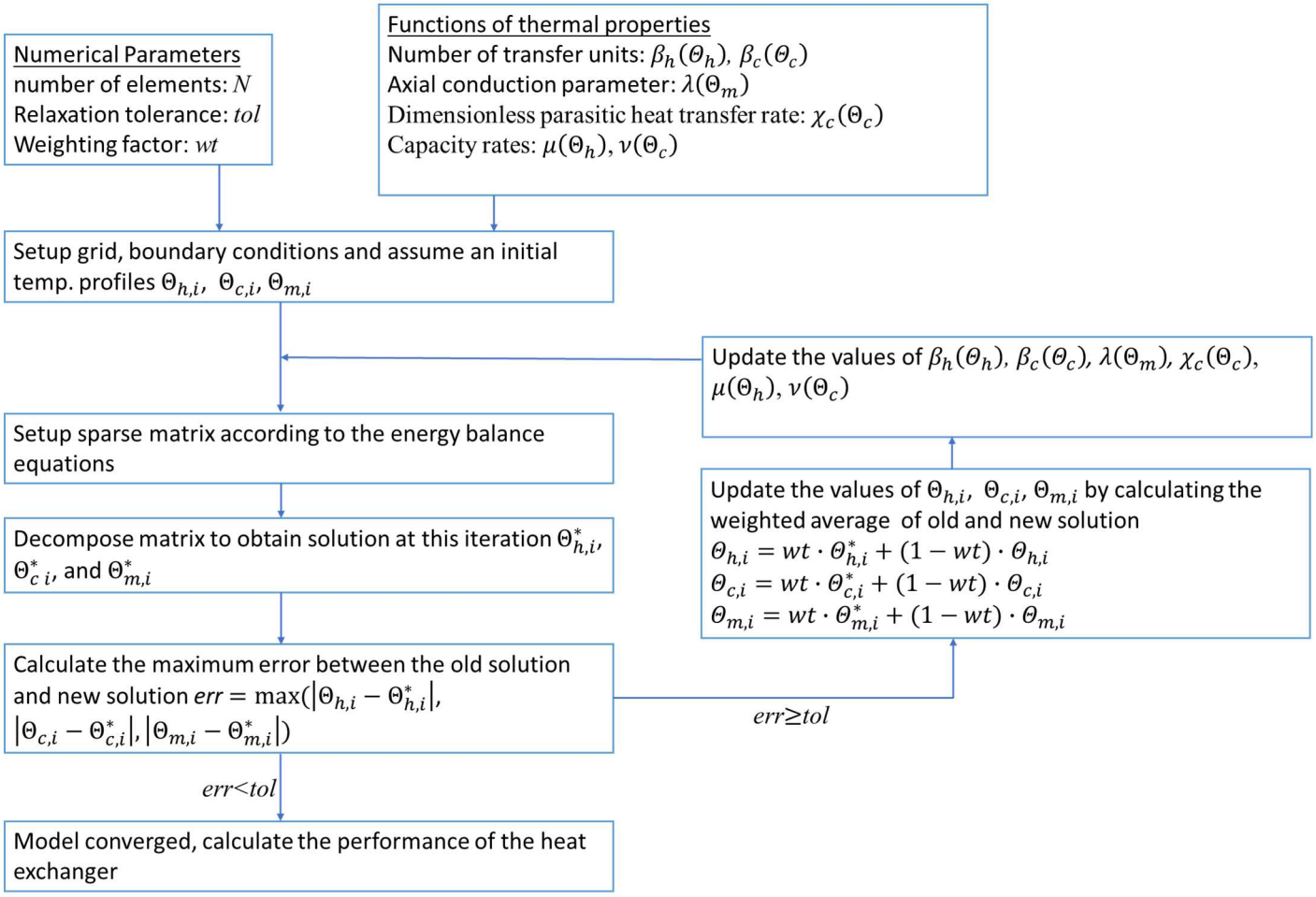

Figure 8.5. Flowchart of the weighted relaxation technique.

9. Whole heat exchanger model results analysis

The design of heat exchangers always encounters a trade-off between high effectiveness and low pressure drop. The performances of various geometries in this work have been obtained by the overall heat exchanger model and compared. The geometry with a pitch length of 25 mm provides a higher effectiveness than the geometry with a pitch length of 50 mm, when other geometry parameters are the same. However, the tube side pressure drop of the form one exceeds the pressure drop requirement (1 bar). Several assumptions have been made while carrying out the fluent simulation and building the overall heat exchanger model, which could introduce error in the estimation of the effectiveness and pressure drop. The assumptions and their consistency will be discussed in this chapter.

9.1. Effectiveness and pressure drop

9.1.1. The geometry that satisfying all design objectives:

For each geometry, the performance is explored with 2 different overall heat exchange lengths, one is 5.4 m and the other is 4.5 m. To obtain the performance of the heat exchanger under a realistic scenario for each overall heat exchanger length, the effectiveness and pressure drop are calculated under both the ideal situation, where there is no radiation parasitic heat load, and the worst case scenario, where there is no insulation layer.

Therefore, for each geometry, the effectiveness and pressure drop are calculated under 4 situations. The results show that for all geometries with a pitch length of 25 mm, although the effectiveness is larger than 0.99 even under the worst case scenario, the pressure drop of the tube side in these 4 cases are all larger than 1e6 Pa, which is much larger than the pressure drop

requirement (<1e5 Pa for both sides). For the geometries with a pitch length of 50 mm, the tube side pressure drop is still larger than 1e5 Pa if there are 36 tubes in one shell, each with an outer diameter of 1mm. As a result, geometries with more, and larger diameter tubes are explored and a geometry satisfying all design requirements has been found.

The geometry consists of 48 tubes in one group, made up of 6 bundles with each bundle consisting of 8 tubes. The tube outer diameter is 1.2 mm, and the inner diameter is 1 mm. The effectiveness and pressure drop under the 4 situations of the heat exchanger with this configuration are listed in Table 9.1. ΔP_h denotes the pressure drop of the high-pressure tube side, and ΔP_c denotes the low-pressure shell side. As shown in the table, only one situation results in a tube side pressure drop a little larger than 1 bar. That situation occurs when the overall heat exchange length is 5.4 m, and there is no insulation layer. The effectiveness values under all 4 situations are larger than 0.99. In addition, the pressure drop of the shell side under all situations is much smaller than 1 bar. Accordingly, this geometry can be determined to reach all design objectives. The configuration in one group is shown in Figure 9.2.

Table 9.1. Performance of a geometry with 48 tubes in one group, and 9 groups in parallel.

	Overall heat exchange length =5.4 m		Overall heat exchange length=4.5 m	
	Without considering radiation parasitic heat load	Without insulation layer	Without considering radiation parasitic heat load	Without insulation layer
Effectiveness	0.9945	0.9915	0.9926	0.9907
ΔP_h (Pa)	6.6935e4	1.0176e5	5.6666e4	7.8618e4
ΔP_c (Pa)	9.2814e2	1.4140e3	7.8435e2	1.0908e3

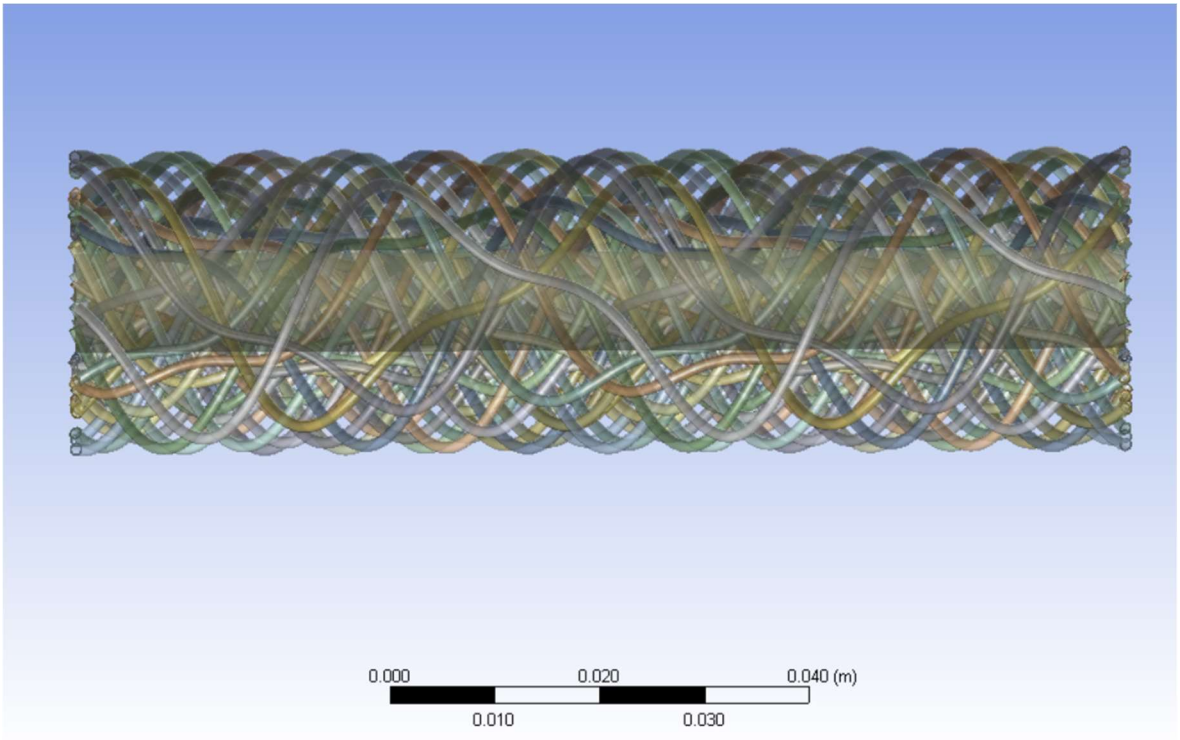

Figure 9.1. Illustration of a group of 48 tubes, with 6 bundles and 8 tubes in each bundle. Pitch length is 50 mm, inner tube diameter is 1mm and outer tube diameter is 1.2 mm.

9.1.2. Minor loss

The pressure drop discussed in the previous section is the major pressure drop occurring along the heat exchange length. Besides the major pressure drop, there exists a minor pressure drop at each of the headers and turns. The header loss is related to the Re value, density, velocity, and head geometry, and it varies significantly from the hot end to the cold end. Figure 9.2, Figure 9.3, Figure 9.4 show the Re, density, velocity profiles from the hot end to the cold end for both shell side and cold side flow respectively. Since the major pressure drop of the shell side is two orders of magnitudes less than the pressure drop limitation, which is 1 bar, there is no need to

calculate the minor loss of the shell side since the total pressure drop is significantly smaller than 1 bar.

The tube side header losses at the hot end and the cold end are obtained based on the thermal properties and header geometry. At the hot end, the contraction loss is 205.7 Pa, and the expansion loss is 177 Pa. At the cold end, the contraction loss is 11.5 Pa, and the expansion loss is 21.1 Pa. The losses at all headers will be less than the value at the hot end. The combined loss from all 8 headers is negligible compared to the major loss. In addition, the total pressure loss of the tube side flow is also under 1 bar even considering the header losses.

The bend loss is also related to the thermal properties of flow and the bend geometry. For the tube side hot end, the pressure drop is 1396 Pa per bend. For the tube side cold end, the value is 171.7 Pa per bend. There are 16 turns for each side along the heat exchanger, and the losses at all bends are less than 1396 Pa and larger than 171.7 Pa. Thus, the total loss of the tube side flow is still under the pressure drop limitation considering the major loss, header loss and bend loss together.

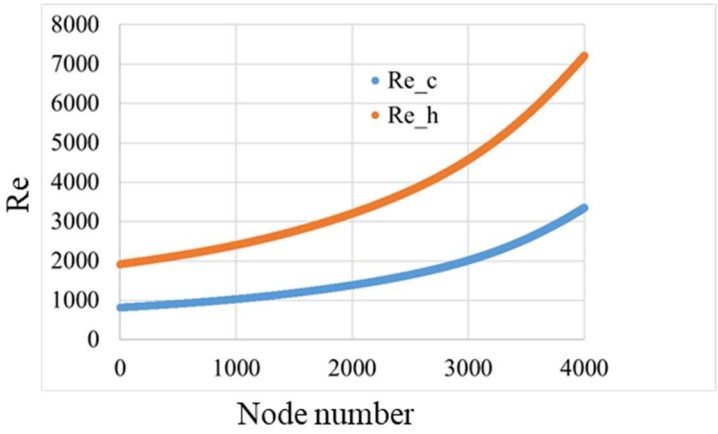

Figure 9.2. Re profiles of the shell side (Re_c) and the tube side (Re_h) along the heat exchanger. Node 1 is the hot end and node 4000 is the cold end.

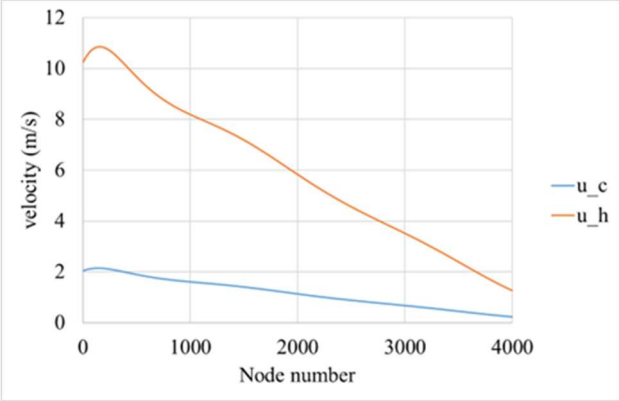

Figure 9.3. Velocity profiles of the shell side (u_c) and the tube side (u_h) along the heat exchanger. Node 1 is the hot end and node 4000 is the cold end.

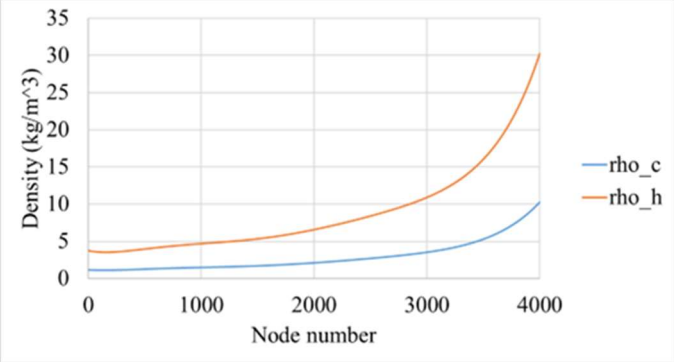

Figure 9.4. Density profiles of the shell side (rho_c) and the tube side (rho_h) along the heat exchanger. Node 1 is the hot end and node 4000 is the cold end.

9.2. Assumption verification

Several assumptions are made in the process of calculating the effectiveness. Firstly, in the fluent simulation the boundary conditions are set to constant heat flux boundary conditions, even though the conditions are neither constant heat flux nor constant temperature in realistic scenarios. Secondly, for the overall heat exchanger model, the problem is simplified to be a 1D pure counter flow model, although the real geometry is 3D and the configuration is somewhere between pure counter flow and pure cross flow. The 1D assumption also implies that the flow and temperature are uniform for both shell and tube side. These assumptions may overestimate the effectiveness.

To understand whether these assumptions are reasonable and to explore the extent to which the effectiveness is miscalculated, two additional studies have been conducted. In the first, more realistic boundary conditions are explored by simulating a complete geometry model that includes the shell and tube side together. The second additional study compares the difference between a pure counter-flow and a pure cross-flow model.

9.2.1. Exploration of the realistic boundary conditions

In previous chapters, the simulations of the shell side flow and the tube side flow are carried out separately to reduce the computation cost. To incorporate more realistic boundary conditions, the complete geometry model containing the shell side, the metal tube-wall component, and the tube side is simulated, as shown in Figure 9.5. For the metal tube wall component, the virtual wall and shell conduction setting in Fluent are applied. The shell conduction feature in Fluent can calculate the heat conduction in the wall in both normal and planar direction without generating a real mesh. A conformal mesh is generated at the interface of the shell and tube sides, which means the two sides share the same nodes at the interface.

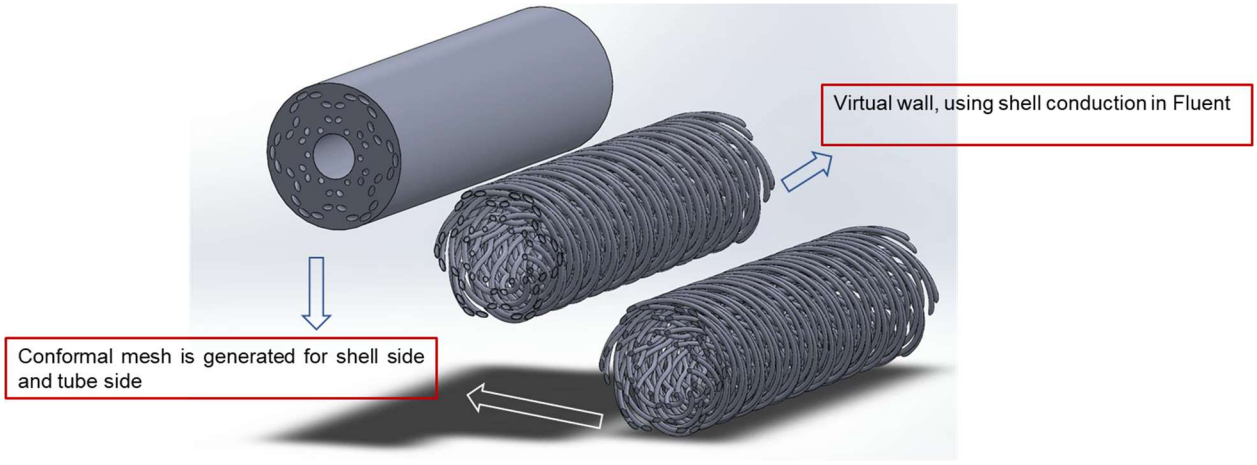

Figure 9.5. Whole geometry model containing the shell side, metal part and tube side.

Figure 9.5 shows a geometry with 48 tubes and a shell outer diameter of 31 mm. If this geometry is used to build a complete geometry model, it will require more than 100 million cells. It will be very hard to load the file due to the memory limitation and converge. Consequently, a smaller shell with only 12 tubes is simulated instead, and the model converges successfully. Figure 9.6 demonstrates the temperature profiles of the shell side flow and tube side flow. Figure 9.7 demonstrates the wall temperature profiles along the heat exchanger using the same colormap as in Figure 9.6. The left side is the inlet of the tube side flow and outlet of the shell side flow, and the right side is the inlet of the shell side flow and the outlet of the tube side flow. It can be observed that all three temperatures change gradually and linearly, and the shell side flow temperature tends to be more and more uniform from the right end to the left end.

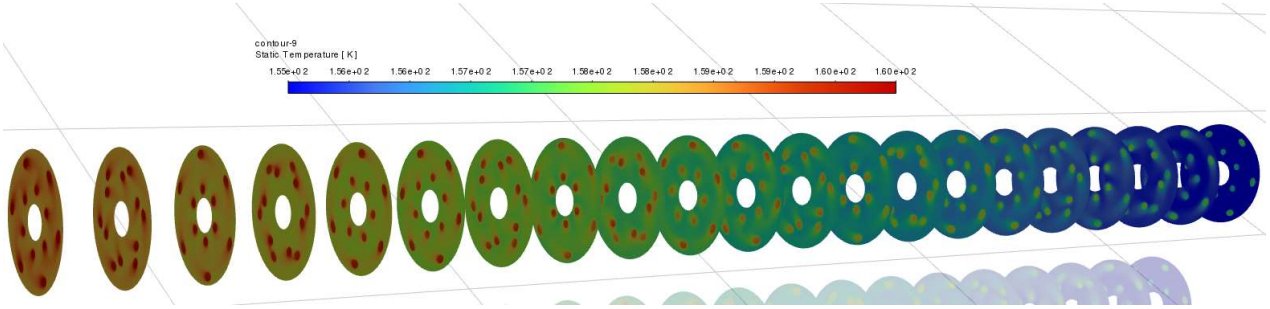

Figure 9.6. Shell side and tube side temperature distribution for a geometry with 12 tubes.

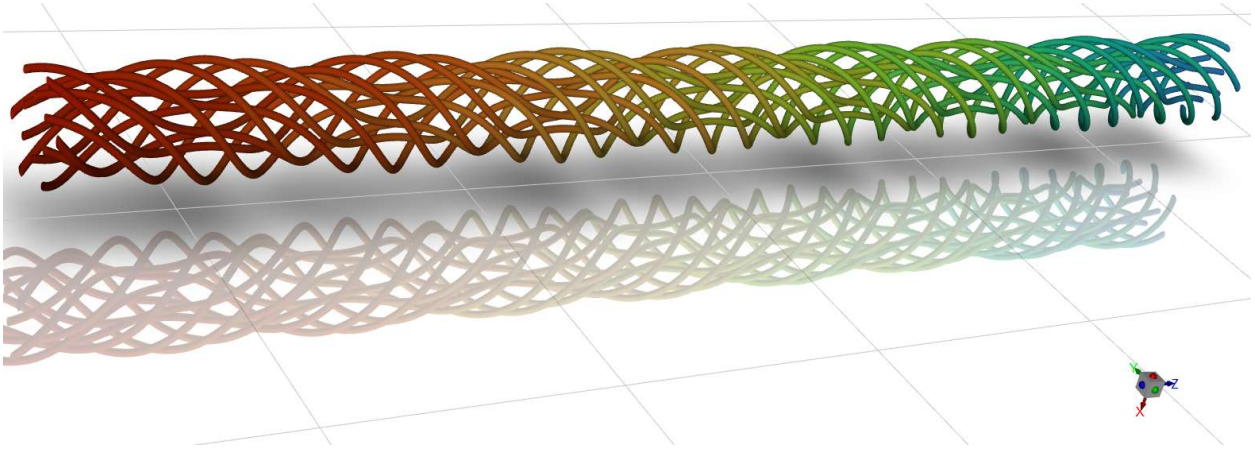

Figure 9.7. Wall temperature distribution for a geometry with 12 tubes.

To decide which boundary condition is closer to the realistic situation, the constant heat flux boundary or the constant temperature boundary condition, the temperature profiles of the bulk flow in the tube side obtained from the whole geometry model are compared with those from the models using the two boundary conditions. Those profiles are shown in Figure 9.8 (from the whole geometry model), Figure 9.9 (from the model using the constant heat flux boundary condition) and Figure 9.10 (from the model using the constant temperature boundary condition). The temperature distribution from the whole geometry model is more similar to that from the constant heat flux model since both of them decrease linearly along the heat exchanger. However, in the case of the constant temperature boundary condition, most of the temperature drop happens near the inlet and then the temperature tends to be steady. Therefore, it can be determined that it is reasonable to use the constant heat flux boundary condition.

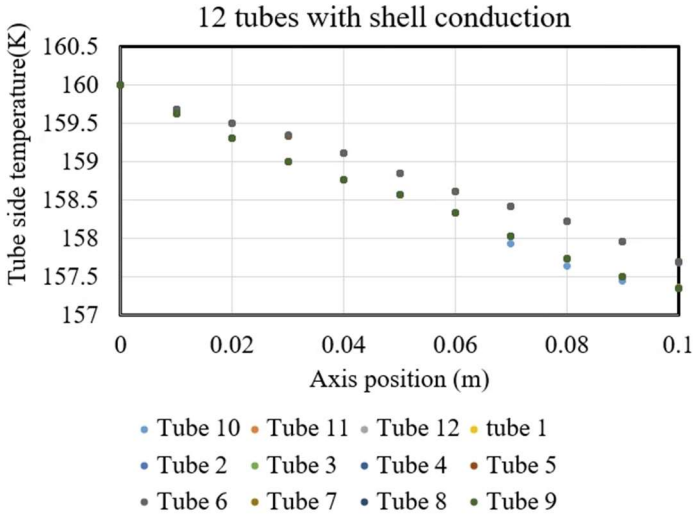

Figure 9.8. Temperature variation of flow in 12 tubes along the heat exchanger obtained from the whole geometry model.

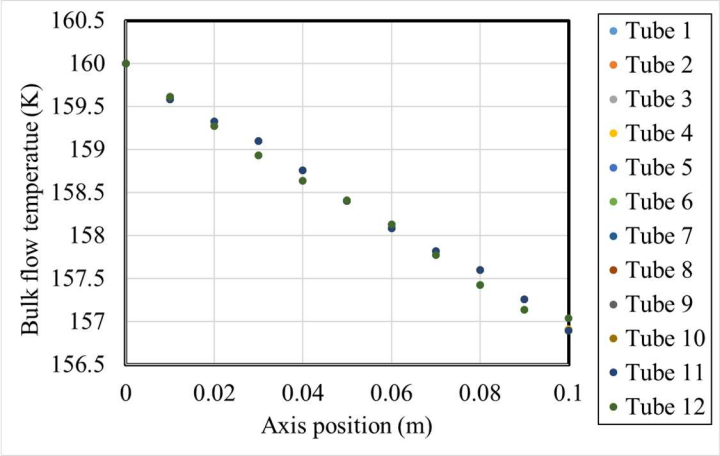

Figure 9.9. Temperature variation of flow in 12 tubes along the heat exchanger obtained from the model using constant heat flux boundary conditions.

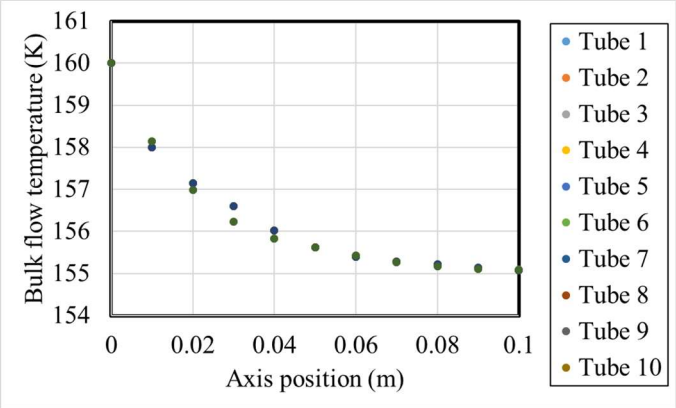

Figure 9.10. Temperature variation of flow in 12 tubes along the heat exchanger obtained from the model using constant temperature boundary conditions.

Figure 9.8 displays a slight temperature difference between the 12 tubes, which may be caused by the initial phase difference between the curves of two tubes in one bundle. In this geometry, 2 tubes are twisted into each of the 6 bundles, so the initial phase difference between the two tubes in one bundle is 2π /2. In a model that included 8 tubes in one bundle, the initial phase difference would only be 2π /8, and it can be assumed that the temperature difference among tubes caused by the initial phase difference would be much smaller.

9.2.2. Difference between pure counter flow and pure cross flow configuration

A pure counter flow model is applied to estimate the effectiveness, while the configuration of the real geometry is somewhere between pure counter flow and pure cross flow. To decide to which configuration this geometry is more similar, the angle θ between each tube and the axial direction is calculated for a heat exchanger with a pitch length of 50 mm. The profiles of the cos θ variation along the heat exchanger are shown in Figure 9.11, where the x axis is the axial position with a unit of mm. It is illustrated that for each tube, the angle varies continuously, with cos θ varying from 0.4 to 1. If cos θ equals 1, the configuration is the pure counter flow. If cos θ equals 0, it is the pure cross flow. The average cos θ of the six tubes in one bundle (the dash line in Figure 9.11), which is also the angle between the bundle and the axis direction, remains the same along the heat exchanger (as shown in Figure 9.12). The average value of cos θ is 0.6, so this geometry is closer to pure counter flow than pure cross flow.

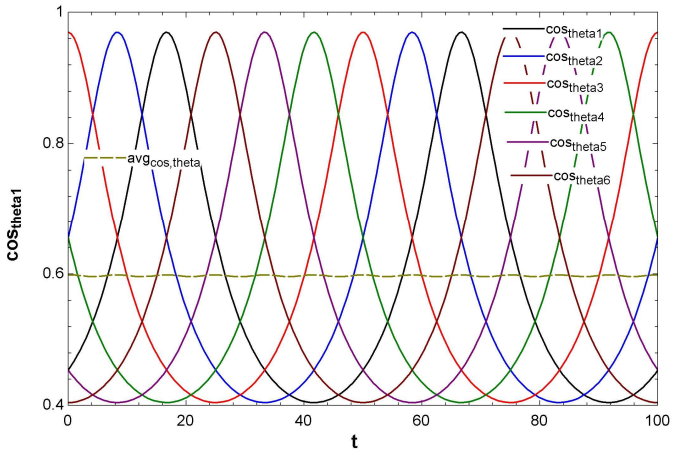

Figure 9.11. The variation of angle between each tube and axis direction.

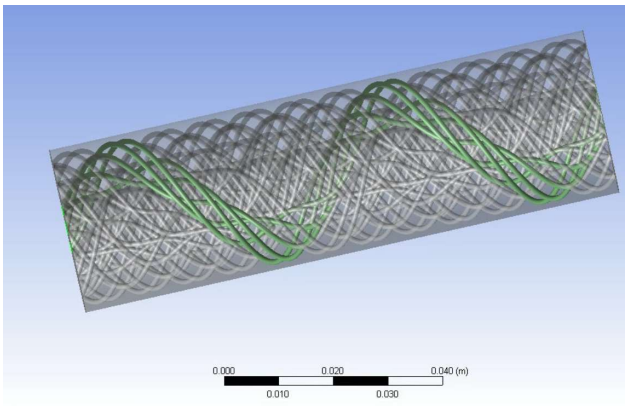

Figure 9.12. The angle between the bundle and axis direction remains the same along the heat exchanger.

To evaluate the difference between the pure counter flow model and pure cross flow model, the effectiveness of each section is calculated by the NTU-effectiveness correlations of both configurations. The correlation of the pure counter flow configuration is:

$$\varepsilon = \begin{cases} \frac{1-exp[-NTU(1-C_R)]}{1-C_R exp[-NT\ \ (1-C_R)]} & for\ C_R < 1 \\ \frac{NTU}{1+NTU} & for\ C_R = 1 \end{cases} \tag{9.1}$$

The correlation of the pure cross flow configuration is:

$$\varepsilon = 1 - exp\left[\frac{NTU^{0.22}}{C_R}\{exp(-C_R NTU^{0.78}) - 1\}\right] \tag{9.2}$$

To use these configurations to calculate the effectiveness of each section, first the temperature profiles of the shell side, metal, and cold side (shown in Figure 9.13) are obtained from the numerical model. Then the thermal resistance of the shell side, metal and cold side can be calculated, and the profiles of NTU and capacity ratio (shown in Figure 9.14) of each section can be calculated. By substituting the NTU and capacity ratio values into equations (9.1) and (9.2), the effectiveness values of each section along the heat exchanger are obtained for both configurations, as shown in Figure 9.15.

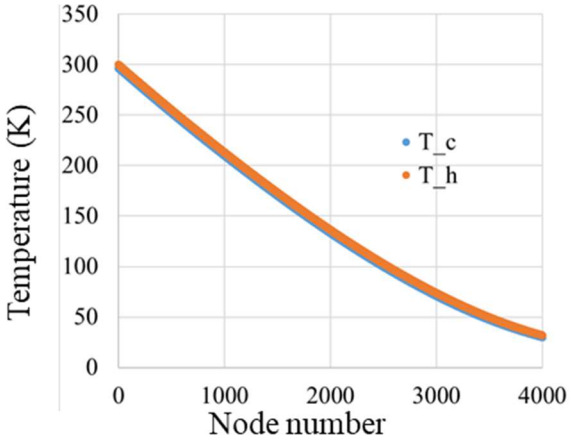

Figure 9.13. The temperature profiles of the shell side and cold side, obtained from the numerical model.

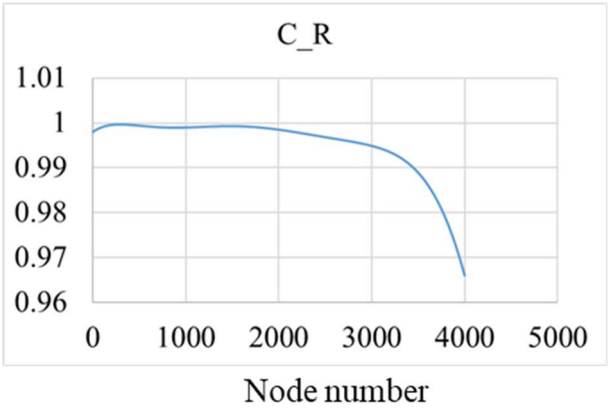

Figure 9.14. The capacity ratio profile, obtained from the numerical model.

In Figure 9.15, the comparison between the pure counter flow configuration (legend co) and pure cross flow configuration (legend cr) is carried out on three different geometries, with the pitch lengths of 40 mm, 50 mm and 60 mm respectively. It can be observed that the effectiveness increases as the pitch length decreases. For each geometry, the difference between the effectiveness from the pure counter flow configuration and that from the pure cross flow configuration is larger at the hod end, and almost disappears at the cold end. And the largest

difference is less than 1%. In conclusion, the calculation deviation caused by using pure counter flow model is negligible.

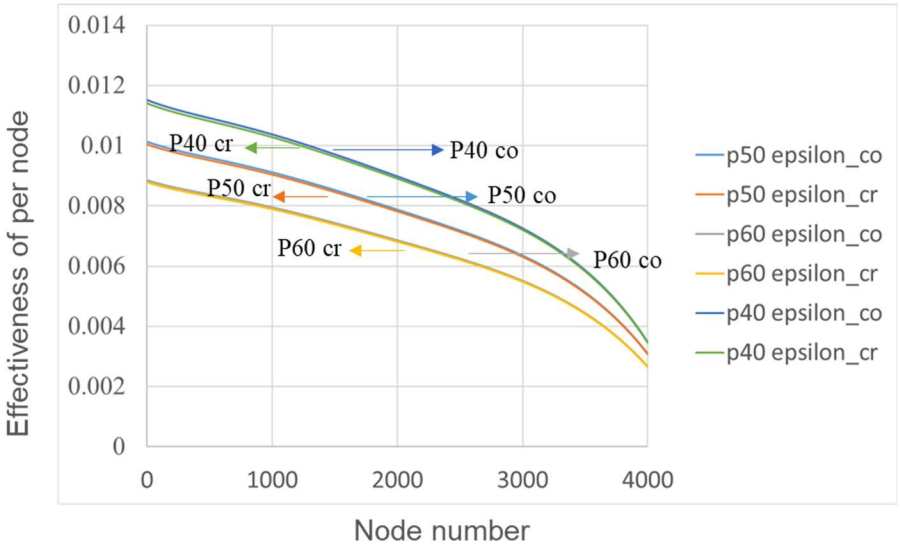

Figure 9.15. The difference of effectiveness of per node between pure counter flow and pure cross flow.

10. Conclusion and future work

10.1. A novel geometry design for recuperators

In this study, a novel design of recuperators with meso-scale helical tube bundles is examined. The basic design idea is twisting several tubes into one bundle and then twisting several bundles into one group, and flow in several groups goes in parallel. This design has two advantages, first all tubes keep changing their position in the radial direction by spiraling in and out in each period, thereby promoting fluid mixing and reinforcing the uniform flow and temperature distribution for the shell side flow. Second, the path of each tube is generated by 3D sinusoidal equations, with the same total length and average coil diameter, which is important for weakening the maldistribution problem for the tube side flow.

The geometry can be specified by the pitch length, tube diameter, number of tubes in one bundle, and the number of bundles. Various geometries with different values of these parameters have been investigated. To accurately account for the influence of the tube distribution, the conduction shape factor concept is “borrowed” from the conduction heat transfer field. Separate fluent simulations have been carried out for the shell side and tube side flow. Based on the simulation results of various geometries under various working conditions, the Nu and friction factor correlations for both sides have been developed with a high-quality fit.

The study on vortex structure is quite inspiring since the average vorticity magnitude on the Q iso-surface has a strong relationship with the corresponding conductance. The relationship is shown to depend on temperature and suggests that mixing is a more dominant factor determining heat transfer at low temperature. To build a correlation between vorticity magnitude and conductance, a coefficient measuring how dominant the mixing is under various temperatures

should be considered. If a relationship can be developed among geometry parameters, vorticity magnitude and conductance, it will be much more helpful to optimize the heat exchanger design. There are many different methods of visualizing vortical structure other than using the Q iso-surface, and they should be investigated and compared. In future, for both the shell and tube side flow, the vortex and turbulence structure should be visualized and analyzed, to explore how various geometry parameters influence the turbulence and in turn, the heat transfer efficiency.

In this study, the thermal and hydraulic performances under the ideal situation with no manufacturing errors have been explored. In the future, models including arbitrary errors caused by manufacturing process should be built and simulated, to explore the maldistribution problem and its influence on the thermal performances.

10.2. Design of the overall heat exchanger

The overall heat exchanger assembly design is proposed with a configuration of 9 groups of tube bundles going in parallel for 0.6 m and turning 180 degrees, a total of eight times to occupy a space with both length and width of 0.3 m. To reduce the effect of maldistribution caused by unintended variations in the manufacturing process, both the shell side flow and tube side flow are mixed and redistributed in the header at each 180-degree turn to reinforce the uniform distribution of velocity and temperature. To achieve this function, a double-header system is designed.

This recuperator design is flexible and universal. The configuration in each shell, number of shells and assembly of shells can be manipulated to cater to various design objectives. In the future, machine learning and optimization algorithms may be applied to find the optimal design for different design objectives.

10.3. Development of an overall heat exchanger model

To calculate the effectiveness and pressure drop of the heat exchanger and find the configuration that satisfies all design objectives, a whole heat exchanger model has been built using Matlab along with the Nu, friction factor correlations as inputs. To improve the accuracy of the model, axial conduction, thermal properties variation with temperature and parasitic heat load have been considered. A weighted relaxation technique is applied to solve the nonlinear system.

The pressure drop for the tube side flow limits the choice of geometries. For all geometries with a pitch length of 25 mm, the pressure drop in the tube side exceeds the pressure drop limitation. A configuration with a pitch length of 50 mm, a tube outer diameter of 1.2 mm and tube inner diameter of 1 mm, with 8 tubes in one bundle, 6 bundles in one group and 9 groups going in parallel has been found to meet all design requirements (effectiveness>0.99 with mass flow rate up to 13 g/s, pressure drop<1 bar for both sides, and the mass and volume limits). The minor losses at the bends and headers are also checked and the total pressure is still under 1 bar for both sides considering the minors losses.

The problem has been simplified to be a 1D counter flow problem, while the real geometry is neither the pure counter flow nor pure cross flow. The difference between the pure counter flow configuration and pure cross flow configuration is analyzed through the NTU-effectiveness method. It is shown that under the NTU and capacity ratio profiles along the geometry and from 300 K to 30 K, the effectiveness values of each sub heat exchanger (1 mm long section) obtained from the two configurations are almost the same, with the largest difference smaller than 1%. Accordingly, it can be determined that it is reasonable to utilize the pure counter flow model.

The boundary condition in the real situation is explored by simulating a whole geometry model containing both the shell side, tube side and a virtual wall. Based on the comparison of the

tube side temperature profile from the whole geometry model, the model using the constant heat flux boundary condition and the model using the constant temperature boundary condition, it is found that the boundary condition in the real situation is closer to the constant heat flux boundary condition than to the constant temperature boundary condition.

The 1D numerical model assumes that the temperature and velocity is uniform for both the shell side and tube side, which is impossible in realistic scenarios. In the future, the model considering random flow passage imbalance should be built and the influence of the maldistribution should be explored.

References.

[1] R. Radebaugh, “Cryocoolers: the state of the art and recent developments,” J. Phys.: Condens. Matter 21 (2009), 164219.

[2] R. Radebaugh, “Review of refrigeration methods,” in Handbook of Superconducting Materials, 2nd edition, D.A. Carwell and D. Larbalestier editors, Taylor and Francis Books (2020) to be published.

[3] Chen, Hui, et al. "Optimization of miniature Joule-Thomson cryocooler with non-isometric recuperator on transient characteristics." Energy 267 (2023): 126552.

[4] Maytal, Ben-Zion, and John M. Pfotenhauer. Miniature Joule-Thomson cryocooling: principles and practice. Springer Science & Business Media, 2012.

[5] Niblock, A., K. Cragin, and M. Zagarola. "High Effectiveness Micro Tube Recuperators for Low Capacity Turbo Brayton Cryocoolers for Space." (2021).

[6] Zagarola, Mark V., and John A. McCormick. "High-capacity turbo-Brayton cryocoolers for space applications." Cryogenics 46.2-3 (2006): 169-175.

[7] Nellis G, Dolan F, McCormick J, et al. Reverse Brayton cryocooler for NICMOS[J]. Cryocoolers 10, 2002: 431-438.

[8] Hill, Roger W., et al. "A recuperative heat exchanger for space-borne turbo-Brayton cryocoolers." International Cryocooler Conference, 2007.

[9] Deserranno, D., et al. "Performance testing of a high effectiveness recuperator for high capacity turbo-brayton cryocoolers." International Cryocooler Conference. Vol. 19. 2016.

[10] J. Deltor, “Progress Towards Gas Mixture Selection and Heat Transfer Coefficient Measurements for the Shell-Side of a Joule-Thomson Cryocooler [dissertation],” Madison: Univ. of Wisc. Madison, Available from: UW Madison Library System, 2023.

[11] Wei, Chenxi, Hui Chen, and Yingwen Liu. "Numerically investigated on the transient performance of fast cool-down JT cryocoolers with non-isometric structure." International Journal of Refrigeration 134 (2022): 74-85.

[12] Mehendale S S, Jacobi A M and Shah R K 2000 Fluid Flow and Heat Transfer at Micro- and Meso-Scales With Application to Heat Exchanger Design Appl. Mech. Rev. 175-193.

[13] Wang B X and Peng X F 1994 Experimental investigation on liquid forced-convection heat transfer through microchannels Int. J. Heat Mass Transf. 37: 73-82.

[14] Gui F and Scaringe R P 1995 Enhanced heat transfer in the entrance region of microchannels American Society of Mechanical Engineers New York No. CONF 950729.

[15] Rush, T. A., T. A. Newell, and A. M. Jacobi. "An experimental study of flow and heat transfer in sinusoidal wavy passages." International journal of heat and mass transfer 42.9 (1999): 1541-1553.

[16] Sivashanmugam P and Suresh S 2007 Experimental studies on heat transfer and friction factor characteristics of turbulent flow through a circular tube fitted with regularly spaced helical screw-tape inserts Appl. Therm. Eng. 27(8-9) 1311-19.

[17] Zhang J F, He Y L and Tao W Q 2009 3D numerical simulation on shell-and-tube heat exchangers with middle-overlapped helical baffles and continuous baffles–Part I: Numerical model and results of whole heat exchanger with middle-overlapped helical baffles Int. J. Heat Mass Transf. 52.23-24: 5371-80.

[18] Zhang J F, He Y L and Tao W Q 2009 3D numerical simulation on shell-and-tube heat exchangers with middle-overlapped helical baffles and continuous baffles–Part II: Simulation results of periodic model and comparison between continuous and noncontinuous helical baffles Int. J. Heat Mass Transf. 52.23-24: 5381-89.

[19] Jayakumar J S, Mahajani S M, Mandal J C, Iyer K N and Vijayan P K 2010 CFD analysis of single-phase flows inside helically coiled tubes Comput. Chem. Eng. 34(4) 430-446.

[20] Zachár A 2010 Analysis of coiled-tube heat exchangers to improve heat transfer rate with spirally corrugated wall Int. J. Heat Mass Transf. 53(19-20) 3928-39.

[21] Chen Y P, Sheng Y J, Dong C and Wu J F 2013 Numerical simulation on flow field in circumferential overlap trisection helical baffle heat exchanger Appl. Therm. Eng. 50(1) 1035-43.

[22] Tan X H, Zhu D S, Zhou G Y and Yang L 2013 3D numerical simulation on the shell side heat transfer and pressure drop performances of twisted oval tube heat exchanger Int. J. Heat Mass Transf. 65 244-253.

[23] Khoshvaght-Aliabadi M, Pazdar S and Sartipzadeh O 2016 Experimental investigation of water based nanofluid containing copper nanoparticles across helical microtubes Int. Commun. Heat Mass Transf. 70 84-92.

[24] Alimoradi A and Veysi F 2016 Prediction of heat transfer coefficients of shell and coiled tube heat exchangers using numerical method and experimental validation Int. J. Therm. Sci. 107 196-208.

[25] Rasheed A H, Alias H, Salman S D. Effects of Coil Pitch Spacing on Heat Transfer Performance of Nanofluid Turbulent Flow through Helical Microtube Heat Exchanger[J]. International Journal of Engineering & Technology, 2018, 7(4.14): 356-360.

[26] Neeraas B O, Fredheim A O and Aunan B 2004 Experimental shell-side heat transfer and pressure drop in gas flow for spiral-wound LNG heat exchanger Int. J. Heat Mass Transf. 47(2) 353-361.

[27] Heat Exchanger Design Handbook, Section 2.5.3 Banks of Plain and Finned Tubes, Bergell House, Inc, 1998.

[28] C. Barbe, D. Mordillat, D. Roger, Pertes de charge enecoulement monophasic et diphasic dans la calandre des exchangeurs bobines, XII Journees de l'Hydraulique, Paris, 1972.

[29] Genić S B, Jaćimović B M, Jarić M S, Budimir N J and Dobrnjac M M 2012 Research on the shell-side thermal performances of heat exchangers with helical tube coils Int. J. Heat Mass Transf. 55(15-16) 4295-4300.

[30] Abolmaali A M and Afshin H 2019 Development of Nusselt number and friction factor correlations for the shell side of spiral-wound heat exchangers Int. J. Therm. Sci. 139 105-117.

[31] Sharqawy M H, Saad S M, and Ahmed K K 2019 Effect of flow configuration on the performance of spiral-wound heat exchanger Appl. Therm. Eng. 161 114157.

[32] Taguchi G and Cariapa V 1993 Taguchi on robust technology development 336-337.

[33] Zeng M, Zhang G, Li Y, Niu Y, Ma Y and Wang Q 2015 Geometrical parametric analysis of flow and heat transfer in the shell side of a spiral-wound heat exchanger Heat Transf. Eng. 36(9) 790-805.

[34] Miansari M, Valipour M A, Arasteh H and Toghraie D 2020 Energy and exergy analysis and optimization of helically grooved shell and tube heat exchangers by using Taguchi experimental design J. Therm. Anal. Calorim. 139(5) 3151-64.

[35] Fluent theory guide.

[36] Jiménez, Javier, et al. "Turbulent boundary layers and channels at moderate Reynolds numbers." Journal of Fluid Mechanics 657 (2010): 335-360.

[37] Pope, Stephen B.. Turbulent flows. Cambridge university press, 2000.

[38] https://www.m4-engineering.com/q-criterion-for-vortex-visualization/.

[39] Nellis, G. F. "A heat exchanger model that includes axial conduction, parasitic heat loads, and property variations." Cryogenics 43.9 (2003): 523-538.

Appendix.

Appendix A. Matlab code for the overall heat exchanger model

"Main code"

```
clear;
clear global;
clc;

global alpha_r Cmin Thin Tcin mdot L L_tube A_shell_cross A_tube_cross Dh_shell p
D_tube D_tube_inner N_tube N_group A_heat_transfer_shell A_prime_tube
A_heat_transfer_tube A_metal_cross SF DD phi_c_in phi_h_in

tic; %start timing

wt=0.3;     %relaxation weighting parameter
mhot='a';   %hot side metal adiabatic boundary condition
mcold='a';  %cold side metal adiabatic boundary condition
g=0;        %grid concentration factor
tol1=1e-5;   %absolute tolerance
tol2=1e-5;
n=5400;      %# of discrete elements
%Inlet temperatures(K)
Thin=300;
Tcin=30;
%mass flow rate(kg/s)
mdot=0.013;

%capacitance rate of helium @ P=2206 kPa, 30 K <= T <= 300 K
Ch_in=mdot.*(4.7518E-11*Thin^6 - 5.2560E-08*Thin^5 + 2.3400E-05*Thin^4 - 5.3599E-
03*Thin^3 + 6.6799E-01*Thin^2 - 4.3524E+01*Thin + 6.4003E+03);
%capacitance rate of helium @ P=689.5 kPa, 30 K <= T <= 300 K
Cc_in=mdot.*(1.8728E-11*Tcin^6 - 2.0759E-08*Tcin^5 + 9.2492E-06*Tcin^4 - 2.1160E-
03*Tcin^3 + 2.6250E-01*Tcin^2 - 1.6925E+01*Tcin + 5.6528E+03);
Cmin=min(Ch_in,Cc_in);

%%%Geometry 48 p50 1.2 1 9 groups
L=5.4; %Heat exchanger length (m)
L_tube=0.1827/0.1*L; %tube developing length (m)
N_group=9;

Dh_shell=0.006802423;  %shell side hydraulic diameter (m)
p=0.05; %pitch length (m)0.006802423
D_tube=0.0012; %outer diameter (m)
D_tube_inner=0.001;
N_tube=48;   %tube number in one group
A_tube_cross=3.1415926*(D_tube_inner/2)^2*N_tube*N_group;
D_mandrel=0.0095;
A_shell_cross=(3.1415926*(0.0305/2)^2-3.1415926*(D_tube/2)^2*N_tube-
3.1415926*(D_mandrel/2)^2)*N_group;   %shell side cross section area (m^2)
```

```
A_heat_transfer_shell=(0.0331/0.1*L)*N_group; %heat transfer area for 8 groups
A_prime_shell=A_heat_transfer_shell./L;
A_heat_transfer_tube=(0.00057449/0.1*L)*N_tube*N_group;
A_prime_tube=A_heat_transfer_tube/L;
SF=12.088; %conduction shape factor
DD=0.003061; %nearest distance (m)
A_metal_cross=3.1415926*((D_tube/2)^2-(D_tube_inner/2)^2)*N_tube*N_group;

%%%Geometry 48 p50 1 0.8 9 groups
% L=5.4; %Heat exchanger length (m)
% L_tube=0.1827/0.1*L; %tube developing length (m)
% N_group=9;
%
% Dh_shell=0.0086;  %shell side hydraulic diameter (m)
% p=0.05; %pitch length (m)
% D_tube=0.001; %outer diameter (m)
% D_tube_inner=0.0008;
% N_tube=48;   %tube number in one group
% A_tube_cross=3.1415926*(D_tube_inner/2)^2*N_tube*N_group;
% D_mandrel=0.0095;
% A_shell_cross=(3.1415926*(0.0305/2)^2-3.1415926*(D_tube/2)^2*N_tube-
3.1415926*(D_mandrel/2)^2)*N_group;   %shell side cross section area (m^2)
%
% A_heat_transfer_shell=(0.0275/0.1*L)*N_group; %heat transfer area for 8 groups
% A_prime_shell=A_heat_transfer_shell./L;
% A_heat_transfer_tube=(3.1415926*D_tube_inner*L_tube)*N_tube*N_group;
% A_prime_tube=A_heat_transfer_tube/L;
% SF=8.73; %dimensionless conduction shape factor
% DD=0.003061; %nearest distance (m)
% A_metal_cross=3.1415926*((D_tube/2)^2-(D_tube_inner/2)^2)*N_tube*N_group;

%%%Geometry 48 p60 1 0.8 9 groups
% L=5.4; %Heat exchanger length (m)
% L_tube=0.1543/0.1*L; %tube developing length (m)
% N_group=9;
%
% Dh_shell=0.0096;  %shell side hydraulic diameter (m)
% p=0.06; %pitch length (m)
% D_tube=0.001; %outer diameter (m)
% D_tube_inner=0.0008;
% N_tube=48;   %tube number in one group
% A_tube_cross=3.1415926*(D_tube_inner/2)^2*N_tube*N_group;
% D_mandrel=0.0095;
% A_shell_cross=(3.1415926*(0.0305/2)^2-3.1415926*(D_tube/2)^2*N_tube-
3.1415926*(D_mandrel/2)^2)*N_group;   %shell side cross section area (m^2)
%
% A_heat_transfer_shell=(0.0249/0.1*L)*N_group; %heat transfer area for 8 groups
% A_prime_shell=A_heat_transfer_shell./L;
% A_heat_transfer_tube=(3.1415926*D_tube_inner*L_tube)*N_tube*N_group;
% A_prime_tube=A_heat_transfer_tube/L;
% SF=6.0817; %dimensionless conduction shape factor
% DD=0.003061; %nearest distance (m)
% A_metal_cross=3.1415926*((D_tube/2)^2-(D_tube_inner/2)^2)*N_tube*N_group;
```

```
%%%Geometry 48 p40 1 0.8 9 groups
% L=5.4; %Heat exchanger length (m)
% L_tube=0.2057/0.1*L; %tube developing length (m)
% N_group=9;
%
% Dh_shell=0.0068;  %shell side hydraulic diameter (m)
% p=0.04; %pitch length (m)
% D_tube=0.001; %outer diameter (m)
% D_tube_inner=0.0008;
% N_tube=48;   %tube number in one group
% A_tube_cross=3.1415926*(D_tube_inner/2)^2*N_tube*N_group;
% D_mandrel=0.0095;
% A_shell_cross=(3.1415926*(0.0305/2)^2-3.1415926*(D_tube/2)^2*N_tube-
3.1415926*(D_mandrel/2)^2)*N_group;   %shell side cross section area (m^2)
%
% A_heat_transfer_shell=(0.0342/0.1*L)*N_group; %heat transfer area for 8 groups
% A_prime_shell=A_heat_transfer_shell./L;
% A_heat_transfer_tube=(3.1415926*D_tube_inner*L_tube)*N_tube*N_group;
% A_prime_tube=A_heat_transfer_tube/L;
% SF=19.0525; %dimensionless conduction shape factor
% DD=0.003061; %nearest distance (m)
% A_metal_cross=3.1415926*((D_tube/2)^2-(D_tube_inner/2)^2)*N_tube*N_group;

%Radiation parasitics
sigma=5.67*10^(-8); %Stefan-Boltzmann constant [W/m^2-K^4]
E_316ss=0.28; %Room temp 316 stainless steel emissivity
T_inf=300;   %average metal emissivity
As_o_prime=3.1415926*0.031*1*N_group;   %surface area/length
phi_c_in=Tcin/T_inf;
phi_h_in=Thin/T_inf;
alpha_r=L*sigma*E_316ss*As_o_prime*T_inf^3/Cmin;

[Thetam,Thetah,Thetac,X,eff_avg,DeltaPh_total,DeltaPc_total,betac,betah,Re_c,Re_h,h_c
,h_h,u_c,u_h,rho_c,rho_h,Cc,Ch,kss]=HXsolve(n,wt,tol1,tol1);
eff_avg
DeltaPh_total
DeltaPc_total

%Temperature Profile
Tm_finished=Thetam.*(Thin-Tcin)+Tcin; %metal
Th_finished=Thetah.*(Thin-Tcin)+Tcin; %hot side
Tc_finished=Thetac.*(Thin-Tcin)+Tcin; %cold side


A_tube=A_heat_transfer_tube/n;
A_shell=A_heat_transfer_shell/n;
R_tube=1./(h_h.*A_tube);
R_shell=1./(h_c.*A_shell);
R_metal=log(D_tube/D_tube_inner)./(2.*3.1415926.*L_tube./n.*kss);
R_total=R_tube+R_shell+R_metal(2:n+2);
UA=1./R_total;
NTU=UA./Cc;
C_R=Cc./Ch;
% epsilon_co=(1-exp.(-NTU.*(1-C_R))./(1-C_R.*exp.(-NTU.*(1-C_R)));
% epsilon_cr=1-exp.(NTU.^0.22./C_R.*(exp.(-C_R.*NTU.^0.78)-1));
```

"Matrix assembly and decompose"

```
function
[Thetam,Thetah,Thetac,X,eff_avg,DeltaPh_total,DeltaPc_total,betac,betah,Re_c,Re_h,h_c
,h_h,u_c,u_h,rho_c,rho_h,Cc,Ch,kss]=HXsolve(n,wt,tol1,tol2)
    global L
    %Setup empty vectors and matrices
    Xm=zeros(n+2,1);
    Xf=zeros(n+1,1);
    DeltaX=zeros(n+1,1);
    N=3*n+4;
    A=spalloc(N,N,13*n+6);
    b=spalloc(N,1,N);
    S=spalloc(N,1,N);

    %Setup grid
    DeltaX(1,1)=0;
    DeltaX(n+2,1)=0;

    for i=2:(n+1)
        DeltaX(i,1)=L/n;
    end

    %Normalize DeltaX
    DeltaX=DeltaX/sum(DeltaX);

    Xm(1,1)=0;
    for i=1:n
        Xm(i+1,1)=Xm(i,1)+(DeltaX(i,1)+DeltaX(i+1,1))/2;
    end
    Xm(n+2,1)=1;
    Xf(1,1)=0;
    for i=1:n
        Xf(i+1,1)=Xf(i,1)+DeltaX(i+1,1);
    end

    %Position
    x=Xm.*L;
    deltax=DeltaX.*L;

    %initial guesses
    Thetam=1-Xm;
    Thetah=1-Xf;
```

```
    Thetac=1-Xf;

    done=0;

    while (done==0)
        %thermal properties at current guesses

[betac,DeltaPc,h_c,Re_c,u_c,rho_c]=arrayfun(@betacf,Thetac(1:n+1),Thetam(1:n+1),delta
x(1:n+1));

[betah,DeltaPh,h_h,Re_h,u_h,rho_h]=arrayfun(@betahf,Thetah(1:n+1),Thetam(1:n+1),delta
x(1:n+1));
        [lambda,kss]=arrayfun(@lambdaf,Thetam(1:n+2));
        %[lambda]=arrayfun(@lambdaf,Thetam(1:n+2));
        [mu,Ch]=arrayfun(@muf,Thetah(1:n+1));
        [nu,Cc]=arrayfun(@nuf,Thetac(1:n+1));
        chih=arrayfun(@chicf,Thetah(1:n+1));
        chic=arrayfun(@chihf,Thetac(1:n+1));
        chim=arrayfun(@chimf,Thetam(1:n+1));

        %setup matrix, 3n+4 equations and unknowns,
        %solution matrix assembled in a order of
(Thetam1,Thetam2,...,Thetam_n+2,Thetah_1,Thetah_2,...,Thetah_n+1,Thetac_1,Thetac_2,..
.,Thetac_n,Thetac_n+1)

        %Hot side inlet boundary condition
        b(n+3,1)=1;
        A(n+3,n+3)=1;
        %cold side inlet boundary condition (counterflow)
        b(2*n+4,1)=0;
        A(2*n+4,3*n+4)=1;
        %meta adiabatic BCs
        A(1,1)=1;
        A(1,2)=-1;
        %b(1,1)=0;
        A(n+2,n+1)=-1;
        A(n+2,n+2)=1;
        %b(n+2,1)=0;
        for i=1:n
            %setup matrix for hot side energy balance
            b(n+3+i,1)= (chih(i+1,1)+chih(i,1)).*DeltaX(i+1,1)/2;
            A(n+3+i,n+3+i-1)=(betah(i+1,1)+betah(i,1)).*DeltaX(i+1,1)/4-
(mu(i+1,1)+mu(i,1))/2;

A(n+3+i,n+3+i)=(betah(i+1,1)+betah(i,1)).*DeltaX(i+1,1)/4+(mu(i+1,1)+mu(i,1))/2;
            A(n+3+i,i+1)=-(betah(i+1,1)+betah(i,1)).*DeltaX(i+1,1)/2;
            %setup matrix for cold side energy balance (counterflow)

A(2*n+4+i,2*n+3+i)=(betac(i+1,1)+betac(i,1)).*DeltaX(i+1,1)/4+(nu(i+1,1)+nu(i,1))/2;
            A(2*n+4+i,2*n+3+i+1)=(betac(i+1,1)+betac(i,1)).*DeltaX(i+1,1)/4-
(nu(i+1,1)+nu(i,1))/2;
            A(2*n+4+i,i+1)=-(betac(i+1,1)+betac(i,1)).*DeltaX(i+1,1)/2;
            b(2*n+4+i,1)=(chic(i+1,1)+chic(i,1)).*DeltaX(i+1,1)/2;
            %setup matrix for metal energy balance
            b(i+1,1)=chim(i+1,1).*DeltaX(i+1,1);
```

```
            A(i+1,n+3+i-1)=-(betah(i+1,1)+betah(i,1)).*DeltaX(i+1,1)/4;
            A(i+1,n+3+i)=-(betah(i+1,1)+betah(i,1)).*DeltaX(i+1,1)/4;
            A(i+1,2*n+4+i-1)=-(betac(i+1,1)+betac(i,1)).*DeltaX(i+1,1)/4;
            A(i+1,2*n+4+i)=-(betac(i+1,1)+betac(i,1)).*DeltaX(i+1,1)/4;
            A(i+1,i)=-(lambda(i+1,1)+lambda(i,1))./(DeltaX(i+1,1)+DeltaX(i,1));
            A(i+1,i+2)=-(lambda(i+1,1)+lambda(i+2,1))./(DeltaX(i+1,1)+DeltaX(i+2,1));

A(i+1,i+1)=(lambda(i+1,1)+lambda(i+2,1))./(DeltaX(i+1,1)+DeltaX(i+2,1))+(lambda(i+1,1
)+lambda(i,1))./(DeltaX(i+1,1)+DeltaX(i,1)) ...

+(betac(i+1,1)+betac(i,1)).*DeltaX(i+1,1)/2+(betah(i+1,1)+betah(i,1)).*DeltaX(i+1,1)/
2;
        end

        %decompose matrix
        S=A\b;
        for i=1:n+1
            Thetam_n(i,1)=S(i);
            Thetah_n(i,1)=S(n+3+i-1);
            Thetac_n(i,1)=S(2*n+4+i-1);
        end
        Thetam_n(n+2,1)=S(n+2);

        %calculate error
        err=max([max(abs(Thetam-Thetam_n)),max(abs(Thetah-Thetah_n)),max(abs(Thetac-
Thetac_n))])

        %check for convergence
        if err<tol1
            done=1;
            Thetam=Thetam_n;
            Thetah(1,1)=Thetah_n(1,1);
            Thetah(n+2,1)=Thetah_n(n+1,1);
            Thetac(1,1)=Thetac_n(1,1);
            Thetac(n+2,1)=Thetac_n(n+1,1);
            for i=2:n+1
                Thetah(i,1)=(Thetah_n(i,1)+Thetah_n(i-1,1))/2;
                Thetac(i,1)=(Thetac_n(i,1)+Thetac_n(i-1,1))/2;
            end
            X=Xm;
        else
            for i=1:n+1
            Thetac(i,1)=wt*Thetac_n(i,1)+(1-wt)*Thetac(i,1);
            Thetah(i,1)=wt*Thetah_n(i,1)+(1-wt)*Thetah(i,1);
            Thetam(i,1)=wt*Thetam_n(i,1)+(1-wt)*Thetam(i,1);
            end
            Thetam(n+2,1)=wt*Thetam_n(n+2,1)+(1-wt)*Thetam(n+2,1);
        end
    end

    Thetah=full(Thetah);
    Thetac=full(Thetac);
    Thetam=full(Thetam);

    Qdh=integral(@muf,Thetah(n+2),1,'AbsTol',tol2,'ArrayValued',true);
```

```
    Qdc=integral(@nuf,0,Thetac(0+1),'AbsTol',tol2,'ArrayValued',true);

    DeltaPh_total=sum(DeltaPh);
    DeltaPc_total=sum(DeltaPc);

    %non-dim heat transfer rates from each fluid to metal
    Qdhm=trapz(X,betahf(Thetah,Thetam,deltax).*(Thetah-Thetam));
    Qdmc=trapz(X,betacf(Thetac,Thetam,deltax).*(Thetam-Thetac));
    %max possible non-dim heat transfer rate
    Qdmaxh=integral(@muf,0,1,'AbsTol',tol2,'ArrayValued',true);
    Qdmaxc=integral(@nuf,0,1,'AbsTol',tol2,'ArrayValued',true);
    Qdmax=min(Qdmaxh,Qdmaxc);
    %effectivenesses
    effh=Qdh/Qdmax;
    effc=Qdc/Qdmax;
    eff_avg=(effh+effc)./2;

    %non-dim parasitic heat transfer rates
     Qpdh=trapz(X,chihf(Thetah));
     Qpdc=trapz(X,chicf(Thetac));
     Qpdm=trapz(X,chimf(Thetam));
    %non-dim conduction into hot END
    Qdmhot=lambdaf(Thetam(1))*2*(Thetam(1)-Thetam(2))/DeltaX(2);
    %non-dim conduction out of cold END
    Qdmcold=lambdaf(Thetam(n+2))*2*(Thetam(n+1)-Thetam(n+2))/DeltaX(n+1);
    %overall energy balance. should ~ 0
    UBtotal=-Qdh+Qdc-Qpdh-Qpdc-Qpdm-Qdmhot+Qdmcold;

End
```

"betacf.m"

```
function[betac,DeltaPc,h_c,Re_c,u,rho]=betacf(Thetac,Thetam,deltax)
    global Thin Tcin Cmin mdot L A_shell_cross Dh_shell p D_tube N_tube
A_heat_transfer_shell SF DD
    Tc=Thetac.*(Thin-Tcin)+Tcin;
    Tm=Thetam.*(Thin-Tcin)+Tcin;
    T_film=(Tc+Tm)./2;


    %helium properties @ P = 689.5 kPa, 30 K <= T <= 300 K
    mu=1.1070E-20.*T_film.^6 + 2.2154E-18.*T_film.^5 - 8.4392E-15.*T_film.^4 +
3.9089E-12.*T_film.^3 - 7.9840E-10.*T_film.^2 + 1.3258E-07.*T_film + 1.4175E-06;
    k=-1.1043E-16.*T_film.^6 + 1.3209E-13.*T_film.^5 - 6.6180E-11.*T_film.^4 +
1.8464E-08.*T_film.^3 - 3.4098E-06.*T_film.^2 + 8.2510E-04.*T_film + 1.2804E-02;
    rho=6.2042E-13.*T_film.^6 - 6.9372E-10.*T_film.^5 + 3.1374E-07.*T_film.^4 -
7.3649E-05.*T_film.^3 + 9.5755E-03.*T_film.^2 - 6.8024E-01.*T_film + 2.4144E+01;


    u=mdot./(A_shell_cross.*rho);
    Re_c=rho.*u.*Dh_shell./mu;
    Nu=0.5833.*(p./D_tube).^0.66005.*N_tube^(-0.618).*Re_c.^0.60825;
    h_c=Nu.*k./Dh_shell;
    A_prime_shell=A_heat_transfer_shell./L;
    betac=h_c.*A_prime_shell.*L./Cmin;
```

```
    f=6.70262.*(p./D_tube).^0.38582.*(DD./D_tube).^0.27427.*(SF)^0.2613.*N_tube.^(-
0.39882).*Re_c.^(-0.39059);
    DeltaPc=f.*(deltax./Dh_shell).*(1/2).*rho.*u.^2;

end
```

“betahf.m”

```
function [betah,DeltaPh,h_h,Re_h,u,rho]=betahf(Thetah,Thetam,deltax)
    global Thin Tcin mdot Cmin p D_tube D_tube_inner L L_tube A_tube_cross
A_heat_transfer_tube A_prime_tube N_tube N_group
    Th=Thetah.*(Thin-Tcin)+Tcin;    %Hot fluid temperature
    Tm=Thetam.*(Thin-Tcin)+Tcin;    %Metal temperature
    T_film=(Th+Tm)./2;              %hot side film temperature

    %helium properties @ P = 2206 kPa, 30 K <= T <= 300 K
    mu=2.9483E-20.*T_film.^6 - 1.8325E-17.*T_film.^5 + 8.0501E-16.*T_film.^4 +
1.7607E-12.*T_film.^3 - 5.2491E-10.*T_film.^2 + 1.1352E-07.*T_film + 2.1878E-06;
    k=4.6420E-17.*T_film.^6 - 4.4895E-14.*T_film.^5 + 1.5101E-11.*T_film.^4 -
1.0948E-09.*T_film.^3 - 7.6655E-07.*T_film.^2 + 6.2670E-04.*T_film + 2.0982E-02;
    rho=1.9142E-12.*T_film.^6 - 2.1384E-09.*T_film.^5 + 9.6595E-07.*T_film.^4 -
2.2640E-04.*T_film.^3 + 2.9379E-02.*T_film.^2 - 2.0833E+00.*T_film + 7.4099E+01;


    A_tube_cross=3.1415926*(D_tube_inner/2)^2*N_tube*N_group;
    u=mdot./(A_tube_cross.*rho);
    Re_h=rho.*u.*D_tube_inner./mu;
    Nu=0.06105.*(p./D_tube_inner).^(-0.02156).*Re_h.^0.71054;
    h_h=Nu.*k./D_tube_inner;
    betah=h_h.*A_prime_tube.*L./Cmin;

    f=2.68097.*(p./D_tube).^(-0.07549).*Re_h.^(-0.43137);
    DeltaPh=f.*(deltax.*L_tube./L./D_tube_inner).*(1/2).*rho.*u.^2;
End
```

“chicf”

```
function[chic]=chicf(Thetac)
    global  phi_c_in phi_h_in
    [m,n]=size(Thetac);
    qmp=0*ones(m,1); % metal parasitic heat transfer rate per unit length
    % dimensionless parasitic heat load input to metal
    chic=qmp;
end
```

“chihf”

```
function[chih]=chihf(Thetah)
    global  phi_c_in phi_h_in alpha_r
    %[m,n]=size(Thetah);
    %qmp=0*ones(m,1); % metal parasitic heat transfer rate per unit length
```

```
    % dimensionless parasitic heat load input to metal
    chih=alpha_r.*(1-(phi_c_in+Thetah.*(phi_h_in-phi_c_in)).^4)./(phi_h_in-
phi_c_in).*0;
end

“chimf”
function[chim]=chimf(Thetam)
    global  phi_c_in phi_h_in
    [m,n]=size(Thetam);
    qmp=0*ones(m,1); % metal parasitic heat transfer rate per unit length
    % dimensionless parasitic heat load input to metal
    chim=qmp;
end

“lambdaf”
function[lambda,kss]=lambdaf(Thetam)
    global Cmin Thin Tcin L A_metal_cross
    Tm=Thetam.*(Thin-Tcin)+Tcin;    %metal temperature

    %thermal conductivities, 30 K <= T <= 300 K
    kss=1.7455E-13.*Tm.^6 - 1.4021E-10.*Tm.^5 + 3.5267E-08.*Tm.^4 - 7.8535E-07.*Tm.^3
- 1.0273E-03.*Tm.^2 + 1.9304E-01.*Tm - 1.4506E+00;

    lambda=kss.*A_metal_cross./L./Cmin;


end


“muf”
function[mu,Ch]=muf(Thetah)
    global Cmin Thin Tcin mdot
    Th=Thetah.*(Thin-Tcin)+Tcin;
    %specific heat capacity of helium @ P=2206 kPa, 30 K <= T <= 300 K
    c_h=4.7518E-11.*Th.^6 - 5.2560E-08.*Th.^5 + 2.3400E-05.*Th.^4 - 5.3599E-03.*Th.^3
+ 6.6799E-01.*Th.^2 - 4.3524E+01.*Th + 6.4003E+03;
    Ch=mdot.*c_h;

    %dimensionless capacitance rate on hot side
    mu=Ch./Cmin;
end

“nuf”
function[mu,Ch]=muf(Thetah)
    global Cmin Thin Tcin mdot
    Th=Thetah.*(Thin-Tcin)+Tcin;
    %specific heat capacity of helium @ P=2206 kPa, 30 K <= T <= 300 K
    c_h=4.7518E-11.*Th.^6 - 5.2560E-08.*Th.^5 + 2.3400E-05.*Th.^4 - 5.3599E-03.*Th.^3
+ 6.6799E-01.*Th.^2 - 4.3524E+01.*Th + 6.4003E+03;
    Ch=mdot.*c_h;

    %dimensionless capacitance rate on hot side
    mu=Ch./Cmin;
end
```

Appendix B. EES code for calculating the developing length of the tubes and the angle between each tube and the flow direction

```
"8 tubes"
p=50
x=0
y=0
z=1
x1=10*cos(2*pi*t/p)+4*cos(2*pi*t/25+2*pi/8)
y1=10*sin(2*pi*t/p)+4*sin(2*pi*t/(p/2)+2*pi/8)
z1=t
x1_prime=-2/5*pi*sin(2*pi*t/p)-8*pi/25*sin(2*pi*t/(p/2)+2*pi/8)
y1_prime=2/5*pi*cos(2*pi*t/p)+8*pi/25*cos(2*pi*t/(p/2)+2*pi/8)
z1_prime=1
cos_theta1=(x1_prime*x+y1_prime*y+z1_prime*z)/sqrt(x1_prime^2+y1_prime^2+z1_prime^2)/sqrt(x^2+y^2+z^2)
theta_1=arccos(cos_theta1)*360/(2*pi)
Dc_1=sqrt(x1^2+y1^2)
"ds=sqrt(x1_prime^2+y1_prime^2+z1_prime^2)
s=integral(ds,t,0,100)"

x2=10*cos(2*pi*t/p)+4*cos(2*pi*t/(p/2)+4*pi/8)
y2=10*sin(2*pi*t/p)+4*sin(2*pi*t/(p/2)+4*pi/8)
z2=t
x2_prime=-2/5*pi*sin(2*pi*t/p)-8*pi/25*sin(2*pi*t/(p/2)+4*pi/8)
y2_prime=2/5*pi*cos(2*pi*t/p)+8*pi/25*cos(2*pi*t/(p/2)+4*pi/8)
z2_prime=1
cos_theta2=(x2_prime*x+y2_prime*y+z2_prime*z)/sqrt(x2_prime^2+y2_prime^2+z2_prime^2)/sqrt(x^2+y^2+z^2)
theta_2=arccos(cos_theta2)*360/(2*pi)
Dc_2=sqrt(x2^2+y2^2)

x3=10*cos(2*pi*t/p)+4*cos(2*pi*t/(p/2)+6*pi/8)
y3=10*sin(2*pi*t/p)+4*sin(2*pi*t/(p/2)+6*pi/8)
z3=t
x3_prime=-2/5*pi*sin(2*pi*t/p)-8*pi/25*sin(2*pi*t/(p/2)+6*pi/8)
y3_prime=2/5*pi*cos(2*pi*t/p)+8*pi/25*cos(2*pi*t/(p/2)+6*pi/8)
z3_prime=1
cos_theta3=(x3_prime*x+y3_prime*y+z3_prime*z)/sqrt(x3_prime^2+y3_prime^2+z3_prime^2)/sqrt(x^2+y^2+z^2)
theta_3=arccos(cos_theta3)*360/(2*pi)
Dc_3=sqrt(x3^2+y3^2)

x4=10*cos(2*pi*t/p)+4*cos(2*pi*t/(p/2)+8*pi/8)
y4=10*sin(2*pi*t/p)+4*sin(2*pi*t/(p/2)+8*pi/8)
z4=t
x4_prime=-2/5*pi*sin(2*pi*t/p)-8*pi/25*sin(2*pi*t/(p/2)+8*pi/8)
y4_prime=2/5*pi*cos(2*pi*t/p)+8*pi/25*cos(2*pi*t/(p/2)+8*pi/8)
z4_prime=1
cos_theta4=(x4_prime*x+y4_prime*y+z4_prime*z)/sqrt(x4_prime^2+y4_prime^2+z4_prime^2)/sqrt(x^2+y^2+z^2)
theta_4=arccos(cos_theta4)*360/(2*pi)
```

```
Dc_4=sqrt(x4^2+y4^2)

x5=10*cos(2*pi*t/p)+4*cos(2*pi*t/(p/2)+10*pi/8)
y5=10*sin(2*pi*t/p)+4*sin(2*pi*t/(p/2)+10*pi/8)
z5=t
x5_prime=-2/5*pi*sin(2*pi*t/p)-8*pi/25*sin(2*pi*t/(p/2)+10*pi/8)
y5_prime=2/5*pi*cos(2*pi*t/p)+8*pi/25*cos(2*pi*t/(p/2)+10*pi/8)
z5_prime=1
cos_theta5=(x5_prime*x+y5_prime*y+z5_prime*z)/sqrt(x5_prime^2+y5_prime^2+z5_prime^2)/sqrt(x^2+y
^2+z^2)
theta_5=arccos(cos_theta5)*360/(2*pi)
Dc_5=sqrt(x5^2+y5^2)

x6=10*cos(2*pi*t/p)+4*cos(2*pi*t/(p/2)+12*pi/8)
y6=10*sin(2*pi*t/p)+4*sin(2*pi*t/(p/2)+12*pi/8)
z6=t
x6_prime=-2/5*pi*sin(2*pi*t/p)-8*pi/25*sin(2*pi*t/(p/2)+12*pi/8)
y6_prime=2/5*pi*cos(2*pi*t/p)+8*pi/25*cos(2*pi*t/(p/2)+12*pi/8)
z6_prime=1
cos_theta6=(x6_prime*x+y6_prime*y+z6_prime*z)/sqrt(x6_prime^2+y6_prime^2+z6_prime^2)/sqrt(x^2+y
^2+z^2)
theta_6=arccos(cos_theta6)*360/(2*pi)
Dc_6=sqrt(x6^2+y6^2)

x7=10*cos(2*pi*t/p)+4*cos(2*pi*t/(p/2)+14*pi/8)
y7=10*sin(2*pi*t/p)+4*sin(2*pi*t/(p/2)+14*pi/8)
z7=t
x7_prime=-2/5*pi*sin(2*pi*t/p)-8*pi/25*sin(2*pi*t/(p/2)+14*pi/8)
y7_prime=2/5*pi*cos(2*pi*t/p)+8*pi/25*cos(2*pi*t/(p/2)+14*pi/8)
z7_prime=1
cos_theta7=(x7_prime*x+y7_prime*y+z7_prime*z)/sqrt(x7_prime^2+y7_prime^2+z7_prime^2)/sqrt(x^2+y
^2+z^2)
theta_7=arccos(cos_theta7)*360/(2*pi)
Dc_7=sqrt(x7^2+y7^2)


x8=10*cos(2*pi*t/p)+4*cos(2*pi*t/(p/2)+16*pi/8)
y8=10*sin(2*pi*t/p)+4*sin(2*pi*t/(p/2)+16*pi/8)
z8=t
x8_prime=-2/5*pi*sin(2*pi*t/p)-8*pi/25*sin(2*pi*t/(p/2)+16*pi/8)
y8_prime=2/5*pi*cos(2*pi*t/p)+8*pi/25*cos(2*pi*t/(p/2)+16*pi/8)
z8_prime=1
cos_theta8=(x8_prime*x+y8_prime*y+z8_prime*z)/sqrt(x8_prime^2+y8_prime^2+z8_prime^2)/sqrt(x^2+y
^2+z^2)
theta_8=arccos(cos_theta8)*360/(2*pi)
Dc_8=sqrt(x8^2+y8^2)


avg_cos_theta=(cos_theta1+cos_theta2+cos_theta3+cos_theta4+cos_theta5+cos_theta6+cos_theta7+c
os_theta8)/8
avg_theta=(theta_1+theta_2+theta_3+theta_4+theta_5+theta_6+theta_7+theta_8)/8
avg_Dc=(Dc_1+Dc_2+Dc_3+Dc_4+Dc_5+Dc_6+Dc_7+Dc_8)/8
```

Appendix C. EES code for calculating the surface equation perpendicular to the flow direction

```
"p25"
x=10*cos(2*pi*t/25)+4*cos(2*pi*t/12.5+2.4*pi/6)
y=10*sin(2*pi*t/25)+4*sin(2*pi*t/12.5+2.4*pi/6)
z=t
x_prime=-4/5*pi*sin(2*pi*t/25)-16/25*pi*sin(2*pi*t/12.5+2.4*pi/6)
y_prime=4/5*pi*cos(2*pi*t/25)+16/25*pi*cos(2*pi*t/12.5+2.4*pi/6)
z_prime=1
t=50

"-1.912*x+0.01124*1.912+3.135*y-0.003804*3.135+z-0.05=0
z=0.07
y=0.00"

"p50"
"x=10*cos(2*pi*t/50)+4*cos(2*pi*t/25+2.4*pi/6)
y=10*sin(2*pi*t/50)+4*sin(2*pi*t/25+2.4*pi/6)
z=t
x_prime=-2/5*pi*sin(pi*t/25)-8*pi/25*sin(2*pi*t/25+2.4*pi/6)
y_prime=2/5*pi*cos(pi*t/25)+8*pi/25*cos(2*pi*t/25+2.4*pi/6)
z_prime=1
t=50"

"-0.9561*x+1.567*y+z-0.0452=0
z=0.04
y=0.003804"

"p25 a20 b8"
"x=20*cos(2*pi*t/25)+8*cos(2*pi*t/12.5+2.4*pi/6)
y=20*sin(2*pi*t/25)+8*sin(2*pi*t/12.5+2.4*pi/6)
z=t
x_prime=-8/5*pi*sin(2*pi*t/25)-32/25*pi*sin(2*pi*t/12.5+2.4*pi/6)
y_prime=8/5*pi*cos(2*pi*t/25)+32/25*pi*cos(2*pi*t/12.5+2.4*pi/6)
z_prime=1
t=50"

"(x-0.02247)*(-3.824)+(y-0.007608)*6.269+(z-0.05)*1=0
y=0.007608
z=0.05"
```

Appendix D EES code for calculating the minor losses

```
"Shell end header"
"Re=7200
LoverD=0.1827*5/0.001
sigma=(48*pi*0.0005^2)/(pi*(0.0305/2)^2)
K_e=k_e_circulartubeheader(Re,LoverD,sigma)
K_c=k_c_circulartubeheader(Re,LoverD,sigma)
K_e=2*delta_Pe/rho/u^2
K_c=2*delta_Pc/rho/u^2
rho=31.3396[kg/m^3]
u=1.2226[m/s]"

"upper header expansion loss"
Re=7200
A_tube_48=48[m^2]*pi*0.0005^2

L_to_upper=0.025[m]
D_9=0.0036[m]
LoverD_9=L_to_upper/D_9
A_header_l=0.0658*0.0882 [m^2]
A_tube_9=9*pi*D_9^2/4
sigma_9=A_tube_9/A_header_l
K_e_9=k_e_circulartubeheader(Re,LoverD_9,sigma_9)
K_e_9=2*delta_Pe/rho/u^2
rho=31.3396[kg/m^3]
u=1.2226 [m/s] *A_tube_48/A_tube_9

"upper header contraction loss"
Re=7200
LoverD=25/3.6
sigma=(48*pi*0.0005^2)/(0.0658*0.0882)
K_c=k_c_circulartubeheader(Re,LoverD,sigma)
K_e=2*delta_Pe/rho/u^2
rho=31.3396[kg/m^3]
u=1.2226 [m/s] *48*pi*0.0005^2/(48*pi*0.0005^2)
D_1=0.0096[m]

$UnitSystem SI K Pa J
r=0.006[m]
D=0.0096[m]
RelRough=0
"rho=3.7286[kg/m^3]"
rho=30.3263[kg/m^3]
m_dot=rho*v*A
m_dot=0.013[kg/s]
A=pi*D^2/4
g=g#


K=k_90deg_bend(r,D,RelRough)
h_L=K*v^2/(2*g)
DELTAP=h_L*rho*g
```